UNIVERSIDADE FEDERAL DE PERNAMBUCO

CENTRO DE TECNOLOGIA E GEOCIÊNCIAS

DEPARTAMENTO DE GEOLOGIA

PROGRAMA DE PÓS-GRADUAÇÃO EM GEOCIÊNCIAS

SALVIANO PEREIRA DA SILVA

HISTÓRIA METAMÓRFICA DE UM PLATÔ OCEÂNICO: O exemplo do Complexo Raspas, Equador

Recife

2022

SALVIANO PEREIRA DA SILVA

HISTÓRIA METAMÓRFICA DE UM PLATÔ OCEÂNICO: O exemplo do Complexo Raspas, Equador

Dissertação apresentada ao Programa de Pós-Graduação em Geociências da Universidade Federal de Pernambuco, como requisito parcial para a obtenção do título de Mestre em Geociências.

Área de concentração: Geoquímica, geofísica e evolução crustal

Orientadora: Prof. Dra. Carla Joana Santos Barreto

Recife

2022

Catalogação na fonte
Bibliotecário Gabriel Luz CRB-4 / 2222

S586h Silva, Salviano Pereira da.
História metamórfica de um platô oceânico: o exemplo do Complexo Raspas, Equador / Salviano Pereira da Silva. 2022.
160 f: figs., tabs.

Orientadora: Profa. Dra. Carla Joana Santos Barreto.
Dissertação (Mestrado) – Universidade Federal de Pernambuco. CTG.
Programa de Pós-Graduação em Geociências, Recife, 2022.
Inclui referências.

1. Geociências. 2. Eclogito. 3. Xisto azul. 4. Platô oceânico. 5. Rollback. 6. Slab breakoff. I. Barreto, Carla Joana Santos (Orientadora). II. Título.

UFPE

551 CDD (22. ed.) BCTG / 2022 - 438

SALVIANO PEREIRA DA SILVA

HISTÓRIA METAMÓRFICA DE UM PLATÔ OCEÂNICO: O exemplo do Complexo Raspas, Equador

Dissertação apresentada ao Programa de Pós-Graduação em Geociências da Universidade Federal de Pernambuco, como requisito para a obtenção do título de Mestre em Geociências.
Área de concentração: Geoquímica, geofísica e evolução crustal

Aprovada em 05/12/2022.

BANCA EXAMINADORA

_____
Prof(a). Dr(a). Carla Joana Santos Barreto (Orientadora)
Universidade Federal de Pernambuco

_____
Prof. Dr. Lauro Cézar Montefalco de Lira Santos (Examinador Interno)
Universidade Federal de Pernambuco

_____
Prof. Dr. Rafael Gonçalves da Motta (Examinador Externo)
Universidade Federal do Rio Grande do Norte

AGRADECIMENTOS

Alô mainha, a existência desse trabalho e de onde cheguei é por sua causa, muito obrigado por todo o suporte e incentivo durante essa jornada! Sabrina, minha irmã saiba que estarei para lhe dar apoio na sua jornada do caminho científico se essa for sua decisão.

Lu, minha namorada e companheira, muito obrigado pelo apoio nos momentos de angústia, tristeza, alegria, burnout e frustração em que fui submetido durante esse mestrado. Agradeço também a Mônica por ter aberto as portas de sua casa e fornecer apoio logístico para que eu não ficasse parado durante a pandemia.

Agradeço ao Professor Andres Bustamante que foi como um mentor desde o início de minha jornada científica. Prestou todo o apoio mesmo nas minhas ideias malucas ou perguntas sobre as mais diversas áreas. Por ter depositado sua confiança nos dados e amostras utilizados nesse trabalho mais uma vez lhe agradeço.

Agradecimentos também são devidos a um Petit Comitê de amigos geólogos espalhados pelo Brasil: André, Daniel, Cayo, Gabriel, Luiz, Tiago, Will, Rafael, Diniz, Allan, Ian, Winston. Espero nos reunirmos em uma reunião especial do AA futuramente.

Agradeço à Coordenação de Aperfeiçoamento de Pessoal de Nível Superior – Brasil (CAPES) pela bolsa; a Fundação de Amparo à Pesquisa do Estado de São Paulo (FAPESP) pelo financiamento parcial de análises (2004/10203-7); e ao Conselho Nacional de Desenvolvimento Científico e Tecnológico (CNPq) pelo financiamento parcial (458735/2014-0).

RESUMO

Platôs oceânicos são porções da crosta anomalamente espessas cuja origem é associada a grandes volumes de magma oriundos de plumas mantélicas. A maior parte do seu registro é apenas acessível como fragmentos acrescionados em margens ativas. Contudo, apesar de modelos matemáticos preverem a possibilidade de platôs oceânicos serem subduzidos não existem registros de fragmentos que atingiram grandes profundidades e exumados, como eclogitos e xistos azul. Nesse trabalho são apresentadas evidências geoquímicas, geocronológicas e de modelagem termodinâmica que provam a subducção e exumação de platôs oceânicos. A partir desses dados discutirá o caminho tectônico percorrido a partir da assinatura metamórfica imprimido em eclogitos e xistos azuis. O estudo teve foco no Complexo Metamórfico Raspas, localizado no sudeste do Equador. Esse complexo ofiolítico de alta pressão é majoritariamente composto por eclogitos, metaultramáficas e xistos azuis além de incipientes assembleias retrógradas como xistos verde e granada anfibolitos subduzidos no Cretáceo Inferior. A assinatura geoquímica demonstra similaridades com N-MORB e E-MORB e material originados em uma fonte mantélica heterogênea (Zr/Nb – 7.69-112.66). Durante a ascensão da pluma mantélica houve o aumento do grau de fusão parcial (Sm/Yb 0.94-1.95) e empobrecimento do material (La/Yb 0.76-6.86). Devido sua elevada espessura as porções mais internas possivelmente receberam menos energia térmica vinda do manto, ou pelo menos o aquecimento foi mais lento. O que foi refletido na diferença de ~100 °C registrada pelos eclogitos e xistos azuis, permitindo a preservação da assembleia formada nos estágios iniciais pelos xistos azuis. O início do evento de alta pressão é marcado pela formação da assembleia winchita + paragonita/fengita + epidoto + quartzo ± clorita no xisto azul em 490 °C/1.15 GPa durante a colisão do platô com a margem Andina facilitado pela sua menor densidade comparado a uma crosta oceânica normal. Resultando em uma compressão isotérmica durante a formação de núcleos de granada em 523 °C/1.68 GPa. No eclogito essa fase é registrada pela assembleia onfacita + katoforita + clinozoisita + granada + quartzo ± fengita entre 598-661 °C/1.43-1.63 GPa. Durante a subducção, à medida que o platô oceânico era transformado em eclogito o aumento de densidade resultante favoreceu o aumento do ângulo de subducção. Esse processo possivelmente gerou um adelgaçamento do platô visto que as porções mais rasas com menor densidade resistiam à subducção enquanto as regiões mais densas, já transformada em eclogito, “puxavam” o platô para o manto. Isso é refletido no aquecimento isobárico imprimido nos eclogitos durante a formação de granadas em atol (709 °C/1.61 GPa) e em uma leve

descompressão com aumento de temperatura durante a formação de granada (borda) + fengita + clinozoisita + onfacita + winchita + quartzo entre 570-590 °C e 1.4-1.7 GPa no xisto azul. Idades Ar/Ar em fengita no eclogito indicam que a exumação ocorreu em 129 Ma, logo após o principal evento de alta pressão ocorrido em 133 Ma. O metamorfismo retrógrado impresso durante a exumação caracteriza-se por uma descompressão isotermal. A qual é representada pela assembleia pargasita + Mg-hornblenda + albita + epidoto + clorita (450-550 °C /< 0.6 GPa) que substitui em graus variados os xistos azuis. A trajetória metamórfica durante a exumação somado a rápida duração da mesma (1.25-0.5 cm/ano) indicam que o principal mecanismo de exumação foi um *slab breakoff* regional consistente com o mecanismo previamente proposto à outras ocorrências na Colômbia.

Palavras-chave: eclogito; xisto azul; platô oceânico; rollback; slab breakoff

ABSTRACT

Most of what we know about oceanic plateaus comes from fragments accreted onto active margins. Although, numeric models suggest that under certain circumstances they may subduct, reports of eclogites or blueschists which protolith was originated from oceanic plateaus are lacking. Here are presented geochemical, geochronological, and metamorphic constraints of blueschists and eclogites from a high-pressure (HP) ophiolite that evidences their oceanic plateau origin debating the metamorphic signature imprinted by the subduction of oceanic plateaus. The study focused on the Raspas Metamorphic Complex, SW of Ecuador. It is made up by eclogites, metaultramafic, and blueschists with minor greenschists and garnet amphibolites that record the onset of an important HP event on Early Cretaceous. They exhibit a N- to E-MORB signature with trace element ratios pointing to a heterogeneous mantle source (Zr/Nb – 7.69-112.66). Moreover, they show evidences of a change on the source depth (Sm/Yb 0.94-1.95) coupled by an increase of a depleted component (La/Yb 0.76-6.86), typical of an ascending mantle plume. The HP event had onset registered by the formation of the assemblage winchite + paragonite/phengite + epidote/clinozoisite + quartz ± chlorite at 490 °C/1.15 GPa on the blueschists. Followed by an isothermal compression during the collision of the plateau with the Andean margin at 523 °C/1.68 GPa observed by the growth of garnet cores and by the eclogitic assemblage omphacite + katophorite + clinozoisite + garnet + quartz ± phengite between 598-661 °C/1.43-1.63 GPa. Due their greater thickness the portion at the center took longer to be fully heated creating a thermal zoning inside the plateau, translated in the temperature difference between eclogites and blueschists. Moreover, the eclogitization of the plateau increased the density favoring slab-pull forces. In this scenario a rollback took place which coupled by an astenospheric flow thinned the plateau. Which is evidenced by an isobaric heating during the formation of atoll garnets on eclogites at 709 °C/1.61 GPa and by the small decompression at the metamorphic peak garnet$_{(rim)}$ + phengite + clinozoisite + wihchite + omphacite + quartz at 570-590 °C/1.4-1.7 GPa on the blueschists. Eclogitic phengite Ar/Ar ages of 129 Ma indicate fast exhumation rates (1.25-0.5 cm/yr) soon after the HP event occurred at 133 Ma. During exhumation the metamorphic path exhibit an isothermal decompression during the formation of pargasite + Mg-hornblende + epidote + albite + chlorite at 450-550 °C and < 0.6 GPa during a slab breakoff.

Keywords: eclogite; blueschist; oceanic plateau; rollback; slab breakoff

LISTA DE FIGURAS

DISSERTAÇÃO

Figura 1 - Diagrama de Nb/Y versus Zr/Y utilizado para discriminar basaltos oriundos de platôs oceânicos de MORB e basaltos de arco..... 17

Figura 2 - Mapa simplificado dos Andes do Norte com a localização das principais unidades presentes. As estrelas mostram a localização das ocorrências de rochas de alta pressão existentes. 24

ARTIGO 1 - EARLY CRETACEOUS SUBDUCTION OF AN OCEANIC PLATEAU AT THE NORTHERN ANDES; GEOCHEMICAL, METAMORPHIC, AND COOLING AGE CONSTRAINTS OF THE RASPAS METAMORPHIC COMPLEX

Figure 1 - Schematic map of Ecuador, displaying El Oro Metamorphic Complex and the Raspas Metamorphic Complex (top map). Geological units of the Raspas Metamorphic Complex (lower map). 33

Figure 2 - (a) fine-grained garnets in the eclogites are usually found scattered through the matrix. (b) garnet porphyroblasts with a typical atoll texture with inclusions of amphibole, omphacite, and quartz with minor epidote and rutile in the core. (c) well-developed foliation in a blueschist from the Raspas Metamorphic Complex. The matrix is dominated by elongated glaucophane exhibiting slightly green cores associated with cloudy zoisite and paragonite. (d) garnet blueschist shows large garnet porphyroblasts highly fractured with incipient retrograde influence due to chlorite formation. 56

Figure 3 - Binary diagrams show the geochemical characteristics of some trace elements when compared with Zr (a-f). Notice that, for the most part, the samples follow a general trend. However, some group of samples does not have the same behavior (circled samples in the image). Some are grouped below the main trend (a, b, f), whereas others follow a secondary trend (c, d). Only in one diagram, the samples are scattered (c)... 59

Figure 4 - Primitive mantle-normalized multi-element plot for the eclogites (a), garnet amphibolites, greenschists (b), and blueschists (c) from the Raspas Complex. The field for representative samples from the Caribbean, Ontong Java, and Kerguelen Plateaus

are plotted in each diagram. The data from the plateaus are from the GEOROC database and are available in the appendix Table A.1. 61

Figure 5 - (a) trace element ratio diagram from Raspas metabasites. (b) $(La/Sm)_{pmn}$ versus Zr/Nb ratios. (c) Sm/Yb vs. La/Yb and (d) Th/Y vs. Sm/Th, showed the geochemical characteristics of the mantle source for the Raspas metabasites. 62

Figure 6 - X-Ray images from sample 171. (a) mask image showing the minerals present and their proportion in the analyzed section of the sample. In (b) are the molar fraction of the garnet components; grossular (XGrs), almandine (XAlm), pyrope (XPy), and spessartine (XSpss). The image corresponds to the same image as in (a), but each garnet component is displayed on every quadrant of the image. Moreover, the correspondent color bar is displayed next to the correspondent component. In (c-f) is displayed a sketch of a garnet highlighted in (a), showing the main compositional zones according to each garnet component. The color of each zone corresponds to the mean composition in the color bar from (b). A compositional profile obtained in the XMapTools is also displayed. The gray field corresponds to the standard deviation calculated by the program. (g) The effects of diffusion at the contact between garnet and amphibole are observed in a compositional map of FeO wt% and a profile. They show a striking increase of this oxide at the rims of amphibole and in less proportion on garnet. 65

Figure 7 - Results were obtained through the interactive modelling in the Bingo-Antidote. In (a) are shown the pressure-temperature (P-T) conditions for every metamorphic Stage described in the text. The mineral proportions observed and modeled are shown in (c). The P-T conditions in (a) are superimposed with a pseudosection in (b) with the main mineral curves highlighted and the results of the Zr-in- rutile thermometry. The uncertainty for each Stage is plotted in (d). The circles represent the P-T conditions for a variable composition (Recipe 3) and their respective total quality factor. The dashed field in (d) represents the possible window for the zoisite growth. A possible trajectory is displayed by the black dashed arrow, whereas the gray dashed arrow represents the possible effects of diffusion. The red field represents the high Q_{cmp} for the garnet during Stage III. The quality factors (Q) are a measure of how the modeling got close to the observation, whether the assemblages (Q_{ass}), the volume of the phases (Q_{vol}), or their composition (Q_{cmp}). 68

Figure 8 - (a) La_N/Nd_N vs. Sm_N/Yb_N diagram comparing the Raspas metabasites with the Caribbean and Ontong java Plateaus. (b) Nb/Y vs. Zr/Y diagram shows the Raspas Complex's concordance with plume-related rocks. (c-e) boxplot comparing La_N/Sm_N, Nb/Zr, Nb/La ratios from Kerguelen, Caribbean, and Ontong java plateaus with the Raspas Complex. The data used in the comparison are from the GEOROC database and are available in Table A.1. 73

Figure 9 - Sketch showing the tectonic evolution of the Raspas Complex. From top to bottom: The plateau of the Jurassic age traveled towards the Andean margin until it interacted with the continental margin at the transition Jurassic-Cretaceous. As the plateau arrived at the trench, continental sediments were scrapped and carried towards the mantle. At 133 Ma, due to the low buoyancy of the plateau, a flat slab geometry was formed. At this stage, fluid originated from the dehydration of parts eclogitized and traveled upwards, interacting with the continental sediments incorporated and portions that preserved blueschist assemblages (Raspas Complex). At this point, the slab-pull forces, originated by the portions eclogitized, were so strong that they started to bend and thin the subducted plateau creating a roll-back event. This context created a thermal anomaly reflected in the isobaric heating in the Raspas eclogites. Finally, between 129-123 Ma, the mantle flow originated from the roll-back was the mechanism behind the exhumation of the Raspas Complex. 80

ARTIGO 2 - METAMORPHIC EVOLUTION OF BLUESCHISTS FROM THE RASPAS METAMORPHIC COMPLEX, ECUADOR UNRAVELING THE SUBDUCTION OF OCEANIC PLATEAUS

Figure 1 - Simplified map of the Northern Andes at the segment between Ecuador and Colombia. The stars refer to the location of the Cretaceous HP occurrences on the Northern Andes. 104

Figure 2 - Textural aspects of the blueschists from Raspas Metamorphic Complex (b, d, f, h) with simplified sketches of the textures (a, c, e, g). Garnet blueschists (a, b, e, f) characterized by subidioblastic garnet porphyroblasts exhibiting inclusion trail (S_1) made up of clinozoisite/epidote. The porphyroblasts are wrapped into a foliation S_2 made up of slender clinozoisite and winchite crystals with minor white mica. Locally S_2 foliation exhibit tight folds of a previous S_1 foliation (f). The main blueschist

assemblage is partially replaced due retrograde metamorphism registered by the replacement of garnet by chlorite and albite (c, d) and formation of albite, tremolite, epidote, and chlorite after glaucophane and clinozoisite (g, h). 119

Figure 3 - Textural features and sketches of the analyzed sample 166. (a, b) isolated garnet porphyroblast exhibiting a rotated inclusion trail of S_1 foliation and subidioblastic cores defined by inclusion-rich region. (c, d) omphacite and phengite porphyroblasts after S_2 characteristic of the metamorphic peak at an incipient eclogite-facies metamorphism, notice the albite rims around phengite. 120

Figure 4 - X-ray maps of the main garnet components, grossular (a), pyrope (b), almandine (c), and spessartine (d). 122

Figure 5 - (a) mask image showing the mineral proportion on the analyzed region. (b) Map of Na_{apfu} contents on the M_4 site on amphiboles. (c) Si_{apfu} map on white micas. (d) $Fe^{3+}{}_{apfu}$ on M_3 site of epidote, the outline of garnet crystals is highlighted as dashed white lines, whereas S_1 foliation defined by epidote inclusions is represented by the white line. 125

Figure 6 - Isochemical phase diagram of the analyzed sample on the Na_2O-CaO-FeO-MgO-SiO_2-H_2O (NCFMASH) system. The main mineral tie lines are colored. Mineral abbreviations are Chl – chlorite; Grt – garnet; Ab – albite; Omp – omphacite; Ep – epidote; Pg – paragonite. 126

Figure 7 - Isochemical phase diagram on the chemical system Na_2O-CaO-K_2O-FeO-MgO-SiO_2-H_2O (NCKFMASH). Mineral abbreviations are as on Figure 6, except Lws – lawsonite. 128

Figure 8 - Isochemical phase diagram on the NCFMASH with oxygen in excess. Mineral abbreviations are as on Figure 5.2.7. 130

Figure 9 - Isochemical phase diagram on the NCKFMASH with excess of oxygen. Mineral abbreviations are as on Figure 5.2.7 except Zoi – zoisite 133

Figure 10 - P-T diagram showing a summary of the modelling of garnet growth stages using the GrtMod program on NCFMASH and MCKFMASH. Moreover, a diagram of the resulting garnet volumes on each chemical system are shown. 134

Figure 11 - Simplified isochemical phase diagram of Figures 5.2.6-5.2.9 superimposed with a summary of the P-T evolution on NCFMASH (a), NCKFMASH (b), and considering oxygen in excess (c, d); see text for further discussion. Mineral abbreviations on tie lines are as on Figure 5.2.7. Isopleths of Si_{apfu} on white mica (Wm Si apfu), Na_{apfu} on M_4 of amphiboles (Na_M_4 amp), and $Fe^{3+}{}_{apfu}$ on M_3 site of epidote (Ep Fe_M_3) are also plotted. 137

Figure 12 - A/CNK vs. $Na_2O/(Na_2O+CaO)$ (a) and $CaO/(CaO+FeO)$ (b) showing the compositional factors influencing the formation of eclogites (EC field) and blueschists (BS field). For comparison, geochemical analysis of blueschists (blue circles), eclogites (red square) and garnet amphibolites (black triangle) of the Raspas Metamorphic Complex. Notice that all analysis is grouped together and outside the compositional fields for these rock types. 142

Figure 13 - Resume of the metamorphic, textural, and tectonic evolution from Raspas Metamorphic Complex, see text for further discussion. P-T path from eclogites is plotted as black dashed line for comparison. Act – actinolite, Par – pargasite, Mg-Hbl – Mg-hornblende, Zoi – zoisite, Chl – chlorite, Qz – quartz, Fe-bar – Fe-barroisite, Ab – albite, Ep – epidote, Wm – white mica. 145

LISTA DE TABELAS

ARTIGO 1 - EARLY CRETACEOUS SUBDUCTION OF AN OCEANIC PLATEAU AT THE NORTHERN ANDES; GEOCHEMICAL, METAMORPHIC, AND COOLING AGE CONSTRAINTS OF THE RASPAS METAMORPHIC COMPLEX

Table 1 - Major and trace element analysis of metabasites from the Raspas Metamorphic Complex 38

Table 2 - $^{40}Ar/^{39}Ar$ results and mineralogy of some samples from Raspas Metamorphic Complex. 45

Table 3 - Representative mineral analysis of garnet, omphacite and epidote from the Raspas Metamorphic Complex. The remaining analysis are available as supplementary material (Table A.2)..... 48

Table 4 - Amphibole analysis from the Raspas Metamorphic Complex..... 49

Table 5 - ppm Rutile analysis and temperature calculations. 51

ARTIGO 2 - METAMORPHIC EVOLUTION OF BLUESCHISTS FROM THE RASPAS METAMORPHIC COMPLEX, ECUADOR UNRAVELING THE SUBDUCTION OF OCEANIC PLATEAUS

Table 1 - Electron Microprobe analysis (EMPA) of garnet from the analyzed blueschist. ... 108

Table 2 - EMPA analysis of amphibole..... 110

Table 3 - EMPA analysis of epidote calculated with basis of 12.5 oxygen per formulae..... 111

Table 4 - EMPA analysis of feldspars from sample 166. 112

Table 5 - EMPA analysis of phengitic white mica from sample 166. 113

Table 6 - Paragonite EMPA analysis from sample 166. 114

SUMÁRIO

1 **INTRODUÇÃO** **14**

1.1 APRESENTAÇÃO DA PROBLEMÁTICA E JUSTIFICATIVAS 14

1.2 BASE TEÓRICA 15

1.2.1 Platôs oceânicos **15**

1.3 ALGUMAS CONSIDERAÇÕES SOBRE METAMORFISMO 17

2 MATERIAIS **20**

3 MÉTODOS **21**

3.1 INVESTIGAÇÃO GEOQUÍMICA DOS PROTÓLITOS 21

3.2 ESTRATÉGIA NA INVESTIGAÇÃO DO METAMORFISMO 21

4 GEOLOGIA REGIONAL **23**

5 RESULTADOS **26**

5.1 ARTIGO 1: EARLY CRETACEOUS SUBDUCTION OF AN OCEANIC PLATEAU AT THE NORTHERN ANDES; GEOCHEMICAL, METAMORPHIC, AND COOLING AGE CONSTRAINTS OF THE RASPAS METAMORPHIC COMPLEX 26

5.2 ARTIGO 2: METAMORPHIC EVOLUTION OF BLUESCHISTS FROM THE RASPAS METAMORPHIC COMPLEX, ECUADOR UNRAVELING THE SUBDUCTION OF OCEANIC PLATEAUS 98

6 CONCLUSÕES **156**

REFERÊNCIAS **157**

1 INTRODUÇÃO

1.1 Apresentação da problemática e justificativas

Quando indagados sobre zonas de subducção a primeira coisa que vem à mente para a maioria de nós geocientistas são eclogitos e xistos azuis. Essas rochas de mineralogia e raridade singulares são objeto de obstinação de pesquisadores, não só pela beleza e exotismo mas também pelas informações cruciais nelas contidas que nos ajudam a entender o funcionamento da tectônica de placas e seu papel na dinâmica terrestre.

Por exemplo, em apenas algumas décadas desde a consolidação da teoria de tectônica de placas conjuntamente ao desenvolvimento de modelagem termodinâmica possibilitaram entender a relação entre as reações de desidratação durante a formação de eclogitos e a geração de arcos magmáticos (STERN, 2002). Permitiu mensurar a escala de tempo decorrida durante a exumação de rochas de alta pressão (GERYA; STOCKHERT, 2002; GIRAULT *et al.,* 2022), ou ainda os mecanismos por trás do ciclo geoquímico de certos elementos (ZHENG, 2019). Os exemplos mencionados acima demostram em parte o caminho até aqui percorrido. Entretanto, ainda há muitos questionamentos a serem respondidos. Uma dessas incógnitas diz respeito à interação de platôs oceânicos com zonas de subducção.

Platôs oceânicos são porções da crosta oceânica mais espessos que o normal podendo chegar a > 20km de espessura. Sua formação é geralmente atribuída à ascensão de plumas mantélicas e eventual derrame no assoalho oceânico (KERR *et al.,* 2002). Com exceção da ilha de Ontong Java em que elas ocorrem de forma subaérea e por coleta em programas de sondagem, boa parte do registro acessível vem de fragmentos acrescidos durante sua interação com margens ativas. Um dos melhores exemplos é o Platô do Caribe que exibe eventos de acreção na margem sul-americana desde o Cretáceo Superior (VALLEJO *et al.,* 2006).

Diversos modelos numéricos investigaram a interação de platôs oceânicos com zonas de subducção. Dos quais grande parte sugere que essas feições mesmo mais espessas e menos densas do que uma placa oceânicas ‘normal’, pode ser subduzida, corroborado por evidências geofísicas (LIU *et al.,* 2021). Contudo, a única ocorrência descrita, até o presente momento, de eclogitos cujo protólito seja oriundo de um platô oceânico está no cinturão orogênico Venedian-Cambriano, na região de Gorny Altai, Sul da Rússia. Entretanto, nessa região o platô oceânico foi desmembrado durante os estágios iniciais de subducção e posteriormente incorporados na *mélange* (OTA *et al.,*

2002; 2006). Portanto sua trajetória metamórfica registra sua evolução dentro da *mélange* e não a subducção em si do platô oceânico.

Durante o Cretáceo, a cordilheira dos Andes foi palco de diversos eventos acrescionários contemporâneo a formação de complexos de alta pressão que abrangem regiões da Colômbia até o sul do Equador (SPIKINGS *et al.,* 2015). Dentre essas ocorrências, destaca-se as rochas de alta pressão do Complexo Raspas, na porção sul da Cordilheira Central (GABRIELE, 2002), no Equador. Esse complexo é envolto em controvérsias a respeito da origem de seu protólito. Trabalhos pioneiros de geoquímica propuseram que se trataria de um fragmento de platô oceânico (ARCULUS; LAPIERRE e JAILLARD, 1999; BOSH *et al.,* 2002), entretanto essa hipótese foi rebatida argumentando diferentes assinaturas dos protólito, sendo xistos azuis originados de um *seamount* enquanto um típico MORB para os eclogitos (JOHN *et al.,* 2010).

Desde então, os trabalhos que tratam da evolução tectônica dos Andes do Norte tratam o Complexo Raspas seguindo a proposta de John et al., (2010). Entretanto, apesar de ter uma aparente ampla aceitação na comunidade científica, nenhum trabalho posterior testou essa hipótese ou questionou a metodologia utilizada.

Essa contribuição se propõe a reabrir o questionamento da origem e evolução das rochas de alta pressão do Complexo Raspas. A abordagem utilizada será focada na apresentação de novos dados geoquímicos e compilação dos dados previamente publicados para poderem então ser comparados com o banco de dados existentes de rochas de platô oceânico. Adicionalmente dados inéditos de química mineral e mapas composicionais serão utilizados para desvendar a trajetória metamórfica testemunhada por essas rochas. Com isso, pretende-se compreender o reflexo metamórfico originado durante a subducção de platôs oceânicos e como esse processo afetou a evolução dos Andes do Norte durante o Cretáceo.

1.2 Base teórica

1.2.1 Platôs oceânicos

A crosta oceânica em geral exibe espessura bastante homogênea. Contudo, algumas porções são anomalamente mais espessas, as quais podem abranger áreas da escala de centenas de quilômetros e espessuras de algumas dezenas de quilômetros, denominadas platôs oceânicos. Devido à grande quantidade de magma necessário na geração dessas feições, a hipótese mais aceita

para sua origem é atribuída a ascensão de plumas mantélicas (CAMPBELL, 2007). Nesse caso, à medida que a porção superior da pluma chega próximo a superfície, sofre achatamento e subsequente derrame sobre uma vasta extensão do assoalho oceânico (KERR, 2014).

Como o registro geológico dessas feições são geralmente encontradas devido a interação de platôs oceânicos com uma margem ativa, ainda há muito que se descobrir sobre sua estrutura e litologias nas porções mais inferiores. Por exemplo, o Platô de Ontong Java é encontrado de forma subaérea nas Ilhas Salomão, pois quando o platô colidiu com o Arco de Java, houve inversão da polaridade da subducção, causando soerguimento do platô (SUN *et al*., 2021). Contudo, mesmo somado a programas de sondagem o registro disponível não passa de algumas centenas de metros.

O platô oceânico mais conhecido em termos de estrutura e composição é o Platô do Caribe. O consenso científico atual propõe que esse platô se originou no Cretáceo na placa Farallon e que durante sua viagem para nordeste foi deixando diversos fragmentos ao longo na margem sul-americana desde o Equador à Venezuela.

A identificação de platôs oceânicos fica mais difícil à medida que se recua no tempo geológico, pois boa parte de suas estruturas primárias são perdidas por eventos posteriores a sua acreção. Portanto, na ausência de outras feições-diagnóstico, a compreensão da geoquímica de platôs oceânicos é fundamental para identificá-lo no registro geológico.

Platôs oceânicos geralmente possuem composição basáltica com teores de MgO < 11wt. %, contudo não é incomum observar altos teores no Platô do Caribe (KERR *et al*., 2000; MgO > 14 wt. %) comumente com a presença de picritos e komatiitos, além de exibir um característico padrão plano em diagramas normalizados de elementos terras raras (ETR's). Há uma aparente relação entre os basaltos ricos em MgO do Platô do Caribe com variações no conteúdo de terras raras leves (KERR, 2014).

Podem ser distinguidos de basaltos de dorsal oceânica (sigla MORB em inglês) pela ausência de empobrecimento dos terras raras leves ($[La/Nd]_N$ ~1; subscrito $_N$ refere-se a valores normalizados aos de condritos) e maiores valores de Nb/Y. Por geralmente não serem formados em grandes profundidades (i.e., acima do campo de estabilidade da granada), os platôs oceânicos predominantemente possuem menores valores de La/Y, Nb/Zr, $(Sm/Yb)_N$ do que ilhas oceânicas

(KERR *et al*., 2000). Contudo, algumas porções do Platô do Caribe exibirem assinatura rica em elementos incompatíveis similar a basaltos de ilhas oceânicas.

O principal diagrama discriminatório de platôs oceânicos é o Nb/Y-Zr/Y (FITTON *et al*., 1997; Figura 1), em que esses basaltos plotam ao longo de um *trend* de rochas do tipo Icelandito, distinguindo-as de basaltos do tipo MORB. Apesar de haver sobreposição com o campo de basaltos de arco, essas rochas são facilmente distinguidas pelas maiores razões $(La/Nb)_{pmn}$ (> 1; valores normalizados a composição do manto primitivo de SUN & MCDONOUGH, 1989).

Figura 1 Diagrama de Nb/Y versus Zr/Y utilizado para discriminar basaltos oriundos de platôs oceânicos de MORB e basaltos de arco.

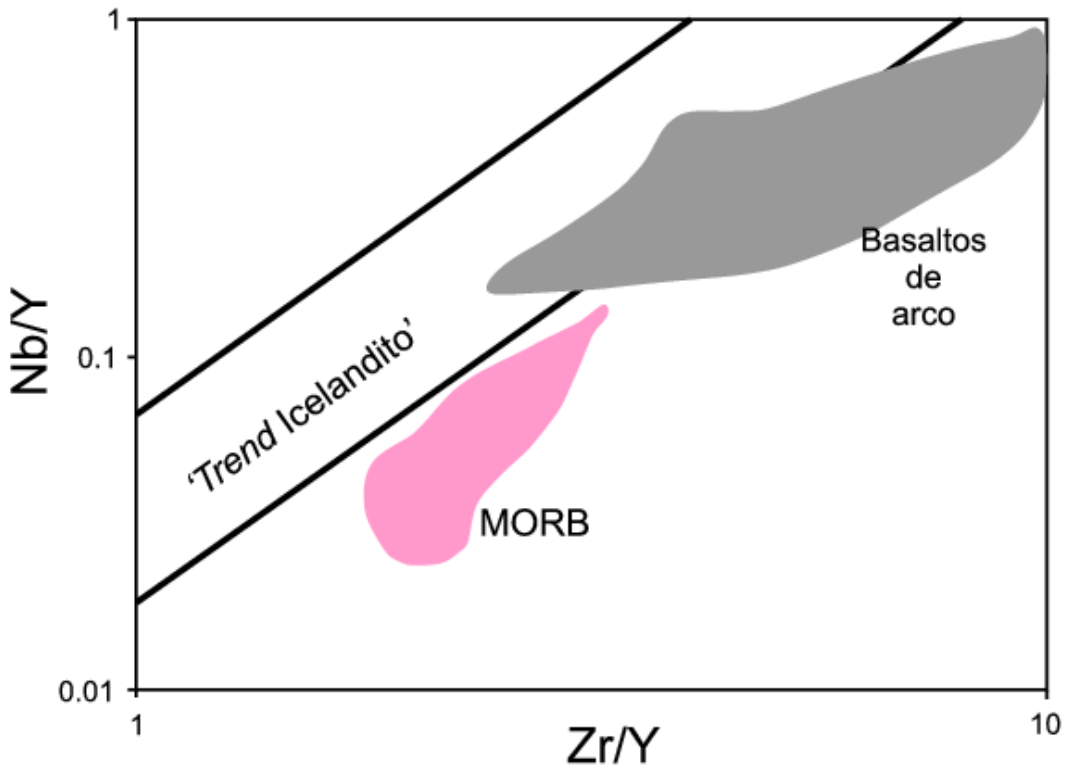

Fonte: Diagrama de Fitton et al., 1997. Campo com dados de basaltos de arco são de Marriner & Millward (1984) e Thrilwall et al. (1996), enquanto MORB representa dados de Mahoney et al., 1994.

1.3 Algumas considerações sobre metamorfismo

Assim como qualquer sistema geológico, rochas metamórficas são fundamentalmente sistemas químicos constituído por fases minerais. Contudo, essas rochas se diferenciam das demais

por serem produto de transformações químicas a partir de processos físicos (i.e., fluxo térmico do/para o sistema e compressão/descompressão no sistema) em uma rocha preexistente. No século XX cientistas observaram que certas fases minerais coexistem sob certas condições de pressão (*P*) e temperatura (*T*) que condizem com intervalos discretos em que a rocha atingiu o equilíbrio (e.g., ESKOLA, 1915). Esse princípio foi o que fundamentou todo o conceito de fácies metamórficas e o desenvolvimento da petrologia metamórfica em si, contudo esse conceito deve ser aplicado com algumas precauções.

Ao estudarmos mudanças de estado físico de uma fase em sistemas simples, como por exemplo da água, os componentes que representa esse sistema são restritos, hidrogênio e oxigênio (nesse caso não levo em conta que no sistema podem ocorrer H^+ e OH^-). Enquanto, em sistemas mais realísticos, digamos um metapelito, o sistema pode ser representado por 6 ou até mais componentes (e.g., TiO-MnO-K_2O-FeO-MgO-Al_2O_3-SiO_2-H_2O-CO_2), o que dificulta bastante entender o sistema durante mudanças de fase. Portanto, é comum simplificarmos o sistema eliminando alguns componentes pouco representados na rocha ou limitado a certas fases minerais.

Deve-se ter também bastante atenção com a presença de minerais zonados (e.g., granada). Esses minerais podem ser uma ‘faca de dois gumes’ pois, ao mesmo tempo em que seu zoneamento e inclusões dão indícios de variações no sistema durante eventos metamórficos pretéritos, não dá para ter certeza do grau de equilíbrio (e se houve) entre as inclusões e das inclusões com o mineral que as inclui, o que depende muito do viés de quem o interpreta. Adicionalmente, como esses minerais comumente ocorrem como porfiroblastos, os elementos consumidos durante seu crescimento são fracionados da matriz, afetando as curvas de potencial químico em suas proximidades. Ou seja, gerando variações na composição efetiva no sistema ao longo do metamorfismo (e.g., SPEAR & WOLFE, 2018).

Talvez o mais importante seja compreender se o conceito de equilíbrio é aplicável a rocha metamórfica objeto de estudo na escala de trabalho escolhida. Via de regra, utiliza-se a petrografia tradicional para ver relações entre minerais e descobrir possíveis relações de equilíbrio. Contudo, nem sempre essa relação é clara. Por exemplo, como previamente dito, a petrologia metamórfica é ditada pelo equilíbrio termodinâmico durante as reações, entretanto, isso desconsidera que em sistemas reais quando um reagente é consumido, seus componentes necessitam ser transportados (independentemente da escala) para nuclear o(s) produto(s). O que consome energia, comumente

não contabilizada durante cálculos entre pares mineralógicos ou em diagramas isoquímicos de fase. Ou seja, mesmo o sistema atingindo equilíbrio suas texturas não necessariamente exibem relações de equilíbrio. Essa energia adicional funciona como barreira para as reações em sistemas metamórficos, denominada barreiras cinéticas (WALTHER e WOOD, 1984; RUBIE, 1998). Seus efeitos podem ser observados em várias escalas e de diversas formas, o que pode refletir em pequenas discrepâncias entre as condições *P-T* calculadas e as reais (CARLSON; PATTISON e CADDICK, 2015).

Os exemplos apresentados acima servem para esclarecer a complexidade de sistemas metamórficos. Desde a coleta da amostra ao processamento dos dados estão sujeitos a influências de viés por parte do pesquisador e limitações geradas pela quantidade de fatores, em escalas diversas, que influenciam no resultado. Portanto deve-se estar ciente de que todos trabalhos que investigam o metamorfismo estão inerentemente associados a erros, contudo isso não significa que todos os trabalhos sobre metamorfismo são inválidos. Pois, mesmo que em um mesmo complexo tenham diversos trabalhos que apontam condições *P-T* aparentemente distintas pelos motivos acima mencionados, quando postos lado a lado percebe-se que esses trabalhos mostram um padrão evolutivo similar (e.g., KLEMD ET AL., 2015)

2 MATERIAIS

As amostras utilizadas fazem parte do acervo pessoal do Professor Andres Bustamante-UFPE utilizado em aulas de Petrologia Metamórfica do curso de Geologia da Universidade de São Paulo (USP) e na Universidade Nacional da Colômbia. Sua coleta foi realizada em 2005 (acervo USP) e em 2017 (acervo da Universidade Nacional da Colômbia), concentrada nas margens do Rio Raspas devido a extensa cobertura vegetal.

3 MÉTODOS

3.1 Investigação geoquímica dos protólitos

Para testar as hipóteses existentes da origem dos protólito do Complexo Raspas utilizou-se análises geoquímicas de 14 amostras; sendo 4 eclogitos, 3 xistos azuis, 5 granada-anfibolitos, e dois xisto verdes. O critério de escolha levou em conta a ausência de veios e superfícies alteradas por diagênese. As amostras foram então moídas e pulverizadas (90% < 200 mesh) seguido por digestão em ácido (0.25 g por amostra) no Instituto de Geociências da Universidade de São Paulo. Os elementos maiores foram analisados em um espectrometro de emissão com plasma indutivamente acoplado (ICP-ES), enquanto os elementos terras raras utilizou-se um espectrometro de massas com plasma indutivamente acoplado (ICP-MS), ambos do Activation Laboratories Ltd. (Actlabs), Canadá. Devido a pequena quantidade de dados também compilou análises geoquímicas previamente publicadas (18 análises no total) no referido complexo para melhor interpretação de padrões geoquímicos.

Adicionalmente, selecionou-se dados dos principais platôs oceânicos (Ontong Java, Kerguelen, Caribe) presentes no banco de dados do GEOROC para comparação. Apenas foram selecionados dados publicados em revistas científicas que não estejam faltando elementos chave na interpretação.

3.2 Estratégia na investigação do metamorfismo

A principal estratégia utilizada nesse trabalho envolve o modelamento termodinâmico interativo utilizando o BINGO-ANTIDOTE, extensão do programa XMapTools (versão 3.4 disponível em www.xmaptools.com) conjuntamente a modelamento termodinâmico no TERIAK-DOMINO (versão 11.03.2020, disponível em: https://titan.minpet.unibas.ch/minpet/theriak/theruser.html) e independente termometria com o conteúdo de Zr em rutilo.

O THERIAK-DOMINO utiliza um método denominado G-minimização; que em linhas gerais fixa a *P*, *T* e a composição do sistema enquanto o algoritmo do programa lista possíveis assembleias cujo $\Delta G_{Formação}$ chegue a um mínimo local. Em seguida todas as assembleias cujo $\Delta G_{Formação}$ seja maior que esse mínimo local serão descartadas, limitando o número de fases consideradas nos cálculos subsequentes. Esse processo se repete até que o G do sistema seja o mínimo possível, resultando nas fases minerais estáveis nessas condições (DE CAPITANI &

BROWN, 1987). Contudo, a principal limitação desse programa, e dos diagramas isoquímicos de fase em geral, diz respeito a composição química efetiva durante cada estágio da evolução metamórfica (e.g., LANARI e ENGI, 2017).

Agora, considere a possibilidade de estabelecermos a composição reagente, assembleia mineral e proporção modal durante vários estágios de sua evolução metamórfica. Considere ainda utilizar a composição efetiva para modelar as fases minerais, comparando-as com as observações feitas em sua amostra, resultando em melhor precisão das condições *P*-*T* em que as transformações minerais sofridas pela rocha ocorreram. Essa é a proposta do BINGO-ANTIDOTE. Essa extensão consegue fazer a conexão entre a robusta ferramenta de processamento de imagens composicionais no XMapTools e o algoritmo de G-minimização do THERIAK-DOMINO.

Para detalhes sobre o funcionamento e os cálculos por trás do BINGO-ANTIDOTE e THERIAK-DOMINO sugere-se a leitura dos trabalhos de Duesterhoeft e Lanari (2020) e de Capitani e Petrakakis (2010), respectivamente.

No segundo artigo utilizo uma estratégia um pouco diferente. Devido à complexidade textural exibida pelo xisto azul a utilização do BINGO-ANTIDOTE fica prejudicada. Por depender que o usuário defina quais zonas composicionais de cada mineral que estava em equilíbrio durante a trajetória metamórfica a sua utilização nesse caso específico fica muito dependente do viés humano de quem interpretou a rocha.

Para o xisto azul foi decidido a utilização de uma abordagem mais tradicional com a utilização de diagramas isoquímicos de fase (pseudo-seções) no THERIAK-DOMINO, modelagem de nucleação e crescimento de granada com o GrtMod (LANARI *et al.*, 2017).

4 GEOLOGIA REGIONAL

Os Andes do Norte caracterizam-se por um sistema orogênico composto por três cadeias montanhosas (Oriental, Central e Ocidental) separadas por dois importantes vales que cortam de norte a sul regiões que compreendem a atual Colômbia. Contudo, na porção sul, onde fica o atual Equador, essa configuração muda para uma única cadeia montanhosa denominada Cordilheira Real. Essas regiões compartilham estruturas e rochas de origem e idades semelhantes, sendo comumente consideradas contínuas.

Durante o Mesozoico, os Andes do Norte foi palco de um evento de subducção contínua iniciado no Jurássico seguido de eventos acrescionários de terrenos alóctones durante o Cretáceo (SPIKINGS et al., 2015).

Entre o Jurássico Médio e o Cretáceo Inferior ocorreram algumas mudanças na dinâmica da subducção. A subducção tornou-se oblíqua com uma notável diminuição do volume de magma produzido (BUSTAMANTE et al., 2016). O que culmina durante a transição Jurássico-Cretáceo na mudança de um regime extensional (MALONEY et al., 2013), com formação de crosta oceânica no back-arc, para um regime compressional durante o fechamento dessas bacias (VILLAGOMÉZ et al., 2011; CARDONA et al., 2020).

Nesse período, os principais eventos metamórficos concentram-se no cinturão metamórfico a W do arco magmático. O evento metamórfico regional de idade entre 157 e 146 Ma (BLANCO-QUINTERO et al., 2014) foi responsável por condições de *P-T* em torno de 0.8 GPa e 550-580 °C no Complexo Cajamarca (BLANCO-QUINTERO et al., 2014) e 0.45 GPa e 700 °C no sul dos Andes Colombianos (RESTREPO et al., 2021). Pouco após esse evento, no Cretáceo Inferior, um importante evento metamórfico foi responsável pela formação de uma série de ocorrências de eclogitos e xistos azuis ao longo da Cordilheira Central. Ocorrido entre 120-130 Ma compreende xistos azuis com lawsonita na região de barragán e lawsonita eclogitos na região conhecida como Pijao, ambos na Colômbia. O foco desse manuscrito será a ocorrência existente no sul do Equador no Complexo Raspas. A qual compreende eclogitos e xistos azuis cuja idade marca exatamente o início desse evento de alta pressão do Cretáceo em ~130 Ma (Figura 2).

Figura 2 Mapa simplificado dos Andes do Norte com a localização das principais unidades presentes. As estrelas mostram a localização das ocorrências de rochas de alta pressão existentes.

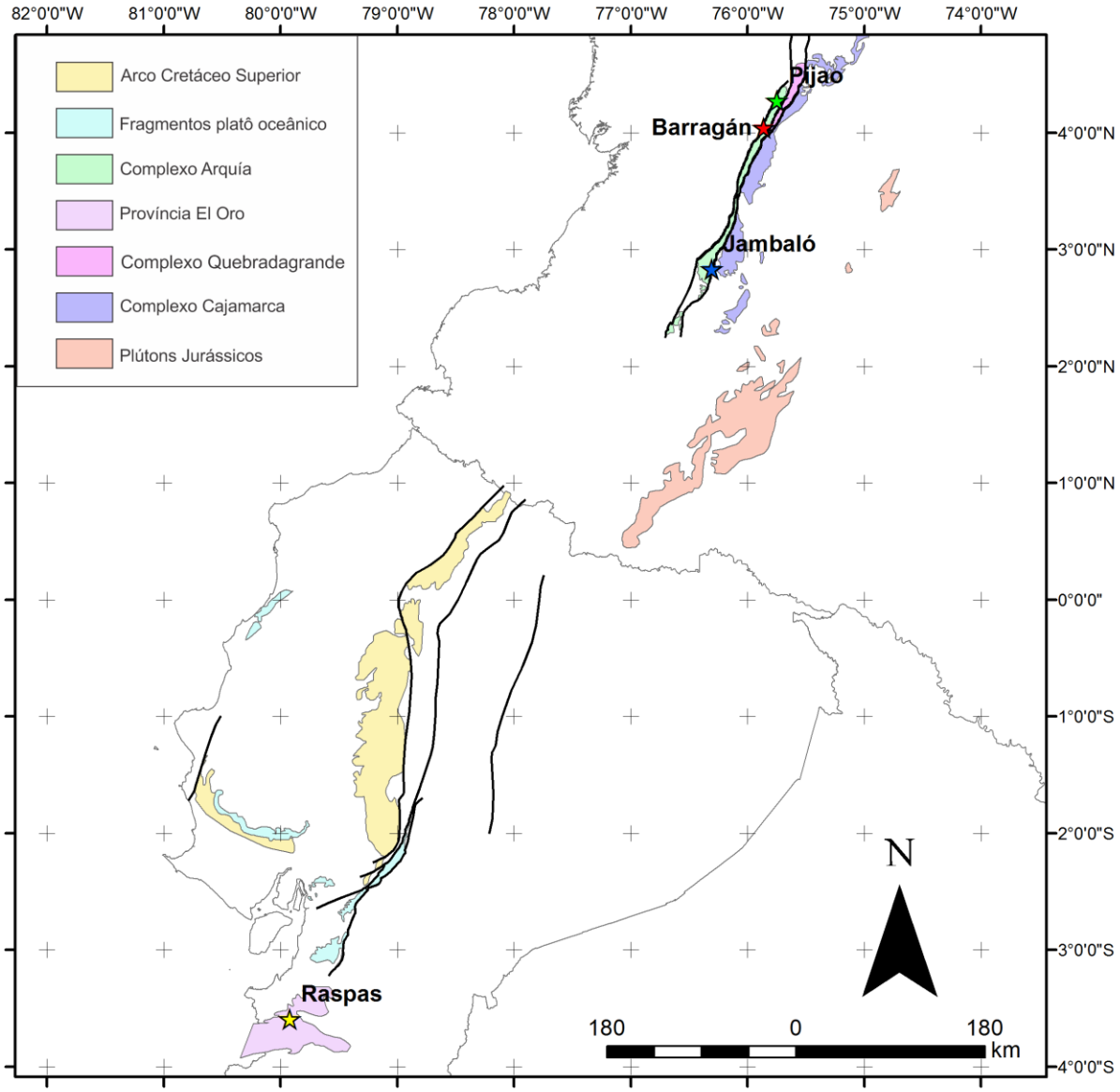

Fonte: O autor

O Complexo Raspas está inserido no sul do Equador na região conhecida como Província El Oro ou Complexo Amotape. Para evitar confusões de nomenclatura essa região será referida durante o trabalho como Província El Oro, pois denota uma denominação mais abrangente. Essa

província é considerada de carácter parautóctone, originada por uma rotação e deslocação dessa região durante o Cretáceo (SPIKINGS ET AL., 2005). É formado por diversos complexos metamórficos de idade Triássica a Cretácea e origens distintas. O Complexo Raspas é limitado a norte pela zona de cisalhamento La Palma-El Guayabo dos paragnaisses de baixo grau do Terreno Birón, enquanto ao sul encontra-se em contato tectônico com xistos azuis e xistos verdes da unidade Arenillas-Panupali, ambos de idade Triássica (GABRIELE, 2002). Pode ser subdividido em duas unidades, Raspas e El Toro, que são limitadas por uma zona de cisalhamento dúctil. A unidade Raspas compreende eclogitos e xistos azuis associados a metapelitos com a associação granada-cloritóide-cianita, e eventual presença de litotipos que exibem incipiente retrometamorfismo como xistos verdes e granada anfibolitos. A unidade El Toro é composta por metaperidotitos exibindo graus variados de serpentinização, além de ser cortados por diques anfibolíticos (GABRIELE, 2002).

5 RESULTADOS

5.1 **Artigo 1:** Early Cretaceous subduction of an oceanic plateau at the Northern Andes; geochemical, metamorphic, and cooling age constraints of the Raspas Metamorphic Complex

Em uma parceria com pesquisadores de universidades da Colômbia confirmamos a hipótese de que o protólito do Complexo Raspas é oriundo de um platô oceânico. A partir desse achado, utilizamos modelamento termodinâmico interativo para compreender a resposta do metamorfismo durante a subducção e eventual exumação de platôs oceânicos. Esse trabalho foi submetido a revista Lithos em 14 de setembro de 2022. Situação atual, sob revisão.

Early Cretaceous subduction of an oceanic plateau at the Northern Andes; geochemical, metamorphic, and cooling age constraints of the Raspas Metamorphic Complex

Salviano da Silva[* a, b], Andres Bustamante[b], Camilo Bustamante[c], Agustín Cardona[d], Caetano Juliani[e]

[a]Universidade Federal de Pernambuco, Departamento de Geologia, Programa de Pós-Graduação em Geociências, Av. da Arquitetura, s/nº, CEP 50740-550, Recife, PE, Brazil.

[b]Departamento de Geologia, Universidade Federal de Pernambuco, Av. da Arquitetura s/nº, CEP 50740-550, Recife, PE, Brazil

[c]Escuela de Ciencias Aplicadas e Ingeniería, Universidad EAFIT, Carrera 49 N° 7 Sur-50, Medellín, Colombia

[d]Departamento de Procesos y Energía, Universidad Nacional de Colombia, Carrera 80 N° 65-223, Medellín, Colombia

[e]Instituto de Geociências, Universidade de São Paulo, Rua do Lago 562, CEP 05508-080, São Paulo, SP, Brazil

[*]Corresponding author.

E-mail: salviano_pereira@hotmail.com (S. da Silva)

ABSTRACT

The Raspas Metamorphic Complex is a high-pressure unit dominated by the presence of eclogites, blueschists, and metapelites with minor greenschists and garnet amphibolites. This unit represents the southernmost expression of a Cretaceous high-pressure belt that extends from Ecuador to Colombia. Although their geochemistry and ages are relatively well known, metamorphic constraints are lacking. Moreover, interpretations for the origin of their protolith are still unclear, thus, obscuring their role in the tectonic evolution of the Northern Andes in the Cretaceous.

In this work, we present new geochemical, metamorphic, and cooling age constraints to understand the protolith, metamorphic conditions, and the tectonic reflex of this feature to the Northern Andes. Their geochemistry reveals rocks with N- to E-MORB signature with trace element ratios characteristic of a heterogeneous mantle source, similar to oceanic plateau lavas. Moreover, they exhibit a continuous variation where the blueschists originated from a deep enriched source, similar to the primitive mantle, whereas eclogites are similar to MORB.

Interactive thermodynamic modeling of an eclogite reveals a low T/P gradient of ~406 °C/GPa during the formation of the assemblage garnet$_{(core)}$, quartz, katophorite, and omphacite cores around 598 °C and 1.43 GPa, followed by the formation of the atoll garnets and zoisite at 661 °C and 1.63 GPa, probably around 133 Ma. Peak metamorphic conditions were attained after isobaric heating at 709 °C and 1.61 GPa resulting in the assemblage of garnet $_{(rim)}$, zoisite$_{(rim)}$, omphacite$_{(rim)}$, and katophorite. Ar/Ar ages around 129 Ma indicate fast exhumation rates of 1.25 to 0.5 cm/yr.

Lastly, we propose that the Raspas Metamorphic Complex represents the interaction of the South American plate with an oceanic plateau during the Early Cretaceous. During the early stages of subduction, it created a flat slab geometry around 130 Ma. As the plateau was transformed to eclogite, the decrease in buoyancy caused an increase in subduction dip during a regional roll-back at 129-123 Ma, which was the same mechanism that triggered the exhumation along the high-pressure belt.

Keywords: Eclogite, oceanic plateau, subduction, Andean Orogeny, rollback

INTRODUCTION

The high-pressure (HP) metamorphic rocks (i.e., eclogites and blueschists; Maruyama et al., 1996) that commonly occur in subduction zones are the key to unraveling the processes related to the interaction of oceanic crust with the mantle at great depths (Ernst and Liou, 2008). Additionally, enabling the understanding of the mechanisms behind the formation of arc magmatism (Zheng and Zhao, 2017; and references within), transport of water to the mantle (Sheng and Gong, 2017), recycling of crustal material (both oceanic and continental), and ultimately the mantle dynamics; thus, functioning as a window to the interior of our planet.

Investigating their protoliths can give insights into the character of the upper and lower plate history, especially the features of the oceanic crust that are being subducted or the incorporation of sediments or fore-arc crustal fragments from the upper plate (e.g., Cloos and Shreve, 1988a; 1988b). Additionally, their pressure-temperature-time path (P-T-t) is essential for determining the time scale, depth, and changes in the tectonic regime experienced by these rocks during their travel from great depths to shallow portions of the crust (e.g., Ernst, 1988; Platt, 1993).

The formation of the Andean Cordillera has been related to long-term subduction for almost 200 Ma (Ramos, 2009). During their activity, it registered several HP rocks outcropping from Chile to Colombia, ranging from the Cretaceous to the Cenozoic age (e.g., Avellaneda-Jimenez et al., 2021; Bustamante and Bustamante, 2019; John et al., 2010; Hyppolito et al., 2015). That has been fundamental for understanding how this subduction zone and its precursors evolved through time (e.g., Spikings et al., 2015).

In the Northern Andes, the HP metamorphic rocks form a discontinuous belt developed during the Early and Late Cretaceous. They are exposed in the western flank of the Central Cordillera of

Colombia (Barragán, Pijao and Jambaló: Bustamante et al., 2020; Avellaneda et al., 2021) and at the El Oro Province of Ecuador (Raspas Metamorphic Complex; John et al., 2010). However, the limited outcrops of blueschists and eclogites in the northern Andes have difficulted their study. Such HP metamorphic rocks have been considered linked to the complex Caribbean-Pacific and South American plates interactions during the Cretaceous (Bustamante and Bustamante et al., 2019).

The Raspas Metamorphic Complex in the El Oro Province of Ecuador is one of the well-studied HP rocks from the Northern Andes regarding their protolith and age. Although different interpretation was proposed for the origin of the protolith, whether as a mix between MORB and subducted seamounts (John et al., 2010) or as an oceanic plateau fragment (Arculus et al., 1999; Bosch et al., 2002). These contrast with the more limited constraints on the metamorphic evolution, which could be key to understanding the subduction dynamics, and exhumation mechanisms in the southern portion of the Northern Andes.

This contribution provides new whole rock geochemistry, Ar-Ar geochronology, mineral analyses, and X-ray maps. The geochemical data were combined with previous work to constrain the origin of the protolith of the eclogitic rocks of the Raspas Metamorphic Complex. Moreover, interactive thermodynamic modeling coupled with geochronologic methods was used to constrain the timing and conditions of metamorphism to discuss the evolution of the subduction zone in which the Raspas Metamorphic Complex was formed and its place within the Northern Andean Cretaceous tectonics.

GEOLOGICAL SETTING

The Mesozoic history of the subduction zone at the northwestern margin of South America is characterized by a change from an extensional regime during the transition between Late Jurassic to Early Cretaceous with the incipient formation of oceanic crust (Zapata et al., 2019), to a compressional regime during the closure of a back-arc basin at < 114 Ma (e.g., Villagoméz et al., 2011).

In the Late Cretaceous, a series of accretional events occurred during the interaction of the Caribbean Plateau with the South American margin (Vallejo et al., 2006; Villagomez et al., 2011; Zapata et al., 2020). This event leaves vestiges in portions of western Ecuador, Colombia, and Venezuela's Caribbean region. In Ecuador they are represented by predominantly mafic volcanic and plutonic rocks of the Pallatanga (~87 Ma; Vallejo et al., 2009), Piñón (~98 Ma; Vallejo et al., 2019), and San Juan Units (123-87 Ma; Vallejo et al, 2006).

High-pressure metamorphic records of the Early to Late Cretaceous have been found in the Northern Andes of Colombia and Ecuador. They provide a record of the different subduction regimes experienced by the South American or the Caribbean plates before or during their interactions (Fig. 1; e.g., Bustamante and Bustamante, 2019).

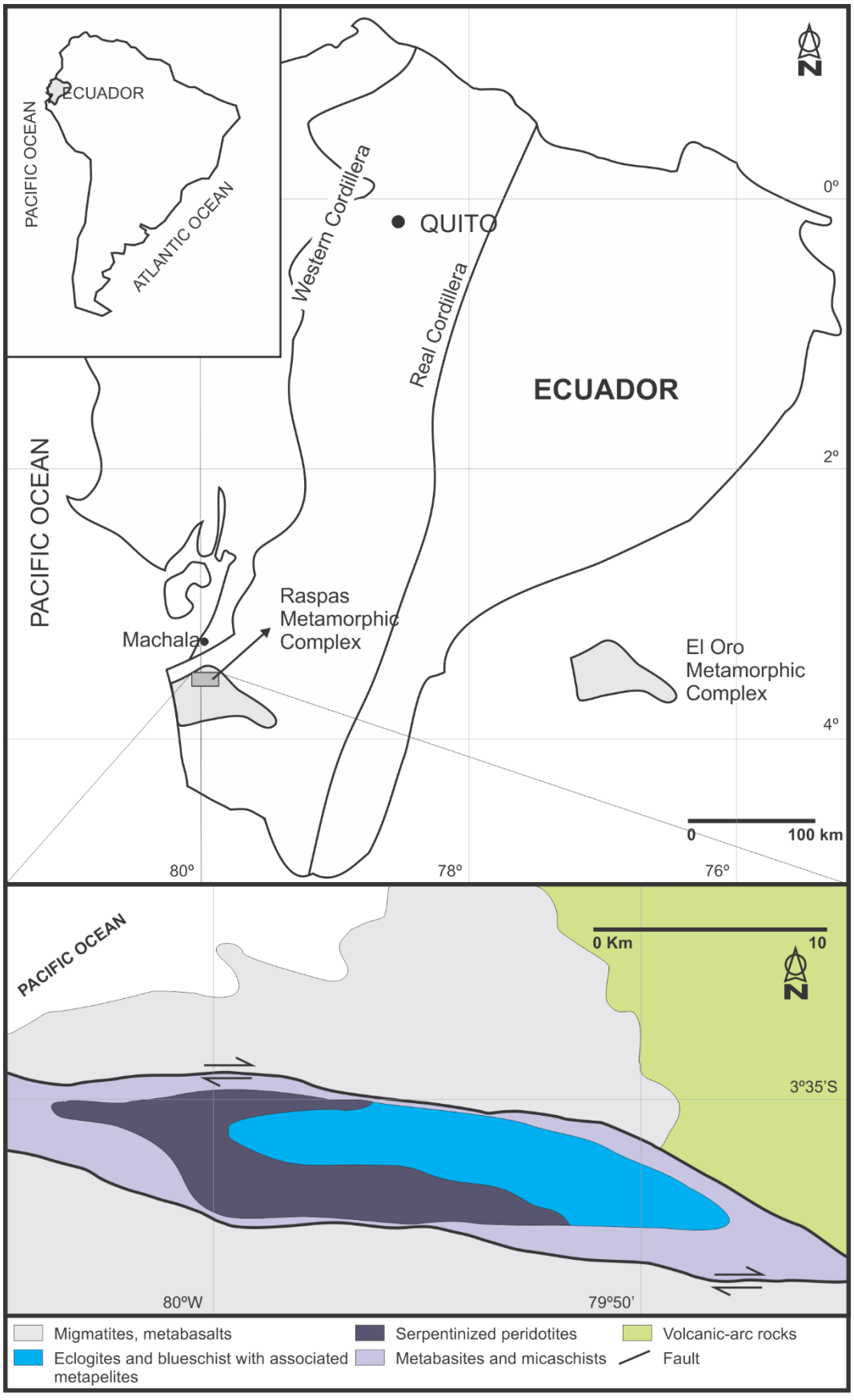
ECUADOR
PACIFIC OCEAN
ATLANTIC OCEAN
Western Cordillera
Real Cordillera
QUITO
ECUADOR
PACIFIC OCEAN
Machala
Raspas
Metamorphic
Complex
El Oro
Metamorphic
Complex
0°
2°
4°
0
100 km
80°
78°
76°
PACIFIC OCEAN
0 Km
10
3°35'S
80°W
79°50'
Migmatites, metabasalts
Eclogites and blueschist with associated metapelites
Serpentinized peridotites
Metabasites and micaschists
Volcanic-arc rocks
Fault

Figure 1 Schematic map of Ecuador, displaying El Oro Metamorphic Complex and the Raspas Metamorphic Complex (top map). Geological units of the Raspas Metamorphic Complex (lower map). Modified from Aspden et al. (1995) and Bosch et al. (2002).

In the western flank of the Central Cordillera of Colombia, the Early Cretaceous eclogites and blueschists of the Barragán and Pijao areas with MORB-like protolith and peak metamorphism at ~120-129 Ma contrast with the Late Cretaceous Jambaló blueschists with supra-subduction signatures and a ca. 64 Ma age of metamorphism (see review in Bustamante and Bustamante, 2019). The former is related to the subduction of the Farallón plate under the northwestern margin of South America. In contrast, the latter relates to Caribbean-South America interactions (see review in Bustamante and Bustamante, 2019).

The geological extension of the Colombian Andes on Ecuador is marked by a metamorphic basement made up of metapelites, metavolcanic and plutonic rocks from the Cordillera Real. In the coastal region in Southern Ecuador, a mountain expression named Amotape Massif exposes Triassic to Cretaceous units bounded by E-W structures that define the whole massif. These units encompass oceanic-related units such as Triassic blueschists (Arenillas-Panipali Unit; 225 Ma; Gabriele, 2002) and metabasites (Piedras Amphibolite Unit; 226 Ma; Gabriele, 2002), and Early Cretaceous HP ophiolite (Raspas Metamorphic Complex; 133 Ma; John et al., 2010). In addition, these units are surrounded by Triassic low-grade metapelites, paragneisses, and migmatites from the Tahuim Group and Birón Terrane (Aspden et al., 1995; Gabriele, 2002).

Geology of the Raspas Metamorphic Complex

The Raspas Metamorphic Complex is part of the El Oro Province, located in the southern portion of the Cordillera Real of Ecuador (Figure 1). It is bounded to the north by the La Palma-El Guayabo

shear zone with the low-pressure para-gneisses from the Birón Terrane and in tectonic contact with the greenschist and blueschists from Arenillas-Panupali Unit at the south (225 Ma; Gabriele, 2002), the Raspas Metamorphic Complex encompasses high-pressure metabasites and metapelites from the Raspas Unit and metaultramafic rocks from El Toro Unit (Figure 1; Gabriele, 2002). The Raspas Unit represents an excellent exposure of nearly pristine blueschists and eclogites, locally interlayered with garnet-chloritoid-kyanite metapelites. Bounded by a ductile shear zone with the Raspas Unit, the El Toro Unit is composed of metaperidotites with variable degrees of serpentinization crosscut by amphibolitic dikes (Gabriele, 2002).

Protoliths for the metabasic rocks have been related to different oceanic-related environments, including oceanic plateau (Arculus et al., 1999; Bosh et al., 2002) or a mix of MORB and seamount environments (John et al., 2010). The HP metapelites have been interpreted as derived from the erosion of an old continental crust and, therefore, incorporated with the metabasites in the subduction channel (Bosh et al., 2002).

Peak metamorphic conditions, constrained by conventional thermobarometry include 550-650 °C and 1.8-2.0 GPa for an eclogite (Feininger, 1980; John et al., 2010), and 550-600 °C and 2.0 GPa for a garnet-chloritoid-kyanite metapelite (Gabriele et al., 2003). In contrast, the P-T conditions of the blueschist are unclear, with some works suggesting that they can be related to the retrograde processes of eclogite at 400-500 °C (Feininger, 1980). Others suggest that they experience metamorphism at similar conditions as the eclogites but at lower pressure (i.e., 550-650 °C and 1.4-1.6 GPa; John et al., 2010).

Lu/Hf garnet ages between 133-126 Ma (John et al., 2010), together with phengite K-Ar and Ar-Ar radiometric ages in phengite between 132-123 Ma (Feininger, 1980; Gabriele, 2002; Riel et al., 2014) argue for a fast burial and exhumation history.

The El Toro Unit is represented by fine- to medium-grained massive, deep-mantle-like metaultramafic rocks, locally serpentinized, such as peridotite and weakly foliated harzburgite that are cut by amphibolite dikes with relicts of eclogite facies metamorphism (Feininger, 1980; Arculus, 1999; Gabriele, 2002). Their origin is attributed to decompression upwelling followed by recrystallization at pressures ranging from 1.0 to 2.5 GPa with subsequent eclogite facies metamorphism with peak conditions constrained at 500-550 °C (Gabriele, 2002).

METHODS

Whole rock geochemistry

Detailed petrographic analyses of 14 samples collected in 33 outcrops were performed to select representative lithotypes for whole-rock geochemistry, avoiding veins and weathered surfaces before crushing in a jaw crusher. In addition, descriptions were carried out in the eclogites, blueschists, garnet amphibolites (retroeclogites), and greenschists (retrograde blueschists) from the Raspas Metamorphic Complex to determine their mineralogical composition, microtextures, mineral paragenesis and where possible, the metamorphic grade. Sample locations and geochemical analysis are presented in Table 1.

Whole rock geochemistry of 14 samples (four eclogites, four blueschists, four garnet amphibolites, and two greenschists) was obtained to constrain the tectonic setting of the protoliths and to compare them with published geochemical information from Raspas Metamorphic Complex (18),

The samples were pulverized (90% < 200 mesh) using a tungsten carbide ring mill at the Instituto de Geociências of the University of São Paulo, Brazil. After this pulverization, the acid digestion of 0.25 g of sample was done. For major elements, samples were analyzed using an inductively coupled plasma emission spectrometer (ICP-ES) and for trace and rare earth elements (REE) using an inductively coupled (ICP-MS) in Activation Laboratories Ltd. (Actlabs), Canada. The detection limit for SiO2, Al2O3, Fe2O3, MgO, CaO, Na2O, K2O, P2O5, and loss on ignition (LOI) was 0.01% for MnO and TiO2 were 0.001%. The detection limit for trace elements varies between 0.005 and 10,000 ppm, depending on the element analyzed. Therefore, it is essential to consider that tungsten carbide could be a potential contaminant (Nb and Co). For this reason, we consider

the experiments by Johnson et al. (1999). The latter suggests that the degree of contamination is of the same magnitude (2%) as the detection limit (one standard deviation of 1.0 ppm). Yamasaki (2018) showed that the main elemental analysis did not show contamination of the samples with preparation in different mills. On the other hand, trace element analyzes were contaminated by W and Co from the tungsten carbide ring mills, yet those trends were easily discernible.

We have compared the results with published constraints with known un-metamorphosed oceanic crust environments, especially oceanic plateau related (1524 analysis), such as Kerguelen (440), Ontong Java (496), and Caribbean (588). The latter includes fragments in Ecuador's western (Pallatanga Unit) and coastal portions (Piñón Unit). The analysis from the oceanic plateaus was selected from the GEOROC database. All data used are presented in the Appendix (table A.1).

Table 1 Major and trace element analysis of metabasites from the Raspas Metamorphic Complex

Rock type	Unit Symbol	GA	GA	GA	EC	EC
Sample		155A	156B	158	160	160A
Latitude		17	17	17	17	17
		0620416	0620409	0630314	0620547	0620547
Longitude		9602592	9602479	9602533	9602467	9602467
SiO2	%	49.25	52.17	49.33	51.95	50.32
Al2O3	%	15.67	14.81	16.14	14.39	14.17
Fe2O3(Total)	%	9.65	10.36	8.57	10.38	13.14
MnO	%	0.19	0.19	0.14	0.18	0.21
MgO	%	7.45	6.48	8.54	7.30	6.77
CaO	%	12.85	11.62	12.37	10.79	10.76
Na2O	%	2.51	1.93	2.61	2.41	2.90
K2O	%	0.18	0.14	0.07	0.12	< 0.01
TiO2	%	0.99	1.07	0.81	1.59	1.86
P2O5	%	0.13	0.13	0.07	0.24	0.16
LOI	%	1.55	1.15	1.55	0.53	< 0.01
Total	%	100.40	100.00	100.20	99.89	100.00
Sc	ppm	42.00	39.00	38.00	38.00	42.00
Be	ppm	< 1	< 1	< 1	1.00	1.00
V	ppm	265.00	302.00	238.00	305.00	392.00
Cr	ppm	370.00	180.00	330.00	50.00	150.00
Co	ppm	62.00	74.00	60.00	64.00	36.00
Ni	ppm	90.00	70.00	100.00	60.00	80.00
Cu	ppm	50.00	80.00	20.00	50.00	60.00
Zn	ppm	80.00	90.00	70.00	90.00	120.00
Ga	ppm	15.00	17.00	15.00	17.00	17.00
Ge	ppm	1.60	1.60	1.30	1.50	1.60
As	ppm	< 5	< 5	< 5	< 5	< 5

Rb	ppm	2.00	3.00	< 1	< 1	< 1
Sr	ppm	136.00	143.00	116.00	122.00	40.00
Y	ppm	26.00	28.40	21.60	31.60	52.10
Zr	ppm	55.00	57.00	37.00	110.00	129.00
Nb	ppm	3.80	3.30	0.90	14.30	2.50
Mo	ppm	< 2	< 2	< 2	< 2	< 2
Ag	ppm	< 0.5	< 0.5	< 0.5	< 0.5	< 0.5
In	ppm	< 0.1	< 0.1	< 0.1	< 0.1	< 0.1
Sn	ppm	< 1	1.00	< 1	1.00	2.00
Sb	ppm	< 0.2	< 0.2	< 0.2	< 0.2	< 0.2
Cs	ppm	< 0.1	< 0.1	< 0.1	< 0.1	< 0.1
Ba	ppm	35.00	58.00	16.00	15.00	190.00
La	ppm	3.60	3.72	1.52	10.80	5.10
Ce	ppm	8.92	8.78	4.25	24.10	14.20
Pr	ppm	1.36	1.43	0.79	3.13	2.65
Nd	ppm	7.08	7.98	4.70	13.50	14.60
Sm	ppm	2.26	2.63	1.77	3.71	4.91
Eu	ppm	0.94	1.06	0.79	1.48	1.82
Gd	ppm	3.11	3.44	2.48	4.33	6.40
Tb	ppm	0.63	0.72	0.52	0.84	1.31
Dy	ppm	4.16	4.87	3.50	5.47	8.80
Ho	ppm	0.87	1.02	0.74	1.15	1.83
Er	ppm	2.65	3.02	2.26	3.47	5.49
Tm	ppm	0.39	0.45	0.33	0.51	0.83
Yb	ppm	2.51	2.93	2.13	3.27	5.35
Lu	ppm	0.39	0.45	0.34	0.50	0.82
Hf	ppm	1.50	1.70	1.20	2.90	3.70
Ta	ppm	1.07	1.45	1.01	2.22	0.12
W	ppm	212.00	356.00	272.00	313.00	4.20
Tl	ppm	< 0.05	< 0.05	< 0.05	< 0.05	< 0.05
Pb	ppm	< 5	< 5	< 5	< 5	< 5
Bi	ppm	< 0.1	< 0.1	< 0.1	< 0.1	< 0.1
Th	ppm	0.28	0.25	< 0.05	1.02	0.19
U	ppm	0.11	0.18	0.03	0.37	0.08

Table 1 cont.

Rock type	Unit Symbol	GS	GS	BS	EC	BS
Sample		162	164	166	172	173
Latitude		17 0621444	17 0624477	17 0624651	17 0619859	17 0619781
Longitude		9602583	9601565	9600668	9602500	9602581
SiO2	%	48.38	47.49	49.35	51.16	48.14
Al2O3	%	16.60	16.80	13.94	13.70	16.77
Fe2O3(Total)	%	6.79	9.83	12.97	12.65	8.72
MnO	%	0.12	0.17	0.22	0.26	0.07
MgO	%	9.84	8.09	8.75	8.02	9.62
CaO	%	13.77	12.08	8.25	9.77	9.92
Na2O	%	1.90	2.05	3.12	2.67	2.10
K2O	%	0.06	0.19	0.28	0.13	0.18
TiO2	%	0.51	1.08	1.57	1.64	0.26
P2O5	%	0.04	0.11	0.14	0.14	0.01
LOI	%	2.41	2.51	1.54	0.79	4.03
Total	%	100.40	100.40	100.10	100.90	99.81
Sc	ppm	43.00	41.00	43.00	44.00	19.00
Be	ppm	< 1	< 1	2.00	1.00	< 1
V	ppm	190.00	287.00	347.00	382.00	80.00
Cr	ppm	510.00	360.00	140.00	190.00	480.00
Co	ppm	41.00	40.00	45.00	80.00	28.00
Ni	ppm	140.00	120.00	80.00	70.00	160.00
Cu	ppm	30.00	60.00	80.00	70.00	30.00
Zn	ppm	50.00	90.00	110.00	130.00	40.00
Ga	ppm	13.00	17.00	17.00	19.00	10.00
Ge	ppm	1.40	1.70	1.50	1.30	0.80
As	ppm	< 5	< 5	< 5	< 5	< 5

Rb	ppm	2.00	3.00	2.00	2.00	3.00
Sr	ppm	125.00	148.00	98.00	87.00	79.00
Y	ppm	14.20	26.10	33.80	38.20	6.60
Zr	ppm	17.00	56.00	92.00	90.00	7.00
Nb	ppm	0.90	2.60	6.00	1.90	< 0.2
Mo	ppm	< 2	< 2	< 2	< 2	< 2
Ag	ppm	< 0.5	< 0.5	< 0.5	< 0.5	< 0.5
In	ppm	< 0.1	< 0.1	< 0.1	< 0.1	< 0.1
Sn	ppm	< 1	< 1	1.00	1.00	< 1
Sb	ppm	< 0.2	< 0.2	< 0.2	< 0.2	< 0.2
Cs	ppm	0.10	0.10	0.10	< 0.1	0.20
Ba	ppm	17.00	21.00	55.00	14.00	62.00
La	ppm	1.28	2.94	5.40	3.25	0.38
Ce	ppm	2.89	7.93	14.00	10.80	1.11
Pr	ppm	0.57	1.29	2.11	1.87	0.21
Nd	ppm	3.48	6.91	10.90	10.90	1.49
Sm	ppm	1.26	2.29	3.42	3.92	0.56
Eu	ppm	0.62	1.03	1.35	1.62	0.38
Gd	ppm	1.77	3.23	4.29	5.58	0.80
Tb	ppm	0.37	0.66	0.86	1.07	0.17
Dy	ppm	2.51	4.36	5.67	6.80	1.12
Ho	ppm	0.52	0.91	1.19	1.38	0.22
Er	ppm	1.53	2.74	3.58	4.11	0.64
Tm	ppm	0.22	0.40	0.53	0.63	0.09
Yb	ppm	1.35	2.63	3.39	4.17	0.57
Lu	ppm	0.20	0.41	0.50	0.65	0.09
Hf	ppm	0.60	1.60	2.60	2.70	0.30
Ta	ppm	0.62	0.37	0.36	1.18	< 0.01
W	ppm	23.60	22.00	0.90	301.00	2.70
Tl	ppm	< 0.05	< 0.05	< 0.05	< 0.05	< 0.05
Pb	ppm	< 5	< 5	< 5	< 5	< 5
Bi	ppm	< 0.1	< 0.1	< 0.1	< 0.1	< 0.1
Th	ppm	0.06	0.16	0.34	0.12	< 0.05
U	ppm	0.09	0.09	0.36	0.08	0.02

Table 1 cont.

Rock type	Unit Symbol	BS	BS	GA	EC
Sample		174	174A	175J	MC22
Latitude		17 0619825	17 0619825	17 0618670	17 0621091
Longitude		9602780	9602780	9601880	9602177
SiO2	%	47.36	44.33	45.63	45.12
Al2O3	%	17.40	16.95	17.78	17.32
Fe2O3(Total)	%	10.24	10.53	7.55	10.72
MnO	%	0.18	0.21	0.12	0.21
MgO	%	5.61	6.62	10.00	6.72
CaO	%	10.35	10.60	15.12	13.38
Na2O	%	2.64	2.61	1.23	1.69
K2O	%	0.67	1.09	< 0.01	0.18
TiO2	%	2.25	2.28	0.61	2.44
P2O5	%	0.51	0.37	0.04	0.24
LOI	%	3.02	4.53	2.36	1.83
Total	%	100.20	100.10	100.40	99.85
Sc	ppm	32.00	31.00	42.00	40.00
Be	ppm	2.00	2.00	< 1	1.00
V	ppm	257.00	262.00	219.00	352.00
Cr	ppm	270.00	250.00	620.00	100.00
Co	ppm	45.00	41.00	42.00	56.00
Ni	ppm	120.00	150.00	120.00	80.00
Cu	ppm	80.00	50.00	90.00	640.00
Zn	ppm	120.00	140.00	50.00	130.00
Ga	ppm	23.00	23.00	15.00	25.00
Ge	ppm	1.70	1.70	1.40	1.80
As	ppm	< 5	< 5	< 5	< 5
Rb	ppm	9.00	18.00	< 1	3.00

Sr	ppm	435.00	365.00	169.00	268.00
Y	ppm	36.30	37.10	13.60	40.00
Zr	ppm	211.00	212.00	21.00	207.00
Nb	ppm	23.00	25.90	0.80	19.90
Mo	ppm	< 2	< 2	< 2	3.00
Ag	ppm	< 0.5	< 0.5	< 0.5	0.70
In	ppm	< 0.1	< 0.1	< 0.1	1.40
Sn	ppm	2.00	2.00	< 1	548.00
Sb	ppm	< 0.2	< 0.2	< 0.2	1.30
Cs	ppm	0.40	0.70	< 0.1	0.20
Ba	ppm	534.00	961.00	11.00	32.00
La	ppm	23.20	19.90	0.67	19.70
Ce	ppm	48.50	45.10	2.35	44.30
Pr	ppm	6.33	5.78	0.43	5.64
Nd	ppm	27.10	25.20	2.83	25.00
Sm	ppm	6.40	5.89	1.16	6.09
Eu	ppm	2.36	2.27	0.66	2.20
Gd	ppm	6.63	6.11	1.67	6.56
Tb	ppm	1.16	1.10	0.35	1.19
Dy	ppm	6.96	6.59	2.38	7.27
Ho	ppm	1.34	1.27	0.48	1.37
Er	ppm	3.77	3.55	1.37	3.93
Tm	ppm	0.54	0.52	0.20	0.58
Yb	ppm	3.38	3.25	1.23	3.78
Lu	ppm	0.51	0.48	0.19	0.58
Hf	ppm	4.80	4.90	0.70	5.10
Ta	ppm	2.21	1.89	< 0.01	2.38
W	ppm	122.00	1.40	1.20	195.00
Tl	ppm	< 0.05	0.05	< 0.05	< 0.05
Pb	ppm	< 5	< 5	< 5	7.00
Bi	ppm	< 0.1	< 0.1	< 0.1	0.50
Th	ppm	1.80	1.78	< 0.05	1.75
U	ppm	0.47	0.49	0.04	0.80

$^{40}Ar/^{39}Ar$ ages

Phengite from eclogite and a retrograded eclogite was concentrated and analyzed by the $^{40}Ar/^{39}Ar$ method. Mineral concentrates were prepared by manual separation of grains present in the ~1 mm fraction. Two or three grains from each sample were analyzed, although, for some samples, only one grain was analyzed.

$^{40}Ar/^{39}Ar$ analyses were performed at the Argon Geochronology Laboratory of the University of Michigan using a continuous laser for step-heating, and a VG 1200S noble gas mass spectrometer equipped with a Daly detector operated in analog mode using the methods outlined in Streepey et al. (2000) and Keane et al. (2006). Analyzed samples were packed within pure Al foil packs and irradiated for 10.83 hrs at 5C at the McMaster Nuclear reactor. Quoted ages are calculated relative to an age of 520.4 Ma for hornblende standard MMHb-1. After irradiation, two or three crystals were chosen from each sample for extraction and purification of argon by the step-heating method. The resulting ages are presented in the Table 2.

Table 2 $^{40}Ar/^{39}Ar$ results and mineralogy of some samples from Raspas Metamorphic Complex.

Sample	Plateau Age (Ma)	Analyzed mica	Sample mineralogy
156B	129.1 ±0.5	phengite	garnet + omphacite + zoisite + phengite + quartz
174	124.2 ±1	phengite	garnet + omphacite + zoisite + phengite + amphibole + quartz

X-ray maps and mineral analysis

The X-ray compositional maps and spot analysis were obtained through an Electron Microprobe Analyzer (EMPA) model JEOL JXA-8230 at the Department of Petrology and Metallogeny of the Universidade Estadual Paulista (UNESP), Brazil.

The compositional maps were obtained for the elements: Si, Al, Mn, Mg, Ca, Na, Ti, Zr, K, and Fe by wavelength-dispersive spectroscopy (WDS), whereas S, P, Ba, and Cl by Energy-Dispersive Spectroscopy (EDS). The operation conditions were 15 keV, ~ 300 nA, a focused beam, a step (pixel) size of 6 μm, and a counting time of 30 ms/pixel.

Compositional spots on omphacite, amphibole, epidote, and profiles in garnet were analyzed. These analyses were performed with a beam current of ~20nA, accelerating voltage of 15 kV, and counting time variables depending on elements. Microprobe analytical errors range ± 0.01-0.21 wt% (1σ) with detection limits varying ± 0.01-0.11 wt%. The standards used for calibrations were "albite" for Na, "anorthite" for Al, "apatite" for P, "barite" for Ba, "diopside" for Mg, "ilmenite" for Fe and Ti, "orthoclase" for K, "pyrite" for S, "rhodonite" for Mn, "sodalite" for Cl, "wollastonite" for Ca and Si, and "zircon" for Zr. All mineral compositions were recalculated using the program CALCMIN (Brandelik, 2009). Representative mineral analysis is presented in the Table 3 and 4. The complete database is available as supporting information (Table S1)

The X-ray maps were processed using the XMapTools version 3.4.1 (Lanari et al., 2014; Lanari et al., 2019; Lanari, 2020). The spot analysis was used to convert the counting maps into oxide maps through the "Standardization" function of this software. As a result, quartz was standardized considering a homogeneous phase (100 % of SiO_2) with only a minor (0.01 wt.%) of Al_2O_3 (Lanari, 2020).

The Zr-in rutile Thermometry operation conditions were set at 20 kV and 80 nA and performed for the elements Si, Al, Cr, V, Sb, Sn, W, Ta, Hf, Fe, Ti, Nb, and Zr following Luvizotto et al. (2009). Moreover, the analysis with values of Si above 300 ppm or anomalous Zr contents was discarded following Zack et al. (2004). The data is presented in Table 5.

Table 3 Representative mineral analysis of garnet, omphacite and epidote from the Raspas Metamorphic Complex. The remaining analysis are available as supplementary material (Table A.2).

Mineral	Grt-2	Grt-2	Grt-2	Grt-2	Grt-2	Grt-2	Grt-2	Grt-2	Grt-2	Omp	Omp	Ep	Ep
Spot	184	185	186	194	195	196	204	205	206	1	8	7	10
Location	Rim	Rim	Rim	Mantle	Mantle	Mantle	Core	Core	Core				
SiO_2	39.11	38.44	38.88	37.93	38.47	38.21	38.57	38.62	38.45	54.97	55.56	38.35	39.06
TiO_2	0.03	0.07	0.04	0.06	0.07	0.09	0.14	0.09	0.15	0.69	0.10	0.01	0.13
$Al2O_3$	21.69	21.54	21.58	21.09	21.52	21.05	21.33	21.36	21.35	10.13	10.11	21.40	27.84
Cr_2O_3	---	---	---	---	---	---	---	---	---	0.01	0.01	0.01	0.01
Fe_2O_3	0.19	0.40	0.51	0.69	0.44	0.82	0.61	0.76	0.62	0.00	0.08	27.76	7.22
FeO	25.38	24.78	24.33	24.00	23.48	23.62	22.94	22.95	22.57	5.74	5.10	---	---
Mn_2O_3	---	---	---	---	---	---	---	---	---	---	---	0.67	0.03
MnO	0.45	0.42	0.44	1.34	1.29	1.57	0.79	0.80	1.14	0.03	0.02	---	---
MgO	5.80	5.39	5.35	2.21	3.07	2.71	4.70	4.69	4.52	8.00	8.27	5.78	0.16
CaO	7.74	8.79	9.38	12.66	12.31	12.11	10.72	10.88	11.01	13.08	13.79	7.83	22.93
Na_2O	0.02	0.01	0.04	0.01	0.03	0.03	0.04	0.06	0.05	6.34	6.24	0.05	0.06
K_2O	---	---	---	---	---	---	---	---	---	0.05	0.01	---	---
Total	100.43	99.87	100.60	100.01	100.67	100.22	99.86	100.23	99.90	99.04	99.31	101.86	97.45
Si	6.08	5.98	6.01	5.98	5.99	6.01	6.02	6.00	6.00	1.99	2.00	2.93	3.04
Ti	0.00	0.01	0.00	0.01	0.01	0.01	0.02	0.01	0.02	0.02	0.00	0.00	0.01
Al	3.98	3.95	3.93	3.92	3.95	3.90	3.93	3.91	3.92	0.42	0.43	1.93	2.55
Cr	---	---	---	---	---	---	---	---	---	0.00	0.00	0.00	0.00
Fe^{3+}	0.02	0.05	0.06	0.08	0.05	0.10	0.07	0.09	0.07	0.00	0.00	1.60	0.42
Fe^{2+}	3.30	3.23	3.15	3.16	3.06	3.11	3.00	2.98	2.94	0.17	0.15	---	---
Mg	1.34	1.25	1.23	0.52	0.71	0.63	1.09	1.09	1.05	0.43	0.44	0.66	0.02
Ca	1.29	1.47	1.55	2.14	2.05	2.04	1.79	1.81	1.84	0.51	0.53	0.64	1.91
Mn^{3+}	---	---	---	---	---	---	---	---	---	---	---	0.04	0.00
Mn	0.06	0.06	0.06	0.18	0.17	0.21	0.10	0.10	0.15	0.00	0.00	---	---
Na	0.01	0.00	0.01	0.00	0.01	0.01	0.01	0.02	0.02	0.45	0.44	0.01	0.01
K	---	---	---	---	---	---	---	---	---	0.00	0.00	---	---

Diopside	---	---	---	---	---	---	---	---	---	0.36	0.40	---	---
Hedenbergite	---	---	---	---	---	---	---	---	---	0.15	0.14	---	---
Jadeite	---	---	---	---	---	---	---	---	---	0.43	0.43	---	---
grossular	0.21	0.24	0.26	0.36	0.34	0.34	0.30	0.30	0.31	---	---	---	---
pyrope	0.22	0.21	0.21	0.09	0.12	0.11	0.18	0.18	0.18	---	---	---	---
almandine	0.55	0.54	0.52	0.53	0.51	0.52	0.50	0.50	0.49	---	---	---	---
spessartine	0.01	0.01	0.01	0.03	0.03	0.03	0.02	0.02	0.03	---	---	---	---
xAl	0.99	0.99	0.98	0.98	0.99	0.98	0.98	0.98	0.98	---	---	---	---

Table 4 Amphibole analysis from the Raspas Metamorphic Complex.

SiO2	45.93	46.21	46.43	46.48	46.47	46.96	46.62	47.64
TiO2	0.49	0.49	0.49	0.48	0.45	0.45	0.48	0.39
Al2O3	14.73	14.68	14.29	14.34	14.36	14.02	14.25	13.27
Cr2O3	0.03	0.06	0.04	0.01	0.01	0.01	0.03	0.02
MnO	0.02	0.03	0.03	0.03	0.03	0.00	0.00	0.02
FeO	10.79	9.81	10.24	10.36	9.99	9.96	10.20	9.97
MgO	11.59	12.06	11.96	11.84	12.11	12.04	12.15	12.42
CaO	8.24	8.16	8.17	8.08	8.25	8.17	8.16	7.94
Na2O	4.32	4.21	4.20	4.13	4.15	4.09	4.14	4.14
K2O	0.38	0.38	0.40	0.37	0.38	0.37	0.37	0.35
Total	96.52	96.09	96.25	96.12	96.20	96.07	96.40	96.16
Si	6.66	6.69	6.73	6.74	6.73	6.80	6.73	6.88
Al	1.34	1.31	1.27	1.26	1.27	1.20	1.27	1.12
Ti								
Fe3+								
SUM_T	8.00	8.00	8.00	8.00	8.00	8.00	8.00	8.00
Ti	0.05	0.05	0.05	0.05	0.05	0.05	0.05	0.04
Al	1.18	1.20	1.17	1.19	1.18	1.19	1.16	1.14

Cr	0.00	0.01	0.01	0.00	0.00	0.00	0.00	0.00
Mn3+								
Fe3+	0.10	0.10	0.10	0.11	0.10	0.08	0.11	0.10
Mn2+								
Fe2+	1.16	1.04	1.10	1.09	1.07	1.09	1.05	1.04
Mg	2.51	2.60	2.58	2.56	2.61	2.60	2.62	2.67
SUM_C	5.00	5.00	5.00	5.00	5.00	5.00	5.00	5.00
Mn2+	0.00	0.00	0.00	0.00	0.00			0.00
Fe2+	0.05	0.05	0.05	0.06	0.05	0.04	0.07	0.06
Mg	0	0	0	0				
Ca	1.28	1.27	1.27	1.26	1.28	1.27	1.26	1.23
Na	0.67	0.68	0.68	0.68	0.67	0.69	0.67	0.71
SUM_B	2.00	2.00	2.00	2.00	2.00	2.00	2.00	2.00
Ca								
Na	0.55	0.50	0.50	0.48	0.50	0.46	0.49	0.45
K	0.07	0.07	0.07	0.07	0.07	0.07	0.07	0.06
SUM_A	0.62	0.57	0.58	0.55	0.57	0.53	0.56	0.51
SUM_CAT	15.62	15.57	15.58	15.55	15.57	15.52	15.56	15.51

Table 5 ppm Rutile analysis and temperature calculations using the Zr-in Rutile calibration (Zack et al., 2004).

Si	160.33	657.69	2618.60	90.22	BD
Al	78.33	62.98	528.19	59.81	33.87
Sn	BD	BD	BD	BD	BD
Cr	485.10	628.78	640.41	428.31	513.15
Sb	BD	BD	BD	BD	BD
Ta	BD	BD	BD	BD	BD
Fe	5506.46	5036.19	7464.51	5026.86	4656.09
W	BD	BD	BD	BD	BD
Hf	BD	BD	BD	BD	BD
Zr	179.89	116.97	3953.20	149.54	183.59
Nb	62.21	112.55	BD	110.45	94.37
Ti	593008.31	594249.30	585760.24	596941.70	596111.98
T (16.4 Gpa)	636.62	605.07	952.68	622.80	638.17
Std dev. σ	21.18	85.26	172.76	88.91	92.14
T (14.3 Gpa)	627.98	596.73	941.03	614.29	629.51
Std dev. σ	20.98	84.45	171.12	88.07	91.27

Table 5 cont.

Si	82.74	102.37	BD	BD	75.26
Al	30.70	25.93	30.17	BD	29.64
Sn	BD	BD	BD	BD	BD
Cr	485.78	541.89	520.68	650.67	545.99
Sb	BD	BD	BD	BD	BD
Ta	BD	BD	BD	BD	BD
Fe	4370.04	4683.29	8800.70	3291.13	3785.50
W	BD	BD	BD	BD	BD
Hf	BD	BD	BD	BD	BD
Zr	135.47	145.10	68.85	163.61	122.89
Nb	71.30	81.09	BD	108.35	101.36
Ti	595113.79	595281.06	592750.52	595321.82	594096.42
T (16.4 Gpa)	615.59	620.59	569.12	629.47	608.58
Std dev. σ	16.04	27.89	14.64	14.06	21.78
T (14.3 Gpa)	607.15	612.10	561.12	620.90	600.21
Std dev. σ	15.88	27.63	14.50	13.92	21.57

Table 5 cont.

Si	BD	BD	BD	BD	95.36
Al	BD	47.10	42.87	50.81	51.34
Sn	BD	BD	BD	BD	BD

Cr	450.20	446.78	357.15	368.10	318.15
Sb	BD	BD	BD	BD	BD
Ta	BD	BD	BD	BD	BD
Fe	3291.13	3846.91	4975.56	4296.19	5917.66
W	BD	BD	BD	BD	BD
Hf	BD	BD	BD	BD	BD
Zr	131.03	139.92	158.42	155.46	160.65
Nb	83.88	84.58	66.41	90.18	71.30
Ti	596479.48	596647.34	595013.08	595654.55	595340.41
T (16.4 Gpa)	613.18	617.93	627.07	625.67	628.11
Std dev. σ	86.92	24.62	89.80	89.51	90.02
T (14.3 Gpa)	604.76	609.47	618.52	617.13	619.55
Std dev. σ	86.09	24.38	88.95	88.66	89.16

Table 5 cont.

Si	BD	107.04	BD	475.85	
Al	34.93	73.57	33.34	46.57	
Sn	BD	BD	BD	BD	
Cr	724.57	820.36	430.36	503.57	
Sb	BD	BD	BD	BD	
Ta	BD	BD	BD	BD	
Fe	3864.01	5169.89	BD	3350.21	
W	BD	BD	BD	BD	
Hf	BD	BD	BD	BD	
Zr	166.57	156.94	130.29	137.70	
Nb	89.48	58.02	76.20	83.88	
Ti	596126.37	593535.28	596520.24	596860.17	
					Average
T (16.4 Gpa)	630.81	626.37	612.77	616.77	619.00
Std dev. σ	18.99	18.08	22.87	20.51	15.00
T (14.3 Gpa)	622.23	617.83	604.36	608.32	611.00
Std dev. σ	18.80	17.91	22.66	20.31	15.00

RESULTS

Sample description

Eclogites and, to a lesser extent, blueschists from the Raspas Unit are mainly concentrated in outcrops along the Raspas River. Large outcrops and boulders of fine- to very coarse-grained dark green eclogites are common. The eclogites comprise garnet porphyroblasts (idioblastic to rounded), pyroxene, quartz, amphibole, and white mica. Very thick amphibole and pyroxene (up to 5 cm in length) also occur locally in pegmatitic-looking lenses or veins. Garnet porphyroblasts are up to 2 cm in diameter, commonly with rims and coronas of chlorite and white mica. Eclogite bodies sometimes have thicknesses ranging from thousands to a few meters, usually intercalated with metapelites. Several fault/shear zones cut through the eclogites, sometimes associated with quartz-feldspathic rock lenses with intercalated eclogite boudins. In the most sheared areas, it is common the presence of several garnetite with pyroxene beds. Retrometamorphic transformation of eclogites to eclogites with amphibole/chlorite has also been found in decametric beds.

In the westernmost part of the Raspas River, the replacement of eclogites by greenschists, usually coarse-grained, with actinolite, chlorite, epidote, and plagioclase are more prominent. Fine-grained eclogites showing the strong orientation of their assemblage, coupled with enrichment in white micas and fine blue amphibole, were observed in contact with greenschist, suggesting some structural relation between both lithologies.

Large blocks of breccias associated with more recent faults are also common. In some outcrops, especially on the western portion, remnants of blueschist intercalated with mylonitized greenschists are also exposed. This blueschist comprises blue amphibole and white mica with garnet

porphyroblasts. Partially serpentinized ultramafic rocks highly deformed were also observed. Small bodies of metagabbros, gneisses, migmatites, and granites, probably from the Tahuim group, were also found in the southern portion.

Eclogites (and retrograded eclogites)

These rocks are mainly composed of omphacite (40 to 58%), garnet (35 to 52%), zoisite (6 to 10%), quartz (4 to 9%), and white mica (accessory to 8%). However, two samples exhibit anomalous content of ~18% of this mineral, amphibole (up to 5%), rutile (up to 5%), and accessory minerals are found titanite, chlorite, epidote-clinozoisite, and apatite. The samples are characterized by elongated crystals of omphacite in the matrix, defining the main foliation (S_{n+2}) that wraps around the porphyroblasts, forming pressure shadows of quartz locally. In some samples, a granoblastic texture was seen.

The garnet is slightly pink, with crystals generally subidioblastic to xenoblastic, although some grains have idioblastic rims. The zoning of the grains is not well defined, but, when present, it is marked by inclusions in the cores and their absence in the mantles. The inclusions are mainly quartz, epidote-clinozoisite, amphibole, omphacite, and rutile, which sometimes are found oriented and even slightly folded, defining a previous foliation (S_{n+1}). Zoning is especially visible in sample 171, with two different stages of garnet crystallization. First, a fine-grain garnet was found without inclusions and usually accumulated in small bands or scattered on the sample (Figure 2a). The other type of garnet is subidioblastic, with a few non-oriented quartz inclusions and a reaction rim, in which plagioclase, amphibole, and eventually quartz and titanite are concentrated. This reaction rim is overgrown by an inclusion-free garnet ring defining atoll texture (Figure 2b). The rims of

atoll garnets are idioblastic but, in most cases, are corroded. In some samples (e.g., 155A), replacement borders with chlorite and eventually amphibole and plagioclase are present.

Omphacite is present as elongated, colorless to light green, and subidioblastic to idioblastic grains that, together with the epidote-group minerals, define the main foliation (S_{n+2}) of the analyzed samples. Zoisite presents grains ranging from 0.2 to 2.9 mm, primarily subidioblastic and oriented according to S_{n+2}. The zoning is not very clear, but nuclei with birefringence of a higher order than the edges are present. Some of the grains have inclusions of quartz and opaque minerals, and the arrangement of these minerals defines a nematoblastic texture.

Quartz is xenoblastic and is the main forming mineral of pressure shadows in the garnet, characterized by a strong undulating extinction. White mica consists of grains that are mainly subidioblastic and may locally define a lepidoblastic texture. Finally, rutile and titanite are found as small crystals up to 0.1 and 0.4 mm, respectively, being in both cases subidioblastic and, eventually, xenoblastic.

Chlorite is seen as small grains with a slight pleochroism that varies in shades of very light green. They are xenoblastic grains found mainly on the rims and fractures of the garnet but also occur as replacement rims around amphibole.

Amphiboles are mostly subidioblastic to xenoblastic and exhibit a pleochroic formula that may correspond to a barroisite. Some crystals have quartz, opaque minerals, and titanite inclusions. This mineral defines a clear nematoblastic texture along the main foliation of the rock. Epidote-clinozoisite occurs, in a few samples, as xenoblastic grains, folded and with well-marked undulating extinction. Apatite appears as small and rounded grains disseminated on the sample.

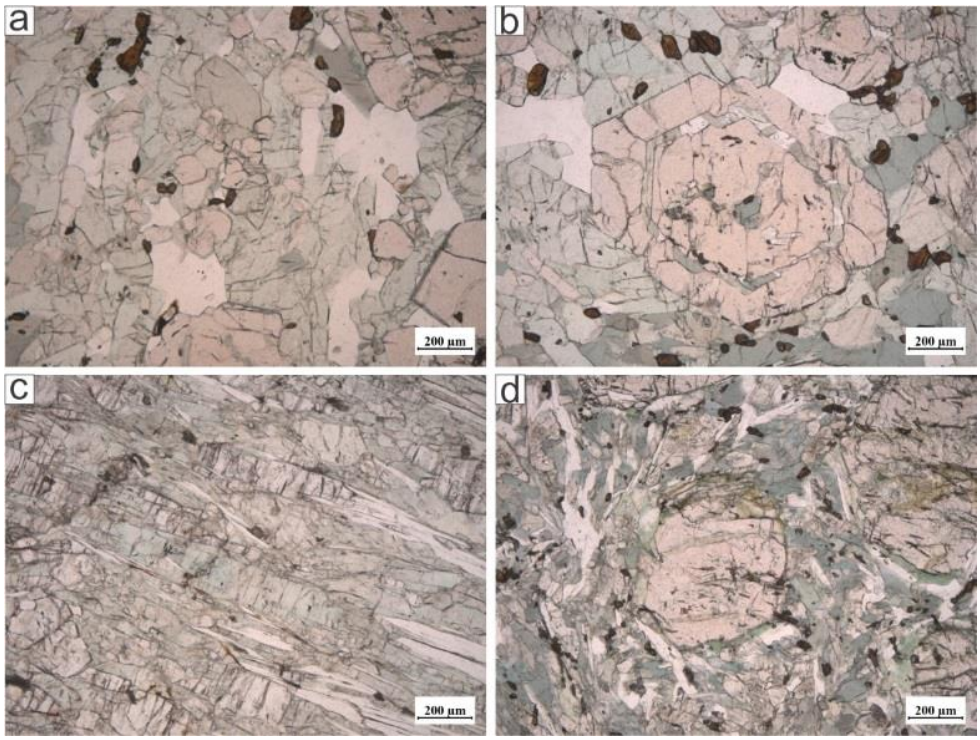

Figure 2(a) fine-grained garnets in the eclogites are usually found scattered through the matrix. (b) garnet porphyroblasts with a typical atoll texture with inclusions of amphibole, omphacite, and quartz with minor epidote and rutile in the core. (c) well-developed foliation in a blueschist from the Raspas Metamorphic Complex. The matrix is dominated by elongated glaucophane exhibiting slightly green cores associated with cloudy zoisite and paragonite. (d) garnet blueschist shows large garnet porphyroblasts highly fractured with incipient retrograde influence due to chlorite formation.

Blueschists and greenschists

Blueschist samples are made up of garnet (30 to 35%), glaucophane and green-amphibole (12 to 18%), white mica (10 to 15%), quartz (8 to 16%), epidote-clinozoisite (4 to 11%), rutile (accessory to 6%), opaque minerals (up to 2%).

Garnet is observed mainly as subidioblastic grains, but some are xenoblastic, and, in minor proportion, idioblastic rims are also observed, where the latter corresponds to an S_3 stage. Epidote, clinozoisite, ilmenite, rutile, and titanite were found as inclusion. Like eclogites, the inclusions are concentrated in the core of the grains. Many garnet grains are filled with fractures filled with quartz and glaucophane (Figure 2d).

Glaucophane occurs on the matrix and as elongated subidioblastic to xenoblastic crystals oriented, defining the main S_{n+2} foliation. It presents pleochroism that varies in colorless- lavender-blue to blue tones with some more greenish portions, which suggests the presence of another amphibole different from glaucophane, perhaps barroisite (Figure 2c).

Epidote-clinozoisite is present in the matrix. The crystals are idioblastic to subidioblastic and define nematoblastic texture along the S_{n+2} and amphiboles. White mica is found as subidioblastic and idioblastic crystals. They are observed on the rims of some garnets, also as part of the S_{n+3}. Quartz is presented as a xenoblastic mineral accompanying S_{n+2} and as part of some pressure shadows in garnet. Small grains are also observed as inclusions in garnet. Rutile is found as subidioblastic grains scattered in the sample or included in garnet. In some cases, it is possible to observe that the crystals are oriented and folded within the garnets, defining an S_{n+1}. In some cases, they are associated with opaque acicular shapes, possibly ilmenite, that occur in various forms and is scattered throughout the samples.

Retrogression of a blueschist facies assemblage is observed at different degrees. This process is mainly associated with transforming glaucophane to tremolite in the matrix and forming albite, epidote, and chlorite aggregates after paragonite and garnet. At the end of the spectrum, the rock is dominated by a well-developed foliation of slender tremolite and epidote prisms associated with albite.

Whole rock geochemistry

The metamorphic lithologies from the Raspas Unit have LOI values for eclogites of 0.01-1.83 wt. %, greenschists of 2.41-2.51 wt. %, garnet amphibolites of 1.15-2.36 wt. %, and blueschists of 3.02-4.56 wt. %; and basaltic composition with SiO_2 contents varying between 44.08 - 52.17 wt.%,

TiO_2 ranging from 0.46 - 2.45 wt.%, Al_2O_3 from 13.49 - 17.78 wt.%, and CaO from 7.03 - 15.12 wt.%. The MgO contents show a larger variation from 4.12-10.36 wt.% with no clear distinction between lithologic groups.

A positive correlation is observed between La, Nb, Hf, Th, and Y when compared with Zr, whereas the Ta pattern is scattered. In some eclogite samples, La, Nb, and Th plot below the primary trend near parallel to the Zr axis, whereas five blueschist samples and one eclogite sample are grouped following an oblique trend as observed when Hf and Y are compared with Zr (Figure 3a-f).

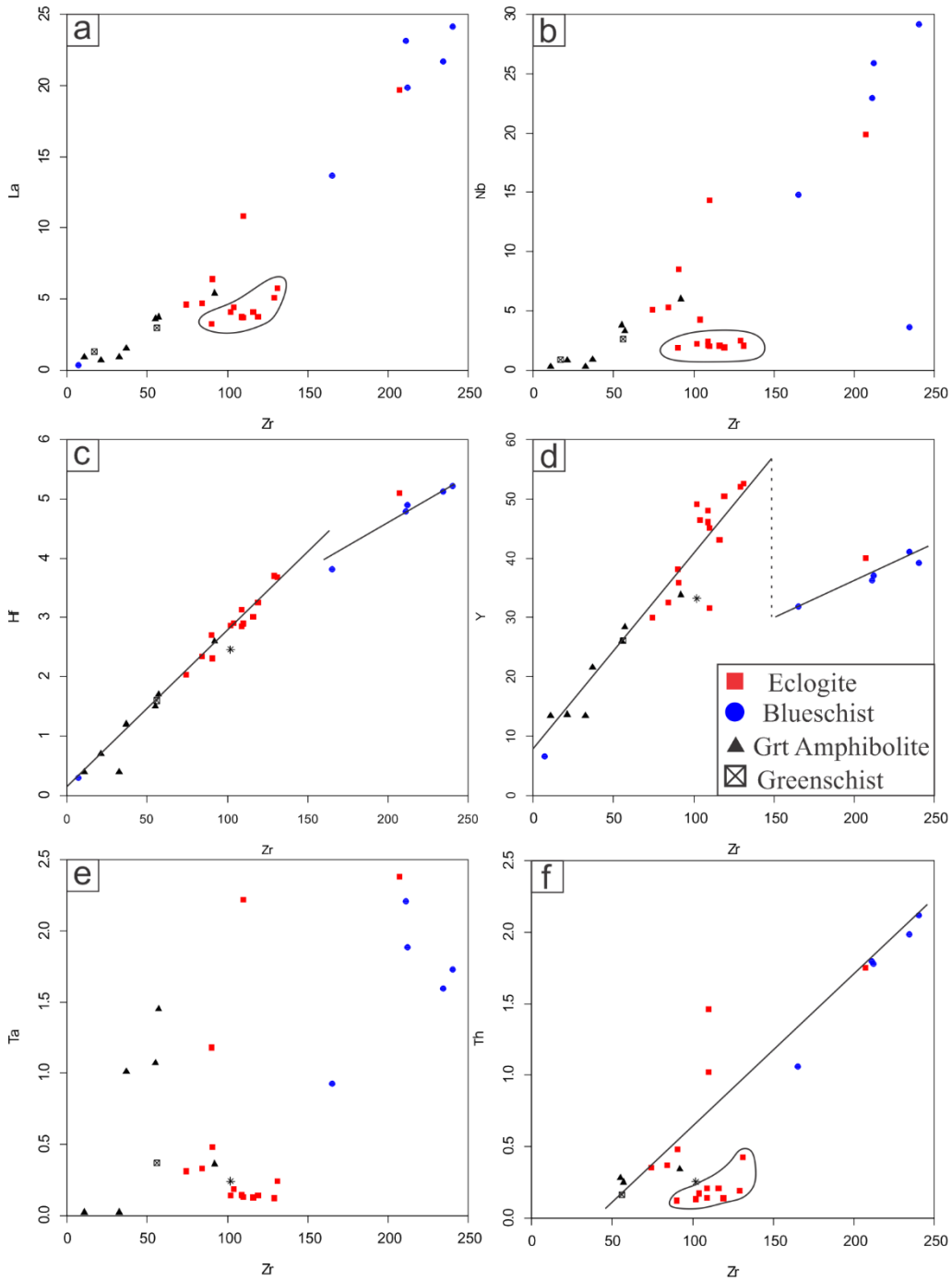

Figure 3 Binary diagrams show the geochemical characteristics of some trace elements when compared with Zr (a-f). Notice that, for the most part, the samples follow a general trend. However, some group of samples does not have the same behavior (circled samples in the image). Some are grouped below the main trend (a, b, f), whereas others follow a secondary trend (c, d). Only in one diagram, the samples are scattered (c).

Primitive mantle normalized plots (McDonough and Sun, 1995; Figure 4a) for eclogite samples display a flat heavy-(H)REE pattern. Light- (L)REE shows variable degrees of enrichment or depletion (La/Yb_{pmn}= 0.62 – 3.79; subscript pmn refers to values normalized to the primitive mantle

of McDonough and Sun, 1995) and a subtle negative to positive Eu anomaly (Eu/Eu* = 0.87 – 1.12). Negative Sr, Th, and Pb anomalies in the three samples are remarkable, whereas some samples display positive U, Pb, and Ta anomalies. They are characterized by broad Zr/Nb ratios (Figure 5a) that range from 7.69 to 64.22. Moreover, the Sm/Yb and La/Yb ratios for eclogites (Figure 5c) are 0.94-1.06 and 0.76-1.80, respectively, although the two samples exhibit higher values (1.13-1.61 and 3.3-5.2, respectively). Th/Y ratios show a significant variation where the majority of eclogite samples have values similar to N-MORB (9 samples with ratios that ranges between 0.003 to 0.005); four samples have intermediate values between N-MORB and primitive mantle (0.008-0.013), and three samples with values above those of primitive mantle (0.032-0.044; Figure 5d). Similar to Th/Y, the Sm/Th ratios exhibit 3 different groups; nine samples with values similar to higher than N-MORB (19.56-39.01), four samples with values between N-MORB and primitive mantle (7.15-8.89), and three samples with values of Sm/Th lower than primitive mantle (2.90-3.64; Figure 5d).

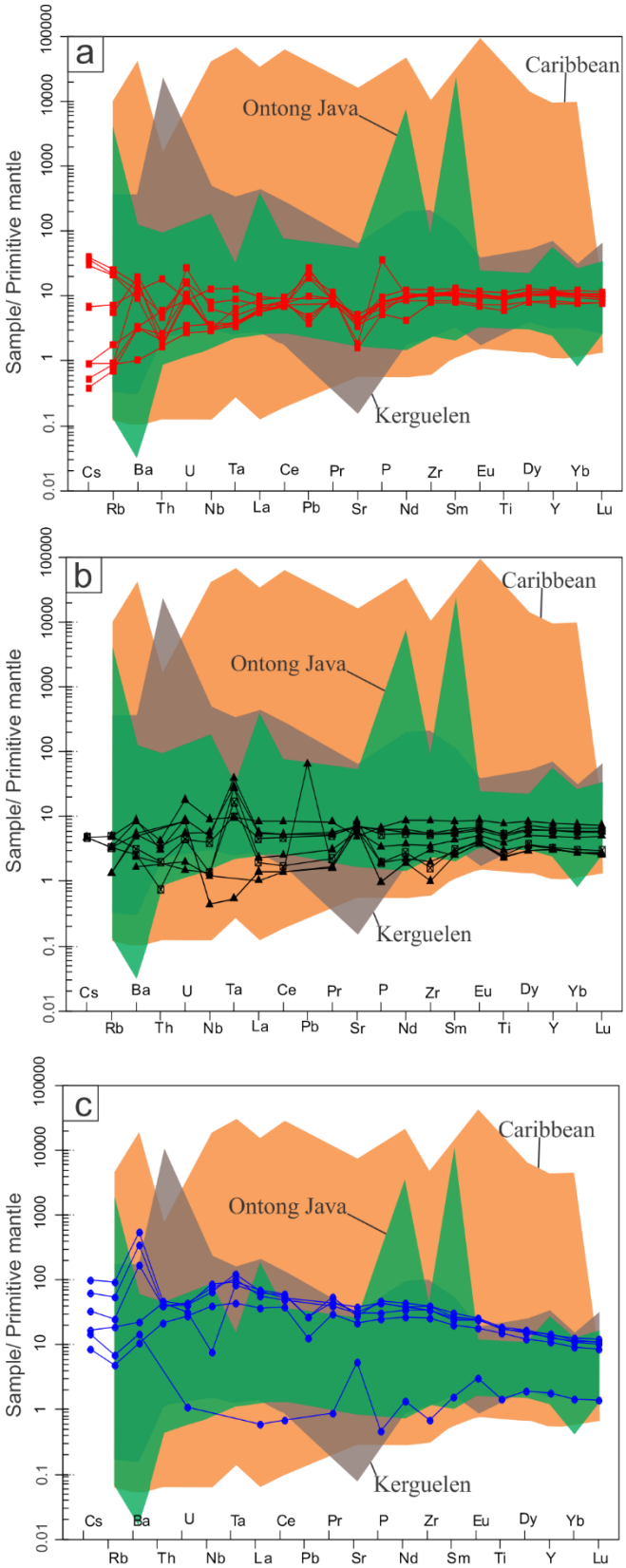

Figure 4 Primitive mantle-normalized multi-element plot (McDonough and Sun, 1995) for the eclogites (a), garnet amphibolites, greenschists (b), and blueschists (c) from the Raspas Complex. The field for representative samples from

the Caribbean, Ontong Java, and Kerguelen Plateaus are plotted in each diagram. The data from the plateaus are from the GEOROC database and are available in the appendix Table A.1.

The greenschists and garnet amphibolites have similar trace element patterns to eclogites with a near flat pattern with negative and positive anomalies of Th, and U, respectively. However, these samples show lower degrees of REE enrichment (i.e., <10 times primitive mantle values against ~10 times of the eclogites) and contrasting Ta and Sr positive anomalies when compared with eclogite samples (Figure 4b). The Zr/Nb ratio exhibits significant variation, but their values are relatively higher than eclogite samples (14.47 – 112.66; Figure 5a). Sm/Yb and La/Yb ratios are similar to eclogites, ranging from 0.83 to 1.01 and 0.13- to 0.54-1.59, respectively (Figure 5c).

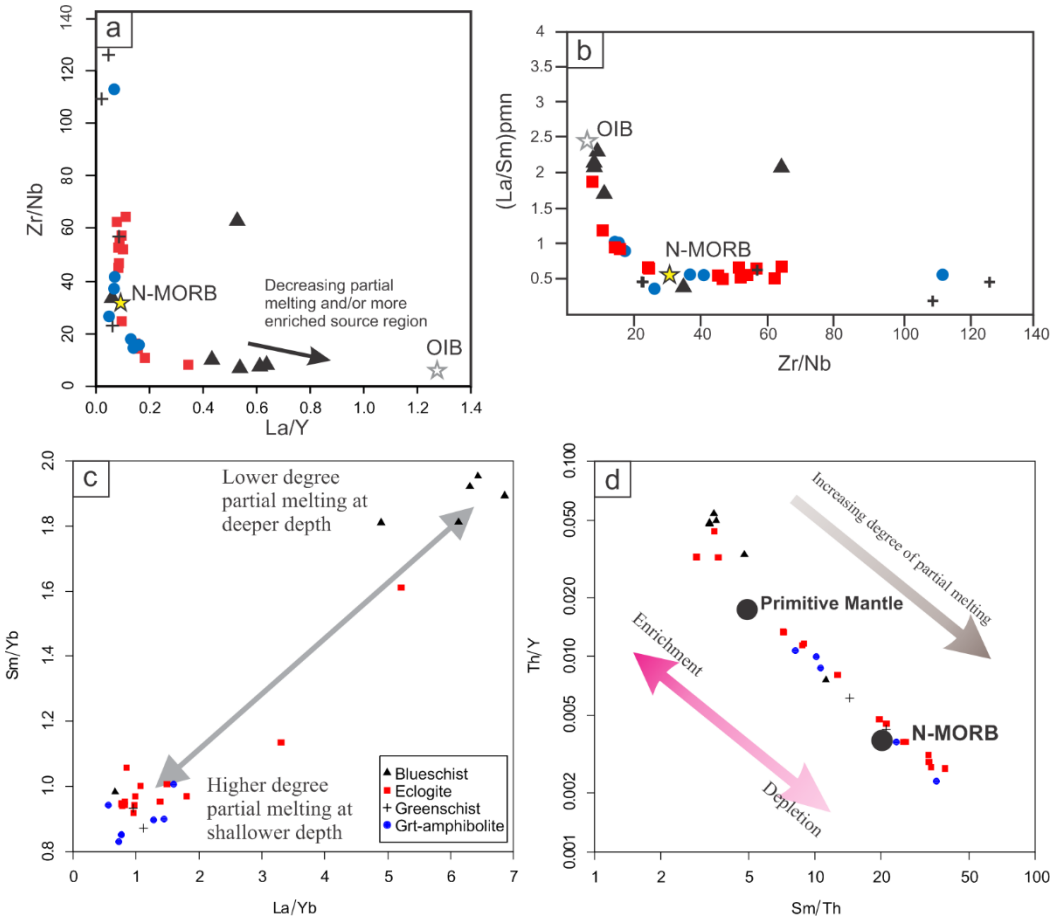

Figure 5 (a) trace element ratio diagram from Raspas metabasites (Hastie et al., 2008). (b) $(La/Sm)_{pmn}$ versus Zr/Nb ratios (after Xia and Li, 2021). $(La/Sm)_{pmn}$ refers to values normalized to primitive mantle from Sun and McDonough (1989). (c) Sm/Yb vs. La/Yb and (d) Th/Y vs. Sm/Th, both after Chen et al. (2021) showed the geochemical characteristics of the mantle source for the Raspas metabasites. In all diagrams, MORB, primitive mantle, and OIB values are from Sun and McDonough (1989).

The blueschist is characterized by a variable degree of LREE enrichments (La/Yb_{pmn} =2.63-4.65), although one sample exhibit LREE depletion (La/Yb_{pmn} = 0.07), similar to eclogite samples. Positive Nb and Ta anomalies are present, resulting in a hump-shaped, E-MORB to- OIB-like pattern in primitive normalized plots (Figure 4c). Remarkable negative Pb and positive Ba and Eu anomalies (Eu/Eu* = 0.97-1.72) are also present. Zr/Nb ratios vary from 8.19 to 64.29. They are also characterized by high Sm/Yb (1.81-1.95), La/Yb (4.89-6.86), Th/Y (0.033-0.054), and low values of Sm/Th (3.31-4.78; Figure 5c, d). One sample does not follow this pattern with values of 0.98, 0.66, 0.008, and 11.20 for these ratios, respectively.

4.3. $^{40}Ar/^{39}Ar$ geochronology

40Ar/39Ar ages on phengite grains from the Raspas samples defined plateau ages at 129.1 ±0.5 and 128.6 ±0.3 Ma (Table 2). These ages are related to the 425 ºC cooling of the muscovite-phengite system (Harrison et al., 2009) and may reflect cooling during the exhumation process of the high-pressure rocks. These results almost overlap with available Lu-Hf garnet in eclogites, blueschists, and metasedimentary rocks (John et al., 2010). These demonstrate the contemporaneous HP garnet growth at ~130 Ma in all three rock types and suggest that this belt experienced very fast exhumation rates. Analogous 40Ar/39Ar ages have also been found farther north in blueschists from the Barragán area in Colombian Andes (Bustamante et al., 2012).

X-ray maps and mineral composition

Garnet

The X-ray maps unravel a complex compositional variation that displays four different zones. The core (zone I) is only preserved at the core of some grains formed by a few spaced regions with evidence of resorption processes. This zone I (Figure 6b-f) is characterized by high grossular and almandine contents with little compositional variations ($Alm_{0.49-0.52}$, $Py_{0.08-0.16}$, $Grs_{0.30-0.38}$, $Sps_{0.04-}$

$_{0.09}$). The outline of the previous core is only preserved by the high values in the spessartine maps, indicating that this component was relatively unaffected by later growth events (Figure 6b, e). The core relicts are interconnected by apparent channel-like structures visible in the pyrope and, to a lesser degree, in the grossular maps that engulf the cores (zone II).

Zone II (Figure 6b-f) is characterized by a step decrease of almandine contents and a slight increase of pyrope contents ($Alm_{0.47-0.48}$, $Py_{0.16-0.17}$). In addition, the grossular and spessartine contents slightly decrease ($Grs_{0.28-0.30}$, $Sps_{0.01-0.02}$). Zone II is limited, in general, by the trail of inclusions in the atoll garnets (Figure 6a, b). However, in some grains, this zone extends to a few microns beyond the inclusions, showing embayment textures in the proximity to zone III.

Zone III (Figure 6b-f) is a transitional zone between the mantle and the rims with ~ 100 µm of width characterized by a steadily increase in pyrope and almandine contents ($Py_{0.18-0.23}$, $Alm_{0.49-0.54}$) coupled with a smooth and step decrease of grossular and spessartine contents ($Grs_{0.27-0.22}$, $Sps_{\sim 0.00-0.01}$), respectively.

Finally, zone IV (Figure 6b-f) is represented by garnet rims with high pyrope and almandine contents ($Py_{0.23-0.27}$, $Alm_{0.53-0.55}$) mirrored by low grossular and spessartine contents ($Grs_{0.15-0.22}$, $Sps_{\sim 0.00}$). In the pyrope and spessartine maps, the rims exhibit narrow channels perpendicular to the grain surface showing a decrease and increase in their contents ($Py_{\sim 0.20}$, $Sps_{0.01-0.02}$), respectively (Figure 6b).

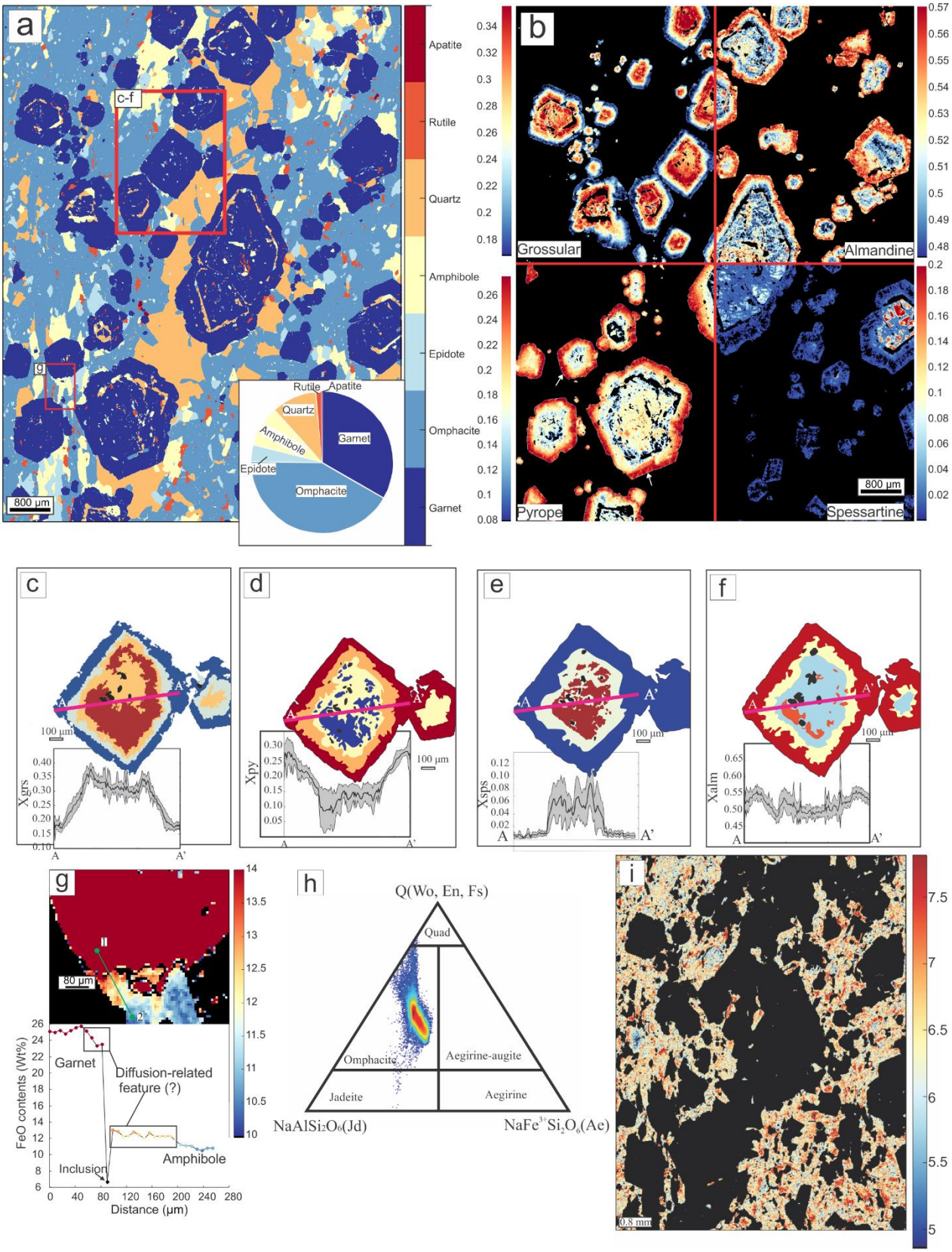

Figure 6 X-Ray images from sample 171. (a) mask image showing the minerals present and their proportion in the analyzed section of the sample. In (b) are the molar fraction of the garnet components; grossular (XGrs), almandine

(XAlm), pyrope (XPy), and spessartine (XSpss). The image corresponds to the same image as in (a), but each garnet component is displayed on every quadrant of the image. Moreover, the correspondent color bar is displayed next to the correspondent component. In (c-f) is displayed a sketch of a garnet highlighted in (a), showing the main compositional zones according to each garnet component. The color of each zone corresponds to the mean composition in the color bar from (b). A compositional profile obtained in the XMapTools is also displayed. The gray field corresponds to the standard deviation calculated by the program. (g) The effects of diffusion at the contact between garnet and amphibole are observed in a compositional map of FeO wt% and a profile. They show a striking increase of this oxide at the rims of amphibole and in less proportion on garnet.

4.4.2. Pyroxene, amphibole, and epidote

Following the classification scheme of Morimoto (1988), the pyroxene minerals of Raspas Metamorphic Complex are essentially omphacite with normalized jadeite contents ranging between 0.09 – 0.45. This classification is consistent with compositional zoning observed in the X-ray maps, where in some portions of the matrix, the omphacite exhibits low Na_2O contents (~ 4 wt. %). Whereas the remaining omphacite, including those included in garnet, possess higher Na contents (~ 6.5 wt. %), although, at the rim of some omphacites, the Na contents are noticeably higher, reaching up to ~ 7.5 wt. % (Figure 6h, i).

The amphiboles do not show compositional variation and correspond to katophorite, following the nomenclature scheme of Hawthorne et al. (2012). Only in the Fe map does this mineral display slight zoning with an apparent increase at some garnet margins, indicating cation exchange during diffusion (Figure 6g). Their Mg# varies from 0.70 to 0.75, the Si a.p.f.u. from 6.63 to 6.83, Fe^{3+} from 0.09 to 0.11, and Na_B from 0.66 to 0.71.

The epidote group minerals have X_{Fe} ($Fe^{3+}/(Fe^{3+}+Al)$) ranging between 0.14 to 0.17. The molar fraction of epidote (X_{Ep}) shows slight zoning, with a cores composition of X_{Ep} ~ 0.9 and rims ~0.3.

Thermodynamic Modeling and P-T Constraints

In order to constrain the metamorphic evolution, interactive thermodynamic modeling in the Bingo-Antidote program was performed (XMapTools add-on, Duesterhoeft, and Lanari, 2020),

coupled with isochemical phase diagrams in the Theriak-Domino (de Capitani and Brown, 1987), and independent thermometer with Zr-in rutile thermometry (Tomkins et al., 2007).

In the compositional map of the eclogite sample 171, the mineral proportions are omphacite (41%), garnet (33%), quartz (10%), amphibole (9%), epidote (4%), rutile (1%), and apatite (~1%) (Figure 7a); where the last two minerals were not considered in the further modeling. In all models, the chemical system utilized was the NCFMASH with water set in excess. The Mn was excluded due to the low contents, K due to the lack of minerals bearing this element in the map and Ti because the only mineral phase incorporated is rutile. The thermodynamic database utilized was from Holland and Powell (1998), version 3.30.

For the first identified assemblage (Stage I), the cores of garnet (zone I) were considered in equilibrium with quartz, the amphibole with less than 11 wt. % of Fe to avoid the crystals affected by diffusion (Figure 6g), and omphacite with Na contents ~ 6.5 wt. % was selected because it is included in the garnet cores and the atoll textures. This model did not consider the omphacite with low Na contents because they lack a clear equilibrium relationship with other minerals. Recipe 1 of Bingo-Antidote, which finds the optimal P-T for a fixed X, showed a good fit with the observations (Figure 7a, 5c), resulting in a quality factor total (Q_{tot}) of 85% for P-T conditions at 598°C and 1.43 GPa (Figure 5c; Figure A.1).

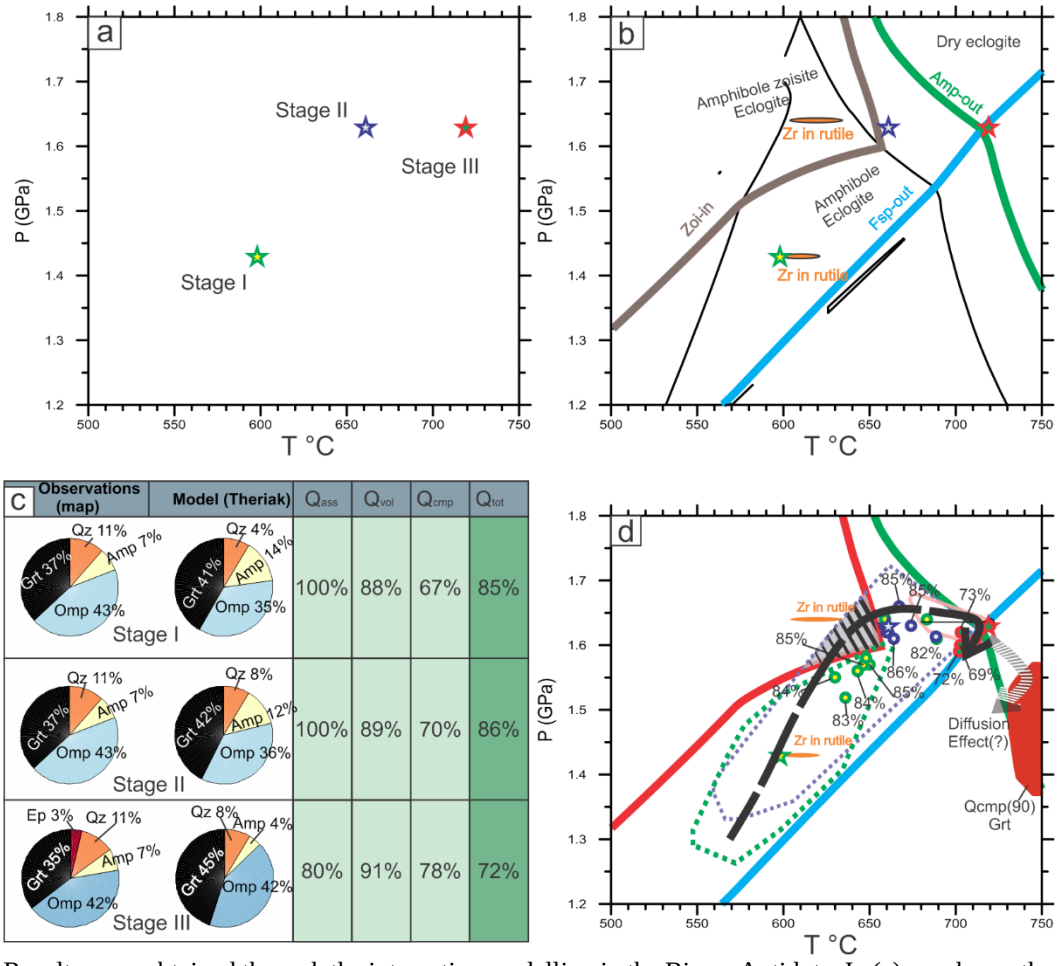

Figure 7 Results were obtained through the interactive modelling in the Bingo-Antidote. In (a) are shown the pressure-temperature (P-T) conditions for every metamorphic Stage described in the text. The mineral proportions observed and modeled are shown in (c). The P-T conditions in (a) are superimposed with a pseudosection in (b) with the main mineral curves highlighted and the results of the Zr-in- rutile thermometry. The uncertainty for each Stage is plotted in (d). The circles represent the P-T conditions for a variable composition (Recipe 3) and their respective total quality factor. The dashed field in (d) represents the possible window for the zoisite growth. A possible trajectory is displayed by the black dashed arrow, whereas the gray dashed arrow represents the possible effects of diffusion. The red field represents the high Q_{cmp} for the garnet during Stage III. The quality factors (Q) are a measure of how the modeling got close to the observation, whether the assemblages (Q_{ass}), the volume of the phases (Q_{vol}), or their composition (Q_{cmp}).

The second assemblage identified (Stage II) considers the same composition for amphibole, omphacite, and quartz, because there is no evidence of a new phase growth during the formation of the atoll texture. Thus, we considered only the growth of zone II of garnet during the formation of the atoll texture. Due to the nature of the atoll texture being the interaction of the growing mineral with a metamorphic fluid (Faryad et al., 2010), the garnet composition chosen was considered possible mixing behavior. Then were selected portions of zone II immediately outside the atoll texture to avoid the influence of the channel features close to the core. Again, a good fit was

observed between the observations and model with Q_{tot} = 86% at 661°C and 1.63 GPa (7igure 5a, c; Figure A.3).

At last, a third assemblage (Stage III) represented by the garnet rims, the epidote rims with high zoisite contents, the omphacite with high Na contents, and the same amphibole as the previous assemblage were considered in equilibrium. This time, the Q factors resulted in lower values with Q_{tot} = 72% at 709°C and 1.61 GPa because the epidote was not predicted in the model (Figure 7a, c; Figure A.5). A possible explanation is that the model did not account for the ferric iron incorporated in the epidote. Then, we ran the same model but added a small amount of oxygen set in excess (0.001 mols). They resulted in a Q_{tot} = 92 % at slightly higher P-T conditions (719 °C and 1.63 GPa) with the presence of epidote. However, the model with excess oxygen overestimated the epidote's stability field in the whole P-T window.

In Figure 7b, the P-T conditions obtained are superimposed with an isochemical phase diagram without O in excess. In it, the P-T conditions and uncertainty of Stage II are close to the stability field of amphibole-zoisite eclogite, which may suggest that the epidote was formed earlier, still during Stage II, although this mineral exhibit equilibrium textures with the garnet rims.

All stages of our model have a noticeable compositional difference between the minerals observed and the model, with a Q_{cmp} that varies from 67 to 78 %, as shown in the quality factor maps (Figure A.2, A.4, A.6). The lower Q_{cmp} of garnet probably has bigger influence in the total Q_{cmp} than the other minerals (Figure A.2, A.4, A.6) that reach up to 40 % (stages I and II, for example). For this mineral, the Q_{cmp} increases at lower P-T conditions for stages I and II indicating that the onset of garnet growth was earlier (Figure A.2, A.4). For the garnet rims, the Q_{cmp} is higher (close to 90 %; Figure A.6) at T above 730°C (Figure 7d), which implies, to a certain degree, the influence of the diffusion between the garnet rims and amphiboles in the model.

DISCUSSION

The protoliths of the Raspas high-pressure rocks

The whole rock geochemical result suggests that the Raspas metabasites have a heterogeneous mantle source according to the Zr/Nb ratios (7.69 – 112.66). The latter suggests that oceanic island basalts (OIB) (Zr/Nb ratios < 10) and MORB (Zr/Nb ratios >>30) signatures characterized these protoliths. Furthermore, when Zr/Nb is compared with La/Y and La/Sm_N (Figure 5a, b), the Raspas lithologies show a variation trend from E-MORB to N-MORB, the blueschist exhibit an E-MORB signature and the greenschist and garnet amphibolites are more akin to an N-MORB signature.

Low La/Yb and high Sm/Yb ratios are related to an increase in the partial melting degree and the depth where this occurs (Chen et al., 2021). Moreover, Sm/Th and Th/Y can hint at the relationship between enrichment and a partial melting degree in the source (Chen et al., 2021). Accordingly, from figures 5c and 5d, coupled with the fact that these rocks were not dismembered during subduction (i.e., they functioned as a coherent block), we can affirm that the metabasites from Raspas Metamorphic Complex share the same protolith, although related to variable degrees of partial melting, enrichment, and depth.

So, from figure 4 and 5, we can infer that the blueschists were the result of the lower degree of partial melting from an enriched, relatively plagioclase-free (Eu/Eu* = 0.97 – 1.72 and slight positive anomaly of Sr; Figure 4), and deeper source than the eclogites, greenschists, and garnet amphibolites from the Raspas Metamorphic Complex. Conversely, the protoliths of the eclogite, greenschist, and garnet amphibolite can be interpreted as the result of a variable degree of partial melting from a shallower and less enriched source than the blueschists (Figure 5) with a small degree of plagioclase retention in the source (Eu/Eu* = 0.87 – 1.12; negative Sr anomaly in some

samples; Figure 4). Although the eclogites and blueschists show characteristics of two endmembers (Figure 5c), figure 5d currently demonstrates a continuous variation, which indicates a continuous change as the depth and degree of partial melting in the source changed.

John et al. (2010) attributed such a heterogeneous source with variable degrees of partial melting and enrichments at different depths to forming seamounts with E-MORB signature into, or close to, an N-MORB ridge. However, they did not consider that the blueschist and eclogite coexist at a local scale without any limiting structure. Moreover, the oceanic plateau data compiled from GEOROC (Table A.1) and summarized in the boxplots of Figure 8c-e are very similar to the Raspas metabasites, where only a few samples plot below the oceanic plateau data, suggesting at least some degree of MORB component contributed for the protolith of the Raspas Metamorphic Complex.

Kerr et al. (2000) have pointed out that the OIB is more enriched in incompatible trace elements than oceanic plateaus. This signature is the result of melting at greater depths in the garnet stability field, which reflects the high $(Sm/Yb)_N$, Nb/Zr, and La/Y observed in OIB lavas (5.14, 0.17, 1.27, respectively; Sun and McDonough, 1989). These ratios for the eclogites of the Raspas Metamorphic Complex are 0.92-2.17, 0.02-0.13, and 0.05-0.64, respectively. In the $(Sm/Yb)_N$ vs. $(La/Nd)_N$ diagram (Figure 8a), Raspas metabasites plot parallels the $(La/Nd)_N$ axis, similar to the Ontong Java or Caribbean Plateaus. The OPB signature of the Raspas Unit is also supported by the near-flat REE pattern typical of the several well-known oceanic plateau (e.g., Ontong Java, Caribbean, or Kerguelen; Figure 4). Moreover, the samples fall essentially in the Iceland array in the Zr/Y – Nb/Y diagram of Fitton et al. (1997). Although, some samples plotted below this array in the MORB field (Figure 8b) indicate a MORB component or possible Nb loss during metamorphism, as seen in the samples with low Nb in the binary diagrams of Figure 3a-f. The

Raspas metabasites also exhibit variable ΔNb (Fitton et al., 1997); eclogite = -0.43 – 0.36 (mean of 0.09), blueschist = -0.76 – 0.17 (mean of 0.04), garnet amphibolite = -0.67 – 0.28 (mean of 0.04), and greenschist = 0.39 – 0.10 (mean of 0.25); that suggest a hybrid enriched plume-like (ΔNb > 0) to a depleted MORB-like source (ΔNb < 0). This small variations in ΔNb is also common in other typical oceanic plateau formed by mantle plumes (Kerguelen = -1.00 – 0.51, mean of -0.01; Ontong Java = -1.81 1.23, mean of 0.08; Caribbean = -5.49 5.99 mean of 0.15; data calculated from the GEOROC database available in the Table A.1).

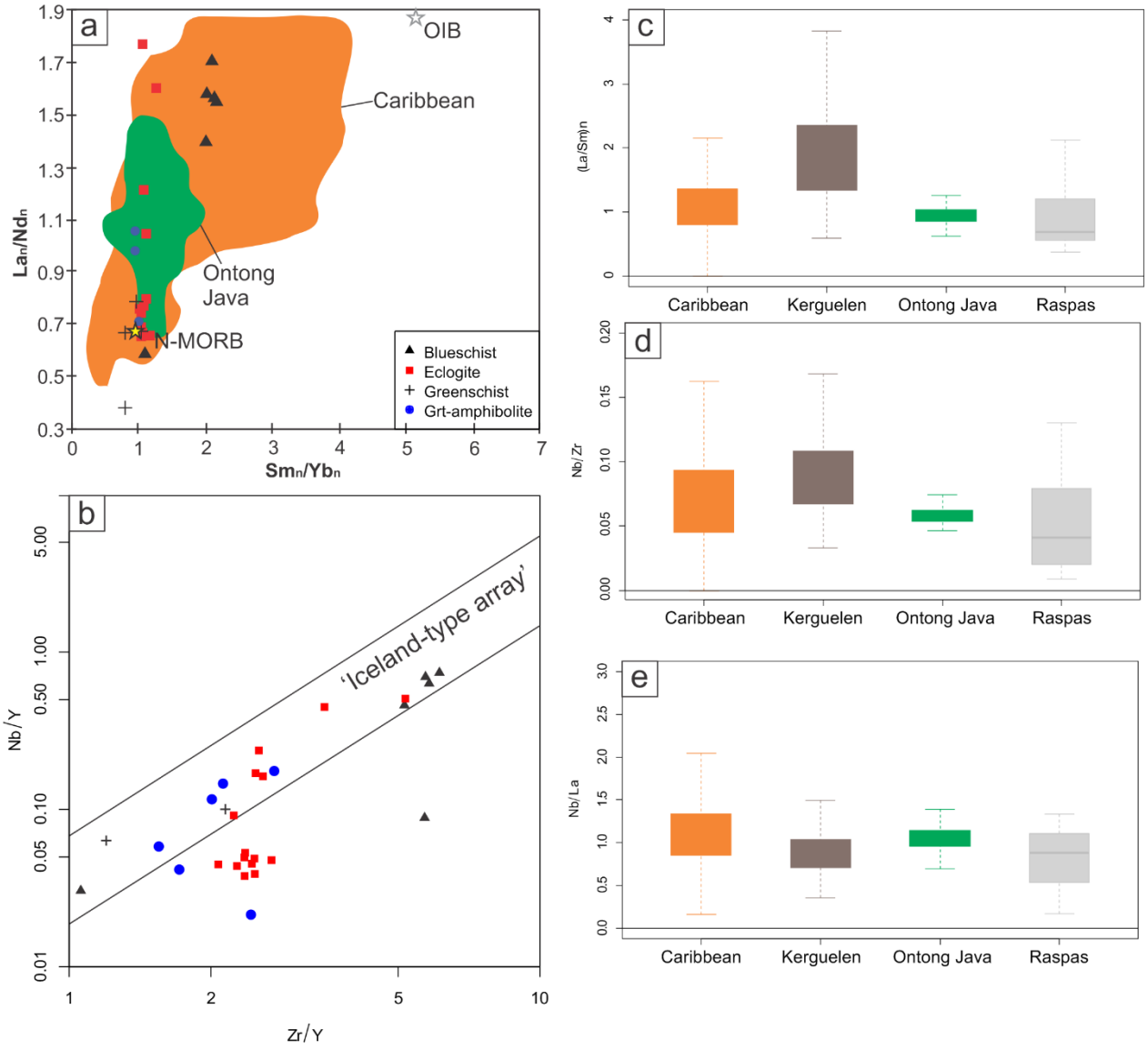

Figure 8 (a) La_N/Nd_N vs. Sm_N/Yb_N (chondrite-normalized following Sun and McDonough, (1989) values) diagram comparing the Raspas metabasites with the Caribbean and Ontong java Plateaus. (b) Nb/Y vs. Zr/Y diagram after Fitton et al. (1997) shows the Raspas Complex's concordance with plume-related rocks. (c-e) boxplot comparing La_N/Sm_N, Nb/Zr, Nb/La ratios from Kerguelen, Caribbean, and Ontong java plateaus with the Raspas Complex. The data used in the comparison are from the GEOROC database and are available in Table A.1.

According to the geochemical characteristics of the Raspas Metamorphic Complex, we envisage a basic protolith formed in an oceanic plateau with a minor MORB component. This apparent dual signature may indicate that during the plume ascension, the increasing degree of partial melting due to the decompression along the melt column favors incorporating a depleted component from its surroundings, diluting the original enriched signature (Kerr et al., 2002b). Consequently, they

resulted in two end-members materials with distinct signatures and samples with an intermediate signature.

The geochemical trend between these two endmembers (i.e., plume-originated oceanic plateau and MORB) becomes apparent when the Raspas metabasites are displayed in the Th/Y vs. Sm/Th diagram (Figure 5d). In this diagram, we can see an enriched material with a signature similar to primitive mantle typical of a lower degree of partial melting at great depths, represented by blueschist and some eclogite samples. This signature is followed by an incipient trend shown by the continuous increase of a depleted and shallower material until it gets very similar to an N-MORB, where most of the eclogites, greenschists, garnet amphibolites, and some blueschists samples fit.

Considering the metamorphic ages of ca. 130 Ma for the Raspas Unit, and despite the absence of direct protolith ages, it is possible to speculate that due to the Caribbean plate affinity of the metabasic rocks, that may be part of the older and less extensively preserved stages reported for the oceanic plateau evolution, which has been considered as old as 139 Ma (Hoernle et al., 2004).

Metamorphic evolution of the Raspas eclogite

As seen in the previous sections, the metamorphic evolution registered by the sample does not involve significant mineralogic changes. However, the changes in the composition of their assemblage hide critical information about the dynamic during the metamorphic path.

The wide P-T window in which the eclogite assemblage grew up (Stage I 550 – 650 °C and 1.3 – 1.6 GPa; Figure 7d) coupled with the low Q_{cmp} observed in the modeling suggest that the eclogite transformation of Raspas metabasites proceeded through hindered kinetic conditions. When the Q_{cmp} of each mineral are compared, we see that, especially for garnet and amphibole, their Q_{cmp}

increases under different conditions (Figure A.2, A.4, A.6), which explains the wide error calculated during the modeling. Therefore, suggesting that the equilibration of these minerals was favored in lower conditions.

We do not rule out that at least garnet was formed earlier in the metamorphic path. However, significant changes are observed along the P-T path when the effective composition is considered. This conclusion was possible using recipe 11 of Bingo-Antidote, which shows significant variation in the resulting P-T conditions during Stage I of our model (Figure 7d). Nevertheless, for the latter two stages, the resulting P-T is more constrained close to the initial results (Figure 7d). The minimum and maximum pressure obtained through recipes 1 and 11 for Stage I was then utilized to calculate the Zr-in-rutile thermometry (Figure 7b). That resulted in a narrow T range from 590 to 630 °C consistent with the P-T conditions of Stage I.

Although the assemblage attained the conditions for their formation at lower P-T, the Zr-in-rutile thermometry suggests that considerable overstepping was needed (e.g., Spear, 2017) during the early stages of eclogitization. For example, if we consider the P-T uncertainty of Stage I and the independent thermometer utilized, the amount of overstepping could be around 50°C.

The presence of zoisite in equilibrium outside the field predicted by the thermodynamic modeling suggest that the crystallization of this mineral was hindered due to kinetics and needed a certain degree of overstepping (Spear and Pattison, 2017), or it crystallized due to the fluid interaction during the formation of the atoll garnet at the P-T interval between stages II and III. Although there is evidence of an extensive fluid transfer and interactions in the Raspas Complex (Herms et al., 2012), however, if the zoisite observed in the sample was formed during fluid input, it is expected to this mineral being present along fractures (e.g., Hyppolito et al., 2018) or the channel features in the atoll garnet.

The formation of the atoll garnet at ~660 °C and 1.6 GPa (i.e., Stage II) during the interaction with fluids (Herms et al., 2002) probably triggered dramatic changes in the kinetic rates of reaction. Thus, working as a catalyst changing from protracted growth to normal growth rates. Furthermore, the extensive solid-state modification registered them in the composition of garnet cores by an intense cation exchange between garnet and the fluid (i.e., interconnected channel-like structures close to garnet cores; Figure 6b-f).

The latest metamorphic event (Sage III) registers an increase in thermal influx during isobaric conditions (709°C and 1.61 GPa). Reflected by the diffusion features present in amphiboles in contact with garnet (Figure 6g), the rock remained under peak metamorphic conditions for some time before exhumation. However, it was insufficient to cause noticeable diffusion patterns on garnet margins.

Tectonic mechanisms for the origin of the Raspas Metamorphic Complex

In this contribution, we demonstrate that the protoliths of the Raspas Metamorphic Complex as part of an oceanic plateau. So, in this section, we debate the P-T path these rocks take in light of the subduction of an oceanic plateau.

The P-T conditions for Raspas eclogite indicate a subduction regime under a low T/P gradient of ~406 °C/GPa at ~50 km depth. Considering that the 133 Ma Lu/Hf ages represent the baric peak and the phengite Ar-Ar ages of 123 - 129 Ma as the cooling ages (Gabriele, 2002; this work), they point to fast exhumation rates of 1.25 to 0.5 cm/yr. However, cation-exchange diffusion features between garnet and amphibole (Figure 6g) suggest that the rock remained under peak conditions for some time before exhumation. Thus, the abovementioned exhumation rates represent the minimum velocity at which they came to the shallow crustal depths.

Another remarkable aspect of the P-T history is the presence of isobaric heating (difference of 0.02 GPa for ~50°C) between Stages II and III. This feature which is common in other orogens (Cheng and Cao, 2015; Marian et al., 2020; Groppo et al., 2009), can be related to (1) thermal equilibration of the slab through heat transfer (England and Thompson, 1984), (2) slow detachment from the downgoing slab followed by underplating in the mantle wedge (Cheng and Cao, 2015), or (3) asthenosphere flow during slab roll-back (Brun and Faccenna, 2008).

The oceanic plateau origin of the Raspas Metamorphic Complex precludes thermal equilibration as a major mechanism as due to its thickness (~20 km). For example, the time needed for an oceanic plateau to attain thermal equilibration, considering a thermal diffusivity of 10^{-6} m s^{-2} (Turcotte and Schubert, 2002), is >50 Ma, thus inconsistent with the short time between the baric peak and cooling of 10-6 Ma experienced by the Raspas metabasites.

If the HP rocks from Raspas Unit were detached from the downgoing slab before the isobaric heating, again, once detached, they would need to remain in contact with hot material during underplating for some time to suffer isobaric heating. Moreover, the increase of temperature would be coupled with decompression representing the early stages of exhumation.

The most feasible mechanism for the isobaric heating experienced by these rocks is during a roll-back. Considering the numeric models, the early stages of subduction of the oceanic plateau coupled with the preservation of lower-grade rocks during the eclogitization and weakening of the mantle wedge would result in a flat slab geometry (Liu et al., 2021 and references within), similar to the Laramide orogen (Liu et al., 2010). Moreover, as the degree of eclogitization increases and the density subsequently increases, the pull forces would bend the plateau, thus originating a roll-back.

Therefore, accordingly, due to the partial eclogitization observed in the Raspas Metamorphic Complex (i.e., the presence of blueschists coexisting with eclogites), it is possible that when their protolith (here named Raspas Plateau) arrived at the subduction, the initial low buoyancy would cause a flat slab geometry (Figure 9), as evidenced by the gap of magmatic activity at 130 Ma in the southern portion of Northern Andes (i.e., southern Colombia to the north of Ecuador; Bustamante et al., 2016). Similar to the present-day absence of volcanic activity in some portions of the Andean margin due to flat slab geometry (Gutcher et al., 2000).

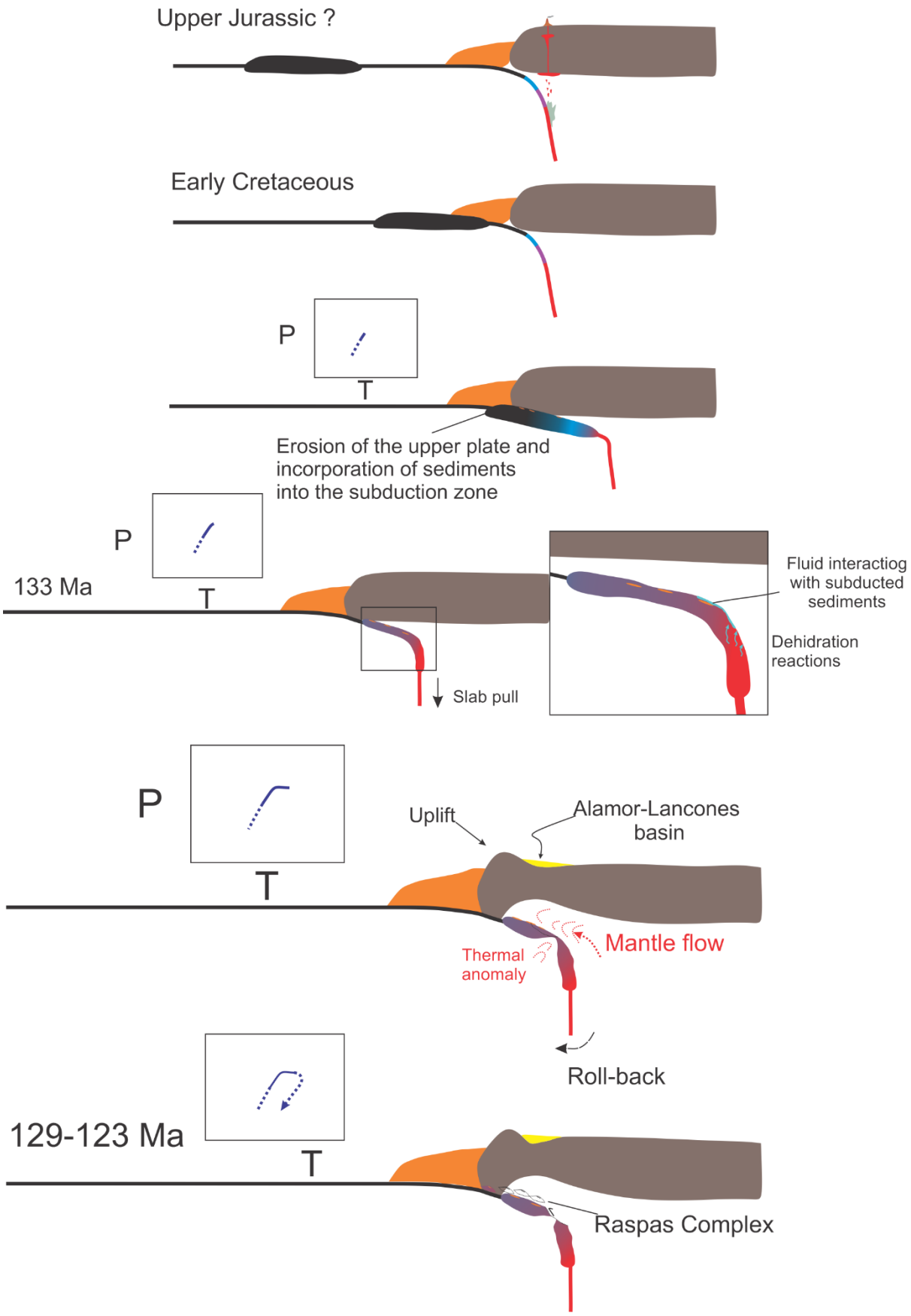
Upper Jurassic ?
Early Cretaceous
P
T
Erosion of the upper plate and
incorporation of sediments
into the subduction zone
P
T
133 Ma
Fluid interactiog
with subducted
sediments
Dehidration
reactions
Slab pull
P
T
Uplift
Alamor-Lancones
basin
Mantle flow
Thermal
anomaly
Roll-back
129-123 Ma
T
Raspas Complex

Figure 9 Sketch showing the tectonic evolution of the Raspas Complex. From top to bottom: The plateau of the Jurassic age traveled towards the Andean margin until it interacted with the continental margin at the transition Jurassic-Cretaceous. As the plateau arrived at the trench, continental sediments were scrapped and carried towards the mantle. At 133 Ma, due to the low buoyancy of the plateau, a flat slab geometry was formed. At this stage, fluid originated from the dehydration of parts eclogitized and traveled upwards, interacting with the continental sediments incorporated and portions that preserved blueschist assemblages (Raspas Complex). At this point, the slab-pull forces, originated by the portions eclogitized, were so strong that they started to bend and thin the subducted plateau creating a roll-back event. This context created a thermal anomaly reflected in the isobaric heating in the Raspas eclogites. Finally, between 129-123 Ma, the mantle flow originated from the roll-back was the mechanism behind the exhumation of the Raspas Complex.

During this initial Stage, the top of the Raspas Plateau caused the erosion of the overriding plate (Stern, 2011), incorporating continental sediments into the subduction channel, as evidenced by the continental affinity of HP metapelites present at the Raspas Metamorphic Complex (Figure 8; Bosh et al., 2002; Gabriele, 2002). As the Raspas Plateau reached deep portions, dehydration reactions during the formation of blueschist and later eclogite assemblages released fluids that percolated through the top of the plateau, interacted with sediments, and created the zoisite veins (Herms et al., 2002) and even trigger the formation of the atoll garnet.

As the Raspas Plateau was progressively transformed to eclogite, the increasing density favored the pull forces causing the bending of the plateau (Figure 9; Wu et al., 2008; Schellart, 2004). During this process, the increasing angle of subduction (i.e., roll-back) leads the asthenospheric mantle to invade the wedge (Alsaif et al., 2020). The mantle flow, caused by the roll-back in a few millions of years, triggered the weakening and thinning of the overriding plate (Figure 9; Arcay et al., 2006). Thus creating a thermal anomaly and extension in the forearc region; as registered by the isobaric heating shown in the P-T path, the formation of the Lower Cretaceous Alamor-Lancones Basin (Valarezo et al., 2019) and registered by zircon fission track of Marcabeli Pluton and La Victoria Unit in the El Oro Province (at 137 and 139 Ma, respectively; Spikings et al., 2005). Finally, we attribute the exhumation of the Raspas Complex to the bending and roll-back followed by a detachment of fragments from the plateau arising during an asthenosphere flow as an ophiolite (Phillips and Offler, 2011).

Riel et al. (2014) proposed a different mechanism for the evolution of the Raspas Metamorphic Complex between 140-120 Ma. They argue that a change in subduction directions from WSW to ENE developed a verticalization at the edge of the slab by toroidal movements at an asthenosphere window to explain the exhumation of Raspas eclogites and a thermal event present at El Oro province during an extensional event (Spikings et al., 2005). However, their model fails to explain the absence of magmatic and volcanic activity typical of slab window geometry in the region (Hole et al., 1991).

Implications for the evolution of the Northern Andes

In the Cretaceous, the Pacific realm experienced the origin of great volcanic activity during the formation of important oceanic plateaus. Most of what we know about these features is from fragments left when they interacted with another slab. For example, the Andean orogeny registers several fragments of the Caribbean Plateau present along the Northern Andes from Ecuador to Venezuela. This event is believed to have occurred a few million years after forming the Caribbean Plateau in the Late Cretaceous (Vallejo et al., 2006). However, our study showed that the Northern Andes interacted with another oceanic plateau fragment still in the Early Cretaceous, denominated Raspas Plateau. Moreover, considering the numeric constraints, which affirm that an oceanic plateau must have > 40 Ma to subduct (Vogt and Gerya, 2014), put an age constraint of > 170 Ma for the origin of the Raspas Plateau.

The idea that the Cretaceous HP occurrences along the flanks of the Central Cordillera of the Northern Andes are part of the same subduction system is not new (e.g., Spikings et al., 2015). However, the metamorphic constraints of this work show that the Raspas Metamorphic Complex shares similar P-T conditions with the other HP occurrences of the Northern Andes. Except for the Pijao occurrence, which reached 2.0 GPa (75 km depth; Avellaneda-Jimenez et al., 2021), pressures

around 1.4-1.5 GPa (50 km depth; Bustamante, 2008; Massonne and Toulkeridis, 2012; this work) are found consistently along the belt. Moreover, the peak metamorphic conditions indicate that the subduction in the northern portion of the HP belt was colder due to the presence of lawsonite in Pijao (~500°C) and Barragán (~300-400).

The age constraints for the HP event along the Northern Andes show that it occurred in the Early Cretaceous between 133-125 Ma. When looking at the individual ages, it becomes clear that the Raspas Metamorphic Complex is slightly older (~133 Ma; John et al., 2010) than the Pijao (~128 Ma; Avellaneda-Jimenez et al., 2021) and Barragán (~125 Ma; Bustamante et al., 2012), thus indicating that the HP event developed from south to north. The exhumation event, constrained between 118-129 Ma, overlaps with the HP event and again started with Raspas Metamorphic Complex at 123-129 Ma (Gabriele, 2002; this work) and extended to Barragán at 120 Ma (Bustamante et al., 2012) and Pijao at 118 Ma (Avellaneda-Jimenez et al., 2021).

The mechanism for the Barragán blueschists' exhumation is still uncertain, but the mechanism proposed for Pijao and presented by this work for Raspas is the same; a roll-back. Avellaneda-Jimenez et al. (2021) observed that during the exhumation of the Pijao eclogites, an increase in temperature was coupled with the decompression. They interpreted this as a result of a thermal influx of hot mantle during a roll-back. As mentioned in the earlier sections, the eclogites from Raspas suffered a similar thermal influx prior to exhumation. Therefore, it was probably caused by slab-pull forces that originated from buoyancy changes during the eclogitization of the Raspas Plateau. This process, therefore, caused a change from a flat slab geometry to a roll-back. So, when we put together the exhumation ages with a similar mechanism of exhumation, it is feasible to affirm that a regional roll-back event started from south to north in ~120 Ma, which was caused by the subduction of the Raspas Plateau.

CONCLUSION

This contribution presented new geochemical, geochronological, and metamorphic data that allowed to constrain of the protolith, metamorphic conditions, and cooling ages of the Raspas Metamorphic Complex.

Their geochemistry shows rocks with primitive mantle-normalized trace element plots flat HREE and variable LREE (enrichment or depletion) patterns typical of N- to E-MORB. Trace element ratios evidence a heterogeneous mantle source (Zr/Nb – 7.69-112.66) characterized by a continuous increase of partial melting degree and depth from blueschists (La/Yb – 4.89-6.86; Sm/Yb – 1.81-1.95) to eclogites (La/Yb 0.76-1.80; Sm/Yb 0.94-1.06). Moreover, diagrams of chondrite-normalized trace element ratios show similarities between Raspas metabasites and oceanic plateau lavas, which was confirmed by the Zr/Y vs. Nb/Y diagram of Fitton et al. (1997) where they plot in the Iceland array. Accordingly, the N- to E-MORB signature coupled with their protolith heterogeneity and trace element similarities with oceanic plateau lavas evidences an enriched protolith for the Raspas Metamorphic Complex originated during the ascension of a mantle plume.

Interactive thermodynamic modeling in the Bingo-Antidote (Duesterhoeft and Lanari, 2020) revealed a complex metamorphic evolution during the subduction of the oceanic plateau that originated this complex, henceforth named Raspas Plateau. During the early stages of subduction, the Raspas Plateau eroded some parts of the continental plate incorporating sediments in the subduction. Due to the low buoyancy of the plateau, it favored the formation of a flat slab geometry, reflected by the absence of magmatic activity coeval to this event (~130 Ma; Bustamante et al., 2016) in the region.

The metamorphism proceeded through a low T/P gradient of ~406 °C/GPa. After an overstepping of around 50 °C, the first metamorphic Stage resulted in the assemblage of garnet$_{(core)}$, quartz, katophorite, and omphacite cores at around 598 °C and 1.43 GPa. Chemical potential diagrams reveal that during the first metamorphic Stage, the assemblage developed through a large P-T interval as the pressure increased, which can be constrained at ~133 Ma (John et al., 2010). The same assemblage remained in equilibrium during the compression until it reached 661 °C and 1.63 GPa; that was when the atoll garnet textures and zoisite were formed. The formation of the atoll garnet has imprinted evidence of fluid-rock interactions, evidenced by channel-like structures with different compositions at the garnet mantle.

The formation of eclogitic assemblages decreased the buoyancy, favoring pull forces resulting in the plateau slab bending and sinking (Figure 8; Wu et al., 2008; Schellart, 2004). During this process, the increasing angle of subduction (i.e., roll-back) leads the asthenospheric mantle to invade the wedge (Alsaif et al., 2020). That, coupled with the weakening of the plateau, caused a thermal anomaly. This process triggered extension at the forearc resulting in the formation of the Lower Cretaceous Alamor-Lancones Basin (Valarezo et al., 2019), also registered by the zircon fission track of Marcabeli Pluton and La Victoria Unit in the El Oro Province (at 137 and 139 Ma, respectively; Spikings et al., 2005). Moreover, the last metamorphic Stage reveals that this feature caused isobaric heating at 709 °C and 1.61 GPa resulting in the assemblage of garnet $_{(rim)}$, zoisite$_{(rim)}$, omphacite$_{(rim)}$, and katophorite.

Our work demonstrated that the Andes interacted with another oceanic plateau, probably formed before 170 Ma, during the Early Cretaceous. Their subduction formed an HP belt that extends to Colombia around 130 Ma (Avellaneda-Jimenez et al., 2021; Bustamante et al., 2012; John et al., 2010). Moreover, cooling ages suggest that the exhumation was quick, with onset

around 126-123 Ma (Raspas Metamorphic Complex; Gabriele, 2002; this work) until 118 Ma (Pijao eclogites; Avellaneda-Jimenez et al., 2021) during a regional roll-back event originated at Ecuador.

ACKNOWLEDGMENTS

This study was supported by the brazilian agencies National Council for Scientific and Technological (CNPq) grant 458735/2014-0 and Fundação de Amparo à Pesquisa do Estado de São Paulo (FAPESP) grant 2004/10203-7. S. P. da Silva thanks the Coordenação de Aperfeiçoamento de Pessoal de Nível Superior – Brasil (CAPES) - Finance Code 001 by the partial financial support.

REFERENCES

Alsaif, M., Garel, F., Gueydan, F., Davies, D. R., 2020. Upper plate deformation and trench retreat modulated by subduction-driven shallow asthenospheric flows. Earth and Planetary Science Letters 532, 116013.

Arculus, R.J., Lapierre, H., Jaillard, E., 1999. Geochemical window into subduction and accretion processes: Raspas metamorphic complex, Ecuador. Geology 27, 547-550.

Aspden, J. A., Bonilla, W., Duque, P., 1995. The El Oro metamorphic complex, Ecuador: geology and economic mineral deposits. Nottingham, British Geological Survey, Overseas Geology and Mineral Resources 67, p. 63.

Aspden, J. A., Litherland, M., 1992. The geology and Mesozoic collision history of the Cordillera Real, Ecuador. Tectonophysics 205, 197-204.

Avellaneda-Jimenez, D. S., Cardona, A., Valencia, V., León, S., Blanco-Quintero, i. F., 2021. Metamorphic gradient modification in the Early Cretaceous Northern Andes subduction zone: A record from thermally overprinted high-pressure rocks. Geoscience Frontiers https://doi.org/10.1016/j.gsf.2020.09.019

Bosch, D., Gabriele, P., Lapierre, H., Malfere, J., Jaillard, E., 2002. Geodynamic significance of the Raspas Metamorphic Complex (SW Ecuador): geochemical and isotopic constraints. Tectonophysics 345, 83-102.

Brandelik, A., 2009. CALCMIN ¬ an Excel TM visual basic application for calculating mineral structural formulae from electron microprobe analyses. Computers & Geosciences 35, 1540-1551.

Brun J. P., Faccenna C., 2008. Exhumation of high-pressure rocks driven by slab roll-back. Earth and Planetary Science Letters 272, 1–7.

Bustamante, A., 2008. Geotermobarometria, geoquímica, geocronologia e evolução tectônica das rochas da fácies xisto azul nas áreas de Jambaló (Cauca) e Barragán (Valle del Cauca), Colômbia. Thesis -Instituto de Geosciências, Universidade de São Paulo, São Paulo, 179p.

Bustamante, A., Juliani, C., Essene, E. J., Hall, C. M., Hyppolito, T., 2012. Geochemical constraints on blueschist- and amphibolite-facies rocks of the Central Cordillera of Colombia: the Andean Barragán region. International Geological Review 54, 1013-1030.

Bustamante, C., Archanjo, C. J., Cardona, A., Vervoort, J. D., 2016. Late Jurassic to Early Cretaceous plutonism in the Colombian Andes: A record of long-term arc maturity. Geological Society of America Bulletin 128, 1762-1779.

Bustamante, C., Bustamante, A., 2019. Two Cretaceous subduction events in the Central Cordillera: Insights from the high P–low T metamorphism. In: Gómez, J. & Pinilla–Pachon, A.O. (editors), The Geology of Colombia, Volume 2 Mesozoic. Servicio Geológico Colombiano, Publicaciones Geológicas Especiales 36, p. 485–498. Bogotá. https://doi.org/10.32685/pub.esp.36.2019.14

Bustamante, A., Bustamante, A., Cardona, A., Juliani, C., da Silva, S., 2021. Jambaló blueschist and greenschist protoliths in the Central Cordillera of the Colombian Andes and their tectonic implications for Late Cretaceous Caribbean-South American interactions. Journal of South American Earth Sciences 107, 102977.

Chen, S., Liu, J., Gao, R., Wang, Z., 2021. Geochemistry of Cretaceous basalts from the Ontong Java Plateau: Implications for the off-axis plume-ridge interaction. Chemical Geology 564, 119815.

Cheng, H., Cao, D., 2015. Protracted garnet growth in high-P eclogite: constraints from multiple geochronology and P–T pseudosection. Journal of Metamorphic Geology 33, 613-632.

Cloos, M., Shreve, R., 1988a. Subduction-Channel Model of Prism Accretion, Melange Formation, Sediment Subduction, and Subduction Erosion at Convergent Plate Margins: 1. Background and Description. Pure and Applied Geophysics 128 (3-4), 455-500.

Cloos, M., Shreve, R., 1988b. Subduction-channel model of prism accretion, melange formation, sediment subduction, and subduction erosion at convergent plate margins: 2. Implications and discussion. Pure and Applied Geophysics 128 (3-4), 501-545.

de Capitani, C., Brown, T. H., 1987. The computation of chemical equilibrium in complex systems containing non-ideal solutions. Geochimica et Cosmochimica Acta 51, 2639-2652.

Duesterhoeft, E., Lanari, P., 2020. Iterative thermodynamic modelling Part 1: A theoretical scoring technique and a computer program (Bingo-Antidote). Journal of Metamorphic Geology 38, 1-25.

England P. C., Thompson A.B., 1984. Pressure–Temperature–Time Paths of Regional Metamorphism I. Heat Transfer during the Evolution of Regions of Thickened Continental Crust. Journal of Petrology 25(4), 894–928.

Ernst, W. G., 1988. Tectonic history of subduction zones inferred from retrograde blueschist P-T paths. Geology, 16, 1081-1084.

Ernst, W. G., Liou, J. G., 2008. High- and ultrahigh-pressure metamorphism: Past results and future prospects. American Mineralogist 93, 1771-1786.

Faryad, S. W., Klápová, H., Nosál, L., 2010. Mechanism of formation of atoll garnet during high-pressure metamorphism. Mineralogical Magazine 74, 111-126.

Feininger, T., 1980. Eclogite and related high-pressure regional metamorphic rocks from the Andes of Ecuador. Journal of Petrology, 21, 107-140.

Fitton, J. G., Saunders, A. D., Norry, M. J., Hardarson, B. S., Taylor, R. N., 1997. Thermal and chemical structure of the Iceland plume. Earth and Planetary Science Letters 153, 197-208.

Gabriele, P., 2002. HP terranes exhumation in an active margin setting: geology and geochemistry of the Raspas Complex in SW Ecuador. Unpublished Ph.D. thesis, University of Laussane, Switzerland.

Gabriele, P., Ballèvre, M., Jaillard, E., Hernandez, J., 2003. Garnet-chloritoid-kyanite metapelites from the Raspas Complex (SW Ecuador): a key eclogite-facies assemblage. European Journal of Mineralogy 15, 977-989.

Groppo, C., Foster, M., Lister, G., Campagnoni, R., 2009. Glaucophane schists and associated rocks from Sifnos (Cyclades, Greece): New constraints on the P–T evolution from oxidized systems. Lithos 109, 254-273.

Harrison, T.M., Celerier, J., Aikman, A.B., Hermann, J., Heizler, M.T., 2009. Diffusion of 40Ar in muscovite. Geochimica et Cosmochimica Acta, 73, 1039-1051.

Hastie, A. R., Kerr, A. C., Mitchell, S. F., Millar, I. L., 2008. Geochemistry and petrogenesis of Cretaceous oceanic Plateau lavas in eastern Jamaica. Lithos 101, 323-343.

Hawthorne, F. C., Oberti, R., Harlow, G. E., Maresch, W. V., Martin, R. F., Schumacher, J. C., Welch, M. D., 2012. Nomenclature of the amphibole supergroup. American Mineralogist 97, 2031-2048.

Herms, P., John, T., Bakker, R. J., Schenk, V., 2012. Evidence for channelized external fluid flow and element transfer in subducting slabs (Raspas Complex, Ecuador). Chemical Geology 310-311, 79-96.

Hoernle, K., Hauff, F., van den Bogaard, P., 2004. 70 m.y. history (139–69 Ma) for the Caribbean large igneous province. Geology 32, 697-700.

Hole, M. J., Rogers, G., Saunders, A. D., Storey, M., 1991. Relation between alkalic volcanism and slab-window formation. Geology 19 (6), 657-660.

Holland, T. J. B., Powell, R., 1998. An internally consistent thermodynamic data set for phases of petrological interest. Journal of Metamorphic Geology 16, 309-343.

Hyppolito, T., Juliani, C., Garcia-Casco, A., Meira, V., Bustamante, A., Hall, C., 2015. LP/HT metamorphism as a temporal marker of change of deformation style within the Late Palaeozoic accretionary wedge of central Chile. Journal of Metamorphic Geology 33 (9), 1003–1024.

Hyppolito, T., Cambeses, A., Angiboust, S., Raimondo, T., García-Casco, A., Juliani, C., 2018. Rehydration of eclogites and garnet-replacement processes during exhumation in the amphibolite facies. Geological Society, London, Special Publications 478, 217-239.

John, T., Scherer, E. E., Schenk, V., Herms P., Halama, R., Garbe-Schonberg, D., 2010. Subducted seamounts in an eclogite-facies ophiolite sequence: the Andean Raspas Complex, SW Ecuador. Contribution to Mineralogy and Petrology 159, 265-284.

Johnson, D.M.; Hooper, P.R.; Conrey, R.M., 1999. XRF analysis of rocks and minerals for major and trace elements on a single low dilution Li-tetraborate fused bead: JCPDS-International Centre for Diffraction Data, 843–867.

Keane, S.D., Dewolf, C.P., Essene, E.J., Halliday, A.N., Hall, C.M., Cosca, M.A., 2006. Isotopic constraints on the thermal history of the Wind River Range, Wyoming: implications for Archean metamorphism. Canadian Journal of Earth Sciences, 43, 1511-1532.

Kerr, A. C., Aspden, J. A., Tarney, J., Pilatasig, L. F., 2002a. The nature and provenance of accreted oceanic terranes in western Ecuador: geochemical and tectonic constraints. Journal of the Geological Society, London 159, 577-594.

Kerr, A. C., Tarney, J., Kempton, P. D., Spadea, P., Nivia, A., Marriner, G. F., Duncan, R. A., 2002b. Pervasive mantle plume head heterogeneity: Evidence from the late Cretaceous Caribbean-Colombian oceanic plateau. Journal of Geophysical Research 107, ECV 2-1-ECV 2-13.

Kerr, A. C., White, R. V., Saunders, A. D., 2000. LIP Reading: Recognizing Oceanic Plateaux in the Geological Record. Journal of Petrology 41, 1041-1056.

Lanari, P., 2020. An introduction to XMapTools. User guide, version 2020-6-10.

Lanari, P., Vidal, O., De Andrade, V., Dubacq, B., Lewin, E., Grosch, E., & Schwartz, S., 2014. XMapTools: a MATLAB©-based program for electron microprobe X-ray image processing and geothermobarometry. Computers and Geosciences, 62, 227-240.

Lanari, P., Vho, A., Bovay, T., Airaghi, L., & Centrella, S., 2019. Quantitative compositional mapping of mineral phases by electron probe micro-analyser. Geological Society of London, Special Publications 478, 39-63.

Liu, L. J., Gurnis, M., Seton, M., Saleeby, J., 2010. The role of oceanic plateau subduction in the Laramide orogeny. Nature Geosciences 3 (5), 353-357.

Liu, Z., Dai, L., Li, S., Wang, L., Xing, H., Liu, Y., Ma, F., Dong, H., Li, F., 2021. When plateau meets subduction zone: A review of numerical models. Earth-Science Reviews 215, 103556.

Marien, L. H., Pitra, P., Cagnard, F., Le Bayon, B., 2020. Prograde and retrograde P–T evolution of a Variscan high temperature eclogite, French Massif Central, Haut-Allier. BSGF - Earth Sciences Bulletin 191, 14.

Maruyama, S., Liou, J. G., Terabayashi, M., 1996. Blueschists and Eclogites of the World and Their Exhumation. International Geologic Review 38, 485-594.

Massonne, H. -J., Toulkeridis, T., 2012. Widespread relics of high-pressure metamorphism confirm major terrane accretion in Ecuador: a new example from the Northern Andes. International Geology Review 54, 67-80.

McDonough, W. F., Sun, S. -S., 1995. The composition of the Earth. Chemical Geology 120, 223-253.

Morimoto, N., 1988. Nomenclature of Pyroxenes. Mineralogy and Petrology 39, 55-76.

Phillips, G., Offler, R., 2011. Contrasting modes of eclogite and blueschist exhumation in a retreating subduction system: The Tasmanides, Australia. Gondwana Research 19, 800-811.

Platt, J. P., 1993. Exhumation of high-pressure rocks: a review of concepts and processes. Terra Nova 5, 119-133.

Ramos, V. A., 2009. Anatomy and global context of the Andes: main geologic features and the Andean orogenic cycle. The Geological Society of America Memoir 204, 31–65.

Riel, N., Martelat, J.-E., Guillot, S., Jaillard, E., Monié, P., Yuquilema, J., Duclaux, G., Mercier, J., 2014. Fore arc tectonothermal evolution of the El Oro metamorphic province (Ecuador) during the Mesozoic. Tectonics 33, 1989-2012.

Schellart, W. P., 2004. Quantifying the net slab pull force as a driving mechanism for plate tectonics. Geophysical Research Letters 31, L07611.

Sheng, Y. -M., Gong, B., 2017. Hydrous species in eclogitic omphacite: Implications for metamorphic dehydration during exhumation. Journal of Asian Earth Sciences, 145, 123-129.

Spear, F. S., Pattison, D. R. M., 2017. The implications of overstepping for metamorphic assemblage diagrams (MADs). Chemical Geology 457, 38-46.

Spear, F., 2017. Garnet growth after overstepping. Chemical Geology 466, 491-499.

Spikings, R. A., Cochrane, R. S., Villagomez, D., Van der Lelij, D., Vallejo, C., Winkler, W., Beate, B., 2015. The geological history of northwestern South America: from Pangaea to the early collision of the Caribbean large igneous province (290-75 Ma). Gondwana Research 27, 95–139.

Spikings, R. A., W. Winkler, R. A. Hughes, and R. Handler., 2005. Thermochronology of Allochthonous Terranes in Ecuador: Unraveling the accretionary and post-accretionary history of the Northern Andes, Tectonophysics 399, 195–220.

Streepey, M.A., van der Pluijm, B.A., Essene, E.J., Hall, C.M., Magloughlin, J.F., 2000. Late Proterozoic (ca. 930Ma) extension in eastern Laurentia. Geological Society of America Bulletin, 112, 1522-1530.

Stern, C. R., 2011. Subduction erosion: Rates, mechanisms, and its role in arc magmatism and the evolution of the continental crust and mantle. Gondwana Research 20 (2-3), 284-308.

Sun, S.-S., McDonough, W. F., 1989. Chemical and isotopic systematics of oceanic basalts: implications for mantle composition and processes. Geological Society, London 42, 313-345.

Tomkins, D. K., Powell, R., Ellis, D. J., 2007. The pressure dependence of the zirconium-in-rutile thermometer. Journal of Metamorphic Geology 25, 703-713.

Turcotte, D. L., Schubert, G., 2002.Geodynamics. Cambridge University Press, New York, NY, 456 pp

Valarezo, M. E., Vallejo, C., Horton, B. K., Gaibor, J., Esteban, J., Javkson, L. J., Carrasco, H., Winkler, W., Bernal, C., Beate, B., 2019. Sedimentological and provenance analysis of the Río Playas stratigraphic section: Implications for the evolution of the Alamor-Lancons Basin of southern Ecuador and northern Peru. Journal of South American Earth Sciences 94, 102239.

Vallejo, C. Spikings, R. A., Luzieux, L., Winkler, W. Chew, D., Page, L., 2006. The early interaction between the Caribbean Plateau and the NW South American Plate. Terra Nova 18, 264-269.

Vallejo, C., Spikings, R. A., Horton, B. K., Luzieux, L., Romero, C., Winkler, W., Thomsen, T. B., 2019. Chapter 8 - Late cretaceous to Miocene stratigraphy and provenance of the coastal forearc and Western Cordillera of Ecuador: Evidence for accretion of a single oceanic plateau fragment. Andean Tectonics, Elsevier 209-236 p.

Vallejo, C., Winkler, W., Sipikings, R. A., Luzieux, L., Heller, F., Bussy, F., 2009. Mode and timing of terrane accretion in the forearc of the Andes in Ecuador. The Geological Society of America Memoir 204, p.

Vogt, K., Gerya, T. V., 2014. From oceanic plateaus to allochthonous terranes: Numerical modelling. Gondwana Research 25, 494-508.

Wu, B., Conrad, C. P., Heuret, A., Lithgow-Bertelloni, C., Lallemand, S., 2008. Reconciling strong slab pull and weak plate bending: The plate motion constraint on the strength of mantle slabs. Earth and Planetary Science Letters 272, 412-421.

Xia, L., Li, X., 2019. Basalt geochemistry as a diagnostic indicator of tectonic setting. Gondwana Research 65, 43-67.

Yamasaki, T., 2018. Contamination from mortars and mills during laboratory crushing and pulverizing. Bulletin of the Geological Survey of Japan 69, 201-210.

Zack, T., Moraes, R., & Kronz, A., 2004. Temperature dependence of Zr in rutile: empirical calibration of a rutile thermometer. Contributions to Mineralogy and Petrology 148, 471-488.

Zapata, S., Cardona, A., Jaramillo, J. S., Patiño, A., Valencia, V., León, S., Mejía, D., Pardo-Trujillo, A., Castañeda, J. P., 2019. Cretaceous extensional and compressional tectonics in the Northwestern Andes, prior to the collision with the Caribbean oceanic plateau. Gondwana Research, 66, 207-226.

Zapata, S., Patiño, A., Cardona, A., Parra, M., Valencia, V., Reiners, P., Oboh-Ikuenobe, F., Genezini, F., 2020. Bedrock and detrital zircon thermochronology to unravel exhumation histories of accreted tectonic blocks: An example from the Western Colombian Andes. Journal of South American Earth Sciences, 103, 102715.

Zheng, Y. -F., Zhao, Z, -F., 2017. Introduction to the structures and processes of subduction zones. Journal of Asian Earth Sciences 145, 1-15.

Supplementary data

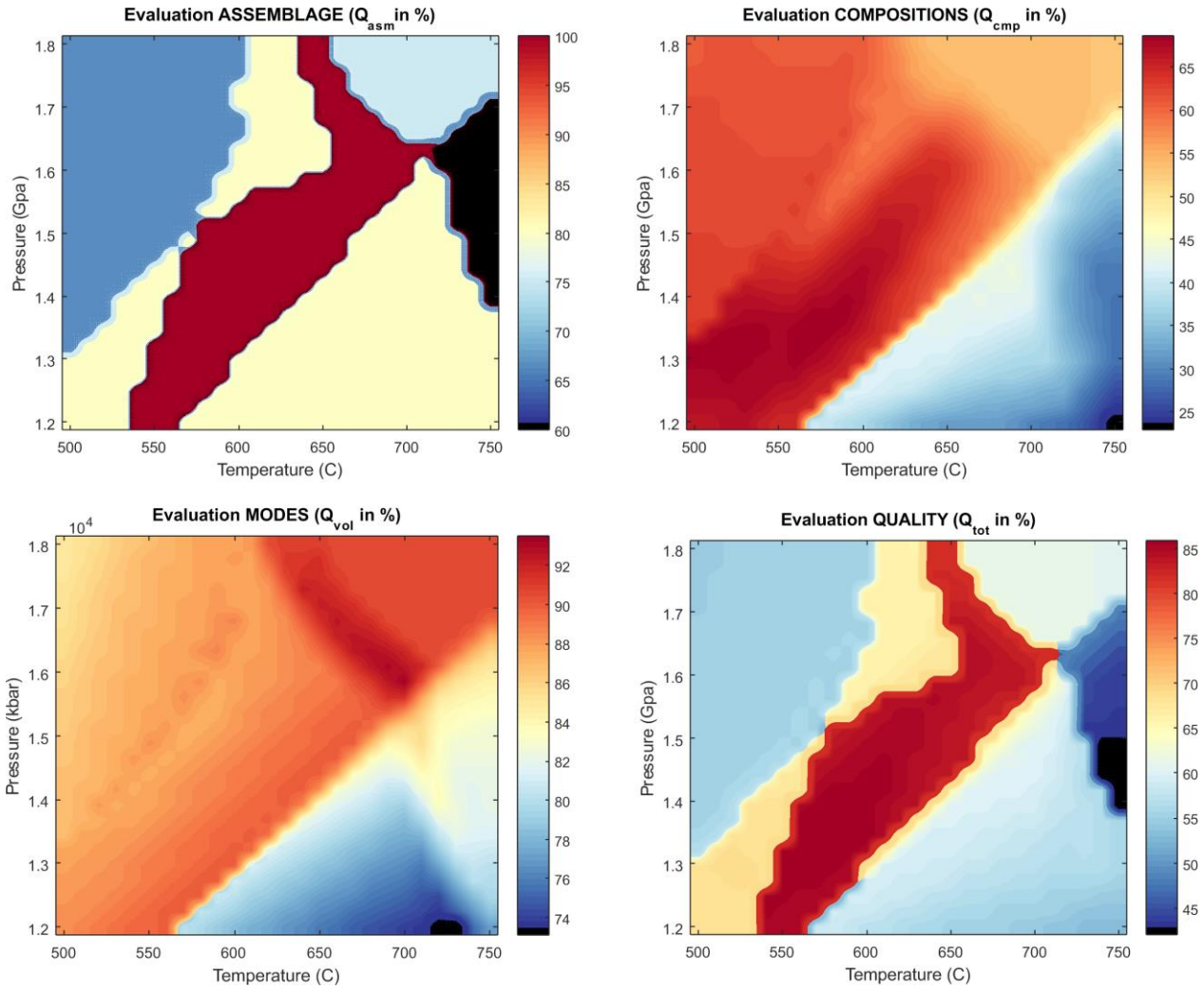

Figure A.1. Quality factors diagrams for the assemblage (Q_{asm}), composition (Q_{cmp}), volume of phases (Q_{vol}), and total (Q_{tot}) for the Stage I.

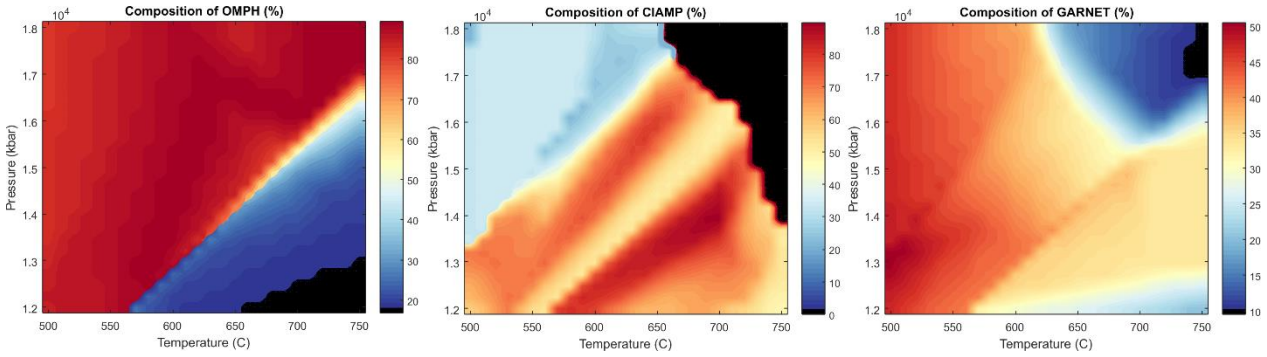

Figure A.2. Diagram for Q_{cmp} for amphibole (CLAMP), garnet and omphacite (OMPH) of the Stage I.

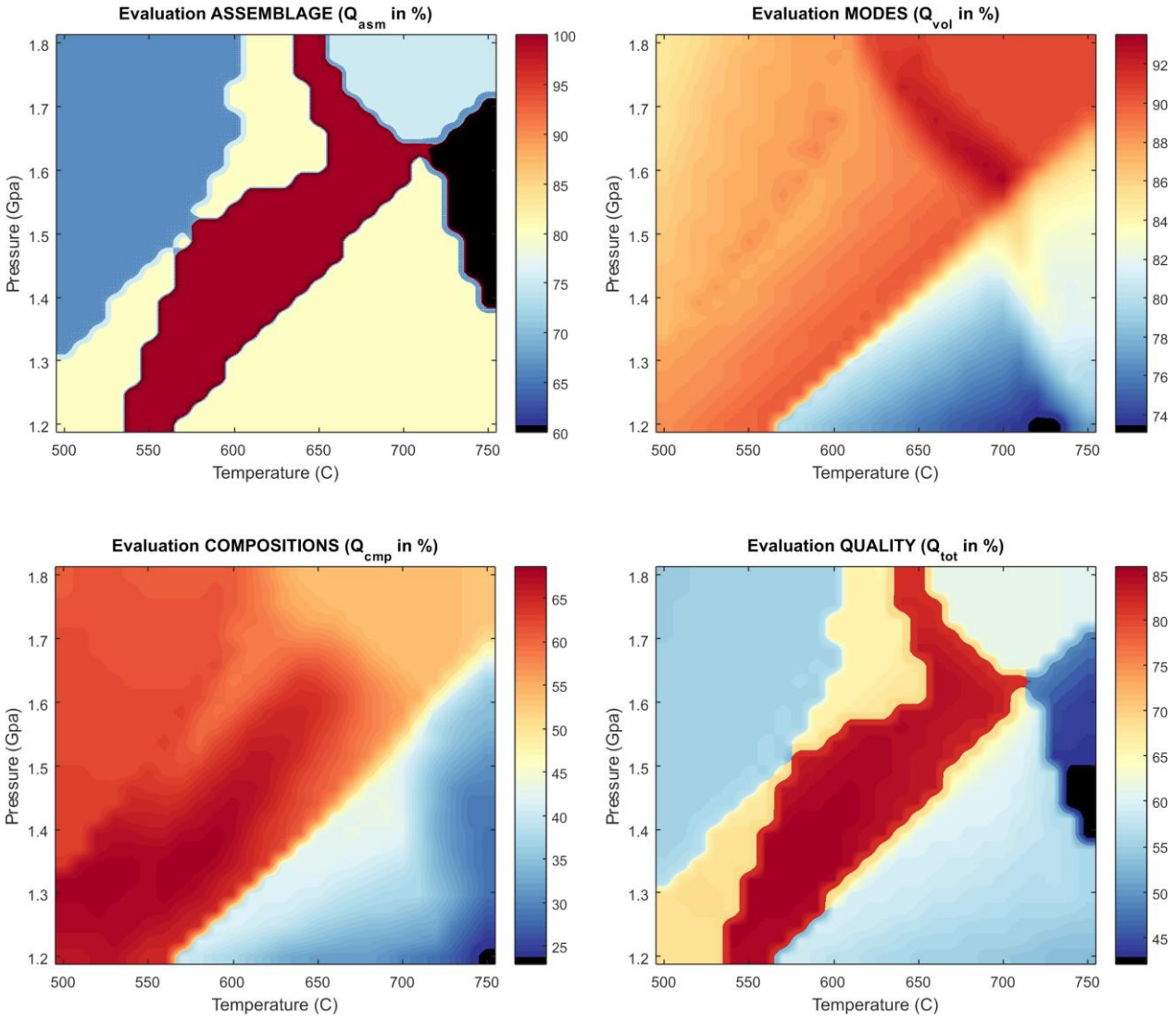

Figure A.3. Quality factors for the Stage II.

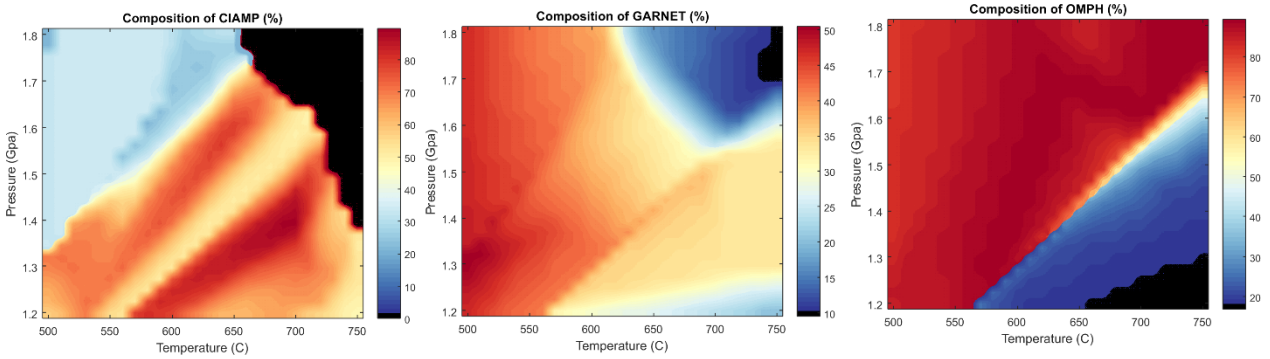

Figure A.4. Diagram for Q_{cmp} for amphibole, garnet and omphacite of the Stage II.

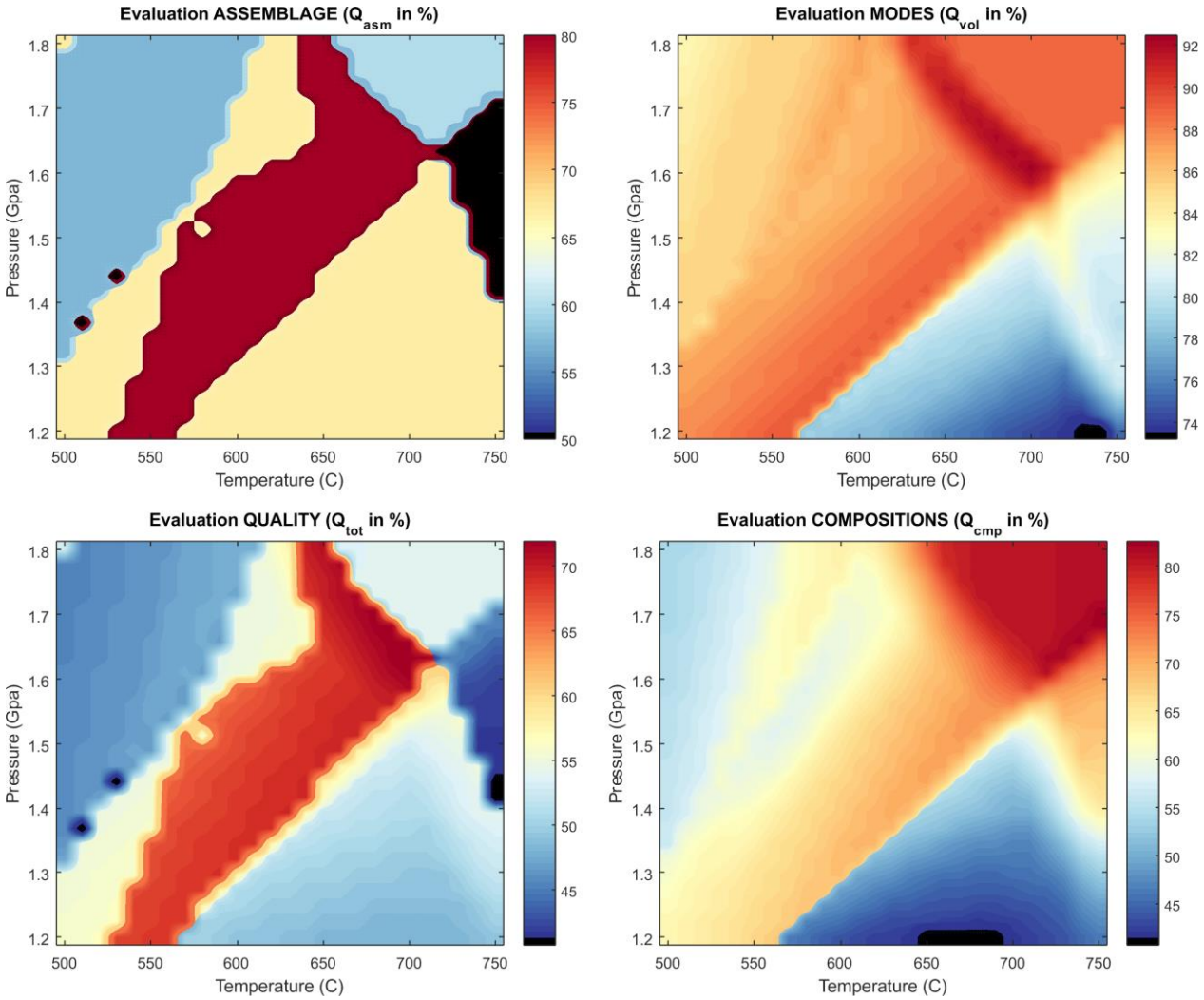

Figure A.5. Quality factors for the Stage III.

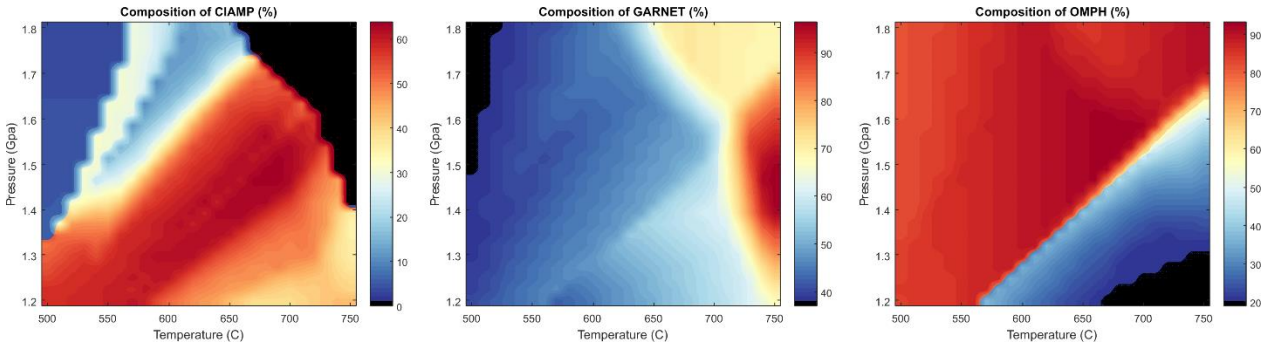

Figure A.6. Diagram for Q_{cmp} for amphibole, garnet and omphacite of the Stage II.

Table A.1. Geochemical database of oceanic plateau lavas from GEOROC.

Table A.2. All mineral analysis of garnet, epidote and omphacite.

5.2 Artigo 2: Metamorphic evolution of blueschists from the Raspas Metamorphic Complex, Ecuador unraveling the subduction of oceanic plateaus

Nesse artigo investigamos a evolução metamórfica dos xistos azuis presentes no Complexo Metamórfico Raspas. A partir de sua trajetória comparamo-la ao seu equivalente eclogítico para debater os estágios iniciais da subducção do Platô Raspas. Submetido ao Geological Journal em 11 de novembro de 2022. Situação atual, sob revisão.

Metamorphic evolution of blueschists from the Raspas Metamorphic Complex, Ecuador: unraveling the subduction of oceanic plateaus

Salviano da Silva[* a, b], Andres Bustamante[b], Carla Joana Santos Barreto[b]

[a]Universidade Federal de Pernambuco, Departamento de Geologia, Programa de Pós-Graduação em Geociências, Av. da Arquitetura, s/nº, CEP 50740-550, Recife, PE, Brazil.

[b]Departamento de Geologia, Universidade Federal de Pernambuco, Av. da Arquitetura s/nº, CEP 50740-550, Recife, PE, Brazil

[*]Corresponding author.

E-mail: salviano_pereira@hotmail.com (S. da Silva)

ABSTRACT

We know most oceanic plateaus from accreted fragments on active margins. Moreover, even though mathematic models indicate that these features can be subducted, our knowledge about the metamorphic signature of their subduction still needs to be improved. During Early Cretaceous occurred, a high pressure (HP) event along the Northern Andes, whose onset is marked by the formation of the HP ophiolite Raspas Metamorphic Complex. This complex is represented by blueschists and eclogites associated with metaultramafic rocks. Previous works suggested a protolith signature akin to an oceanic plateau. In this work, we present mineral analysis and thermodynamic modeling of the blueschists from this complex to unravel the metamorphic response during the subduction of oceanic plateaus. The onset of HP metamorphism marks the collision of the oceanic plateau by an S_1 foliation dominated by epidote/clinozoisite + paragonite/phengite + winchite $_{(low\ Na)}$ + quartz formed around 490 °C/1.15 GPa, followed by an isothermal compression during growth of winchite$_{(high\ Na)}$ + garnet$_{(Alm0.49\text{-}0.61,\ Grs0.23\text{-}0.32,\ Py0.05\text{-}0.07,\ Sps0.17\text{-}0.07)}$ + phengite + zoisite + quartz ± chlorite coeval to S_2 development at 523 °C/1.68 GPa. Peak metamorphic conditions were attained after a small decompression during the early stages of rollback at 570-590 °C/1.4-1.7 GPa as omphacite and phengite porphyroblasts growth. The exhumation had onset by thinning the plateau before breaking off at 550 °C/1.25 GPa registered by Fe-barroisite around garnet. The breakoff culminated in an isothermal decompression during chlorite + albite + pargasite + Mg-hornblende formation at 450-550 °C/ < 0.6 GPa. Moreover, the metamorphic conditions obtained are consistent at ~100 °C cooler than previous constraints for their eclogitic equivalent. We interpret this as caused by thermal zoning on the plateau interior due to their thickness.

Keywords: Oceanic plateau, blueschists, slab rollback, slab breakoff, Andean Orogeny, Raspas Metamorphic Complex

INTRODUCTION

Blueschists and eclogites are one of the most prominent features of subduction zones. Their formation is enabled when cold oceanic material is put under high pressure (HP) conditions at great depths depressing the mantle isotherms. Although vast amounts of oceanic material are consumed during subduction, only a small amount returns due to exhumation to shallow portions of the crust. Thus, it is more accessible for our study (Brun and Faccenna, 2008). Moreover, the extreme conditions where their assemblages are formed means that they are susceptible to changes in temperature and pressure during exhumation (Whitney and Davis, 2006), thus the preservation of blueschists and eclogites depends on a frail balance of fast exhumation rates (Agard et al., 2009) and the absence of posterior metamorphic events (Kydonakis et al., 2015).

When the HP assemblages are preserved, metamorphic studies on the P-T conditions attained by these rocks give primal information about tectonic and petrologic aspects that occurred during subduction. During their path to great depths, the mineralogical transformations are sensible to temperature, better represented by the transition between blueschist to eclogite facies (e.g., Peacock, 1993; Ridley, 1984). This transition releases a significant amount of water to the mantle, responsible for the formation of arc magmatism (Kerrick and Connolly, 2001). Moreover, the P-T path taken during subduction reveals the thermal structure of subduction (e.g., Ota and Kaneko, 2010), if had changes in the angle of subduction (Zhang et al., 2017), and the mechanisms responsible for exhumation (e.g., Maruyama et al., 1996).

The Cretaceous is characterized by a significant volume of plume activity during the formation of oceanic plateaus, especially in the Pacific realm. Numeric models show that even though they are thicker than a typical oceanic crust, under favorable conditions, they can subduct (Liu et al., 2021 and references within). However, the only documented occurrence of HP rocks

originating from an oceanic plateau protolith is in the Gorny Altai region (Ota et al., 2007). Nevertheless, the eclogites of this region were dismembered when the plateau collided with the orogen and later incorporated as small lenses embedded into a mélange (Ota et al., 2007).

The Andean orogeny has a vast record of accretion of oceanic plateau fragments in the Late Cretaceous to Paleogene times (e.g., Kerr et al., 1997). They were the result of the collision of the Caribbean Plateau into the South American margin. However, an older and less know fragment of the oceanic plateau is represented by eclogites and blueschists with oceanic plateau affinity of the Raspas Metamorphic Complex (Arculus et al., 1999; Bosh et al., 2002; da Silva et al., 2022). HP metamorphism occurred at 133 Ma (John et al., 2010). The metamorphic data for the eclogites reveal an isobaric heating between 1.65 and 650-700°C during a rollback and before a slab breakoff (da Silva et al., 2022). However, this complex still lacks metamorphic constraints for the blueschists, which is crucial to unravel the early stages of subduction of the oceanic plateau.

This contribution presents mineral analysis and thermodynamic modeling to constrain the metamorphic evolution of blueschists from the Raspas Metamorphic Complex. Moreover, we compare their P-T path with their eclogite counterpart to debate the subduction of oceanic plateaus in light of the metamorphic path taken by these rocks.

GEOLOGICAL SETTING

The Northern Andes

The regional framework of the northern portion of the Andean orogeny is marked by the evolution of a long-lived subduction (>200 Ma), which history is registered in the eastern, central and western mountain ranges (Spikings et al., 2015).

The Eastern Cordillera marks the onset of subduction during the Jurassic, reflected by an extensive arc magmatism (Bustamante et al., 2016) that evolved to form a back-arc (Fig. 1; Villagómez et al., 2011). By the end of Jurassic, during the break-up of Gondwana, the Andean margin transitioned from an extensional regime to a contractional one, causing the back arc's closure (Spikings et al., 2015). The latter was followed, in the Early Cretaceous, by the formation of an HP belt represented by discontinuous occurrences of blueschists and eclogites that extends from Colombia to Ecuador (Avellaneda-Jimenez et al., 2021; Bustamante et al., 2012; da Silva et al., 2022; Figure 1) along the Central Cordillera. Finally, at the end of the Cretaceous, the South American margin interacted with the Caribbean Plateau resulting in several fragments accreted to the continental margin (Fig. 1; Kerr et al., 1997; Mamberti et al., 2003; Vallejo et al., 2009; Zapata-Villada et al., 2017). This accretionary event is also marked by the formation and accretion of intraoceanic arcs (Fig. 1; Bustamante et al., 2021), some of which developed above the Caribbean Plateau (Bustamante and Bustamante, 2019; Zapata-Villada et al., 2021), and an occurrence of blueschist in the Jambaló region, Colombia (Bustamante et al., 2021).

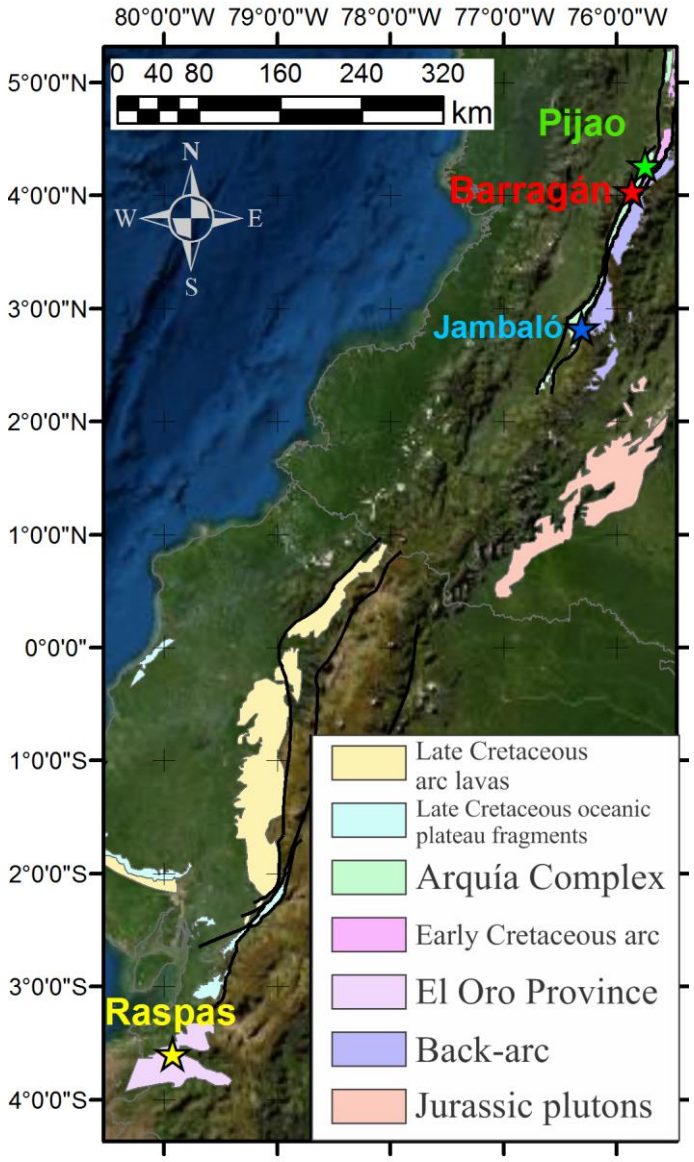

Figure 1 Simplified map of the Northern Andes at the segment between Ecuador and Colombia. The stars refer to the location of the Cretaceous HP occurrences on the Northern Andes.

Cretaceous HP events along the Northern Andes

Bustamante and Bustamante (2019) reviewed the main HP occurrences along the northern Andes, proposing two major events, the first at 133-120 Ma and the second around 65 Ma.

The first HP event is registered along the flanks of the Central Cordillera as discontinuous occurrences in a region that extends from Colombia to Ecuador (Fig. 1). The oldest of these occurrences is the Raspas Metamorphic Complex which will be described in the following section. The other HP rocks are present in Colombia, more precisely in the Arquía Complex at the Pijao and Barragán regions.

The Arquía Complex encompasses amphibolites, garnet amphibolites, micaschists, and serpentinites with minor eclogites and blueschists, all with MORB signature. The HP rocks from the Pijao Metamorphic Complex (after Avellaneda-Jimenez et al., 2021) occur as centimetric- to metric-sized lenses enclosed in garnet amphibolites. The eclogitic assemblage garnet + white mica + omphacite + amphibole + lawsonite + quartz reach P-T conditions around 1.8-2.4 GPa and 465-580 °C at ca. 129 Ma (García-Ramírez et al., 2017) followed by cooling ages of 115-110 Ma (McCourt et al., 1984; Toussaint and Restrepo, 1994)

The HP rocks from Barragán are usually associated with metapelites, ultramafic, garnet amphibolites (retroeclogites), and greenschists, with typic MORB signature (Bustamante et al., 2012). The blueschists of the Barragán region characterizes especially by the presence of chlorite-lawsonite schists bands intercalated with epidote-glaucophane schists. Metamorphic constraints are still lacking, although conventional thermobarometry indicates eclogite-facies conditions preserved for the garnet amphibolites around 640 °C and 1.5 GPa, whereas the blueschists are around 400 °C and 1.0 GPa (Bustamante, 2008). Ar/Ar age constraints display cooling ages around 120 Ma (Bustamante et al., 2012).

The Jambaló blueschists are found to be associated with marbles, metamarls, quartzites, keratophyres, and serpentinites, all of them occurring as lenses embedded in the main greenschist unit (Bustamante et al., 2021). Available metamorphic constraints suggest that the HP assemblage

garnet + paragonite + albite + glaucophane attained conditions between 1.3-1.6 GPa and 450-530 °C. Ar-Ar ages indicate that the HP event occurred in the Late Cretaceous (~ 65 Ma; Bustamante et al., 2012). Their origin has been attributed to a suprasubduction environment during the interaction between the Caribbean Plateau with the Andean margin (Bustamante et al., 2020).

The Raspas Metamorphic Complex

The HP occurrence focus of this work is located in the El Oro Province, the southern portion of Ecuador. This region is marked by several Triassic to Cretaceous units with continental and oceanic affinities. They are bounded by E-W transcurrent shear zones or faults, contrasting with the general N-S major structures from the Northern Andes. It is believed that the El Oro Province is part of the Real Cordillera of Ecuador, although the continuation is covered by Tertiary to Quaternary sediments (Aspden et al., 1995).

The Raspas Metamorphic Complex is juxtaposed with metapelites to migmatitic paragneisses from the Birón terrane by the La Palma-El Guayabo shear zone in the north. Whereas in the south is limited by a major tectonic contact with the Triassic (225 Ma; Gabrieli, 2002) blueschists and greenschists metabasites from the Arenillas-Panupali Unit.

This complex can be subdivided into the El Toro and Raspas units. The El Toro Unit comprises metaperidotites and ultramafic rocks with variable degrees of serpentinization. The Raspas Unit is made up of eclogites, blueschists and HP metapelites. The best exposures are found along the Raspas River as pebbles and boulders, up to decametric scale, dominated by dark green eclogites frequently intercalated with metapelites and in minor proportion blueschists (Aspden et al., 1995; Gabriele, 2002). Metamorphic constraints for the eclogites suggest that the assemblage garnet + katophorite + zoisite + omphacite + quartz was formed around 700 °C and 1.7 GPa (da

Silva et al., 2022) at 133 Ma (John et al., 2010) during the subduction of an oceanic plateau (Arculus et al., 1999; Bosh et al., 2002; da Silva et al., 2022).

METHODS

Mineral analysis and compositional maps were obtained in an Electron Microprobe Analyzer JEOL JXA-8230 at the Regional Center for Technological Development and Innovation from the Federal University of Goiás, Brazil. Chemical maps were obtained via wavelength-dispersive spectroscopy with conditions set at 15 kV, beam current of 100 nA, a focused beam with 8 µm of size, counting time of 60 ms/pixel, and later processed using the program XMapTools (version 4.0; Lanari et al., 2014; Lanari, 2020). Mineral spot analysis (Table 1-6) on glaucophane, albite, phengite, paragonite, epidote, and garnet was performed with a beam current of ~20 nA, accelerating voltage of 15 kV and counting time dependable of the element. Analytical error is between ± 0.01-0.21 wt% (1σ), and detection limits vary from ± 0.01 to 0.11 wt%. The calibration standards utilized were "jadeite" for Na, "Al_2O_3" for Al, "celsian" for Ba, "olivine" for Mg, "olivine P-140" for Ni, "Fe_3O_4" for Fe "A-128 ilmenite" Ti, "orthoclase" for K, "rhodonite" for Mn, "GS-3" for Cr, "diopside" for Ca, and "Enstatite Al 5" for Si.

To understand the phase relationship and their corresponding P-T, we performed pseudosections in Na_2O-CaO-FeO-MgO-Al_2O_3-SiO_2-H_2O (NCFMASH) and Na_2O-CaO-K_2O-FeO-MgO-Al_2O_3-SiO_2-H_2O (NCKFMASH) chemical systems with and without an excess of oxygen. For that, we used the program THERIAK-DOMINO (version 11.03.2020; de Capitani & Brown, 1987; de Capitani & Petrakakis, 2010) with the internally consistent thermodynamic database of Holland and Powell (1998) version 3.30. Mineral solution data from feldspar are from Holland and Powell (2003), omphacite is from Green et al. (2007), chlorite from Holland et al.

(1998), amphibole is from Diener and Powell (2011), and garnet, white mica, and epidote are from Holland and Powell (1998). All pseudosections were made considering a P-T window between 350-600°C and 0.5-1.8 GPa that could be a good representation of assemblages at blueschist facies conditions and part of the retrograde path.

Table 1 Electron Microprobe analysis (EMPA) of garnet from the analyzed blueschist.

Mineral	Garnet	Garnet	Garnet	Garnet	Garnet	Garnet	Garnet	Garnet	Garnet
Point	288	289	290	291	292	293	294	295	296
SiO2	38.75	38.80	38.09	38.49	38.12	38.20	38.12	38.21	37.96
TiO2	0.12	0.09	0.09	0.11	0.13	0.10	0.13	0.17	0.13
Al2O3	20.88	21.16	21.04	21.03	20.85	20.94	21.01	20.87	20.92
Cr2O3	0.01	0.01	0.02	0.01	0.01	0.02	0.01	0.02	0.03
Fe2O3	0.17	0.08	1.05	0.07	0.19	0.00	0.00	0.04	1.04
FeO	28.13	28.71	27.90	28.90	28.00	27.28	26.36	26.59	23.09
MnO	0.63	0.80	0.88	1.28	1.99	2.57	3.39	3.57	5.08
MgO	2.66	2.50	2.48	2.28	2.08	1.93	1.68	1.74	1.53
CaO	8.43	8.41	9.87	8.02	8.24	8.48	8.81	8.48	11.45
Na2O	0.02	0.04	0.03	0.01	0.03	0.01	0.01	0.01	0.02
Total	99.80	100.60	101.45	100.21	99.65	99.54	99.53	99.71	101.24
Si	6.266	6.208	5.951	6.196	6.166	6.194	6.183	6.201	5.963
Ti	0.015	0.011	0.010	0.014	0.016	0.012	0.016	0.021	0.016
Al	3.979	3.990	3.875	3.989	3.975	4.002	4.017	3.992	3.873
Cr	0.001	0.001	0.002	0.002	0.002	0.002	0.001	0.002	0.004
Fe3	0.020	0.009	0.123	0.009	0.023	0.000	0.000	0.005	0.123
Fe2	3.804	3.841	3.645	3.891	3.788	3.699	3.576	3.608	3.034
Mg	0.642	0.597	0.578	0.548	0.502	0.467	0.406	0.422	0.359
Ca	1.460	1.441	1.652	1.383	1.428	1.473	1.531	1.474	1.927
Mn	0.087	0.109	0.117	0.175	0.272	0.353	0.466	0.491	0.675
Na	0.006	0.012	0.008	0.003	0.009	0.005	0.002	0.004	0.005
grossular	0.243	0.240	0.275	0.231	0.238	0.246	0.256	0.246	0.321
pyrope	0.107	0.099	0.096	0.091	0.084	0.078	0.068	0.070	0.060
almandine	0.634	0.640	0.608	0.649	0.631	0.617	0.598	0.601	0.506
spessartine	0.014	0.018	0.019	0.029	0.045	0.059	0.078	0.082	0.113
xAl	0.995	0.997	0.969	0.997	0.994	0.999	1.000	0.998	0.968

Table 1 cont.

Mineral	Garnet	Garnet	Garnet	Garnet	Garnet	Garnet	Garnet	Garnet	Garnet
Point	297	298	299	300	301	302	304	305	306

SiO2	37.90	38.08	38.31	38.21	38.11	38.51	38.32	38.17	38.21
TiO2	0.13	0.08	0.59	0.08	0.14	0.16	0.10	0.12	0.11
Al2O3	20.94	20.96	20.35	20.98	20.85	20.60	20.86	20.84	21.04
Cr2O3	0.01	0.01	0.02	0.01	0.01	0.03	0.00	0.03	0.00
Fe2O3	0.84	0.83	0.36	0.05	1.13	0.27	0.03	1.00	0.00
FeO	22.85	22.74	21.58	24.40	22.59	23.75	26.01	25.62	27.32
MnO	6.24	6.80	7.31	6.31	6.13	5.88	4.54	3.42	3.49
MgO	1.34	1.35	1.22	1.81	1.31	1.36	1.68	1.71	1.95
CaO	10.80	10.48	9.60	8.07	11.30	9.23	8.22	10.40	7.71
Na2O	0.01	0.00	0.03	0.04	0.01	0.00	0.01	0.00	0.01
Total	101.06	101.34	99.38	99.94	101.58	99.80	99.77	101.30	99.84
Si	5.987	6.011	6.313	6.171	5.994	6.286	6.227	6.025	6.183
Ti	0.015	0.010	0.074	0.009	0.017	0.020	0.012	0.014	0.013
Al	3.899	3.900	3.953	3.993	3.865	3.963	3.996	3.878	4.013
Cr	0.001	0.002	0.002	0.001	0.002	0.004	0.000	0.003	0.000
Fe3	0.100	0.099	0.045	0.006	0.134	0.033	0.004	0.119	0.000
Fe2	3.018	3.001	2.975	3.295	2.971	3.242	3.535	3.382	3.697
Mg	0.317	0.317	0.300	0.435	0.306	0.331	0.407	0.402	0.471
Ca	1.828	1.772	1.695	1.396	1.905	1.614	1.430	1.759	1.337
Mn	0.835	0.910	1.021	0.863	0.816	0.813	0.625	0.458	0.478
Na	0.002	0.000	0.010	0.011	0.002	0.000	0.003	0.000	0.003
grossular	0.305	0.295	0.283	0.233	0.317	0.269	0.238	0.293	0.223
pyrope	0.053	0.053	0.050	0.072	0.051	0.055	0.068	0.067	0.079
almandine	0.503	0.500	0.496	0.549	0.495	0.540	0.589	0.564	0.618
spessartine	0.139	0.152	0.170	0.144	0.136	0.136	0.104	0.076	0.080
xAl	0.975	0.975	0.988	0.998	0.966	0.991	0.999	0.969	1.000

Table 1 cont.

Mineral	Garnet	Garnet	Garnet	Garnet	Garnet
Point	308	309	310	311	312
SiO2	38.35	38.10	38.29	38.31	38.29
TiO2	0.12	0.04	0.12	0.08	0.05
Al2O3	20.69	21.12	21.16	20.81	21.32
Cr2O3	0.01	0.04	0.03	0.03	0.04
Fe2O3	0.22	0.76	1.07	0.17	0.83
FeO	27.99	28.41	26.11	27.29	26.72
MnO	1.91	1.03	0.67	0.57	0.55
MgO	2.13	2.69	2.50	2.65	3.23
CaO	8.06	8.96	11.65	9.08	10.28
Na2O	0.00	0.00	0.03	0.02	0.02
Total	99.48	101.14	101.63	99.01	101.33

Si	6.245	5.978	5.942	6.209	5.940
Ti	0.014	0.005	0.014	0.010	0.006
Al	3.971	3.905	3.871	3.976	3.898
Cr	0.002	0.005	0.004	0.003	0.005
Fe3	0.027	0.089	0.125	0.021	0.097
Fe2	3.812	3.728	3.389	3.700	3.466
Mg	0.517	0.629	0.578	0.640	0.747
Ca	1.406	1.506	1.937	1.577	1.708
Mn	0.264	0.136	0.088	0.078	0.072
Na	0.001	0.000	0.008	0.006	0.006
grossular	0.234	0.251	0.323	0.263	0.285
pyrope	0.086	0.105	0.096	0.107	0.124
almandine	0.635	0.621	0.565	0.617	0.578
spessartine	0.044	0.023	0.015	0.013	0.012
xAl	0.993	0.976	0.968	0.994	0.974

Table 2 EMPA analysis of amphibole. Classification after Hawthorne et al., 2012.

Point	251	254	268	270	271	278	283	285	286	287	313
SiO2	52.88	55.58	50.58	52.08	51.96	56.67	51.73	51.16	52.12	50.25	42.48
TiO2	0.10	0.05	0.09	0.07	0.13	0.04	0.12	0.10	0.12	0.11	1.44
Al2O3	11.01	2.02	9.57	9.27	10.55	10.73	10.10	7.71	10.04	6.28	16.21
Cr2O3	0.03	0.00	0.03	0.03	0.01	0.02	0.01	0.00	0.02	0.03	0.23
MnO	0.10	0.07	0.10	0.11	0.08	0.01	0.05	0.11	0.08	0.13	0.09
FeO	11.83	11.24	12.87	13.38	12.27	5.19	10.76	12.52	11.47	12.78	17.83
MgO	11.62	16.75	12.11	11.22	12.24	8.16	12.40	12.93	11.74	12.36	7.36
CaO	5.83	11.80	7.97	6.41	7.61	13.56	6.44	8.34	6.18	8.28	8.20
Na2O	3.43	0.92	2.75	3.42	3.68	6.37	3.59	2.33	3.61	1.77	3.17
K2O	0.22	0.04	0.20	0.13	0.23	0.03	0.21	0.16	0.19	0.26	0.60
Total	97.06	98.4709	96.27	96.12	98.79	100.88	95.56	95.36	95.6	92.27	97.61
Si	7.480	7.835	7.293	7.502	7.288	7.680	7.412	7.445	7.483	7.602	6.290
Al	0.520	0.165	0.707	0.498	0.712	0.320	0.588	0.555	0.517	0.398	1.700
Ti	---	---	---	---	---	---	---	---	---	---	---
Fe3+	---	---	---	---	---	---	---	---	---	---	---
∑T	8.000	8.000	8.000	8.000	8.000	8.000	8.000	8.000	8.000	8.000	8.000
Ti	0.011	0.005	0.010	0.008	0.014	0.004	0.013	0.011	0.013	0.013	0.160
Al	1.315	0.170	0.919	1.076	1.032	1.394	1.118	0.767	1.181	0.722	1.120
Cr	0.003	---	0.003	0.003	0.001	0.002	0.001	---	0.002	0.004	0.020
Mn3+	---	---	---	---	---	---	---	---	---	---	---

Fe3+	0.049	0.103	0.300	0.202	0.205	---	0.242	0.237	0.168	0.070	0.280
Mn2+	---	---	---	---	---	0.001	---	---	---	---	---
Fe2+	1.170	1.202	1.165	1.302	1.185	0.588	0.960	1.180	1.120	1.402	1.780
Mg	2.450	3.520	2.603	2.409	2.559	1.649	2.649	2.805	2.513	2.788	1.620
∑C	4.999	5.000	5.000	5.000	4.999	3.649	5.000	5.000	5.000	5.001	5.000
Mn2+	0.012	0.008	0.012	0.013	0.010	---	0.006	0.014	0.010	0.017	0.010
Fe2+	0.180	0.021	0.087	0.108	0.049	---	0.088	0.107	0.090	0.145	0.150
Mg	---	---	---	---	---	---	---	---	---	---	---
Ca	0.884	1.782	1.231	0.989	1.144	1.969	0.989	1.300	0.951	1.342	1.300
Na	0.925	0.189	0.670	0.889	0.798	0.031	0.918	0.579	0.950	0.496	0.530
∑B	2.001	2.000	2.000	1.999	2.001	2.000	2.001	2.000	2.001	2.000	2.000
Ca	---	---	---	---	---	---	---	---	---	---	---
Na	0.016	0.063	0.099	0.066	0.203	1.643	0.080	0.078	0.055	0.023	0.370
K	0.040	0.007	0.037	0.024	0.041	0.005	0.038	0.030	0.035	0.050	0.110
∑A	0.056	0.070	0.136	0.090	0.244	1.648	0.118	0.108	0.090	0.073	0.480
∑CAT	15.056	15.070	15.136	15.089	15.244	15.297	15.119	15.108	15.091	15.074	15.480

Table 3 EMPA analysis of epidote calculated with basis of 12.5 oxygen per formulae.

Point	238	240	245	246	250	252	253	262	282
SiO2	39.46	39.01	39.12	38.65	37.94	39.16	39.43	39.51	39.11
TiO2	0.09	0.14	0.06	0.09	0.06	0.06	0.09	0.08	0.09
Al2O3	27.24	26.55	27.26	24.56	24.15	26.27	27.10	27.65	27.12
Cr2O3	0.05	0.04	0.03	0.05	0.05	0.11	0.03	0.05	0.02
Fe2O3	7.90	8.73	8.21	11.73	12.77	9.58	8.38	8.00	7.86
Mn2O3	0.24	0.31	0.27	0.17	0.16	0.19	0.31	0.22	0.03
MgO	0.02	0.05	0.00	0.03	0.00	0.01	0.05	0.01	0.09
CaO	21.01	20.71	20.98	24.50	24.41	24.51	20.65	24.88	20.57
Na2O	0.01	0.00	0.00	0.00	0.00	0.01	0.00	0.00	0.03
Total	97.92	97.44	97.84	101.71	101.46	101.85	97.95	102.37	96.80
Si	3.102	3.092	3.083	3.007	2.974	3.016	3.101	3.011	3.105
Ti	0.005	0.009	0.004	0.005	0.004	0.004	0.005	0.005	0.005
Al	2.524	2.480	2.532	2.252	2.231	2.384	2.512	2.483	2.538
Cr	0.003	0.002	0.002	0.003	0.003	0.007	0.002	0.003	0.001
Fe3	0.468	0.521	0.487	0.687	0.753	0.555	0.496	0.459	0.470
Mn3	0.014	0.019	0.016	0.010	0.010	0.011	0.019	0.013	0.002
Mg	0.002	0.006	0.000	0.003	0.000	0.001	0.005	0.002	0.011
Ca	1.770	1.759	1.771	2.043	2.050	2.023	1.740	2.031	1.750

Na	0.001	0.000	0.000	0.000	0.000	0.001	0.000	0.000	0.005
Fe3/(Fe3+Al)	0.156	0.174	0.161	0.234	0.252	0.189	0.165	0.156	0.156

Table 4 EMPA analysis of feldspars from sample 166.

Point	239	247	266	267	269	277	279	280
SiO2	73.79	72.38	68.44	72.38	69.77	70.09	69.88	67.69
TiO2	0.01	0.00	0.00	0.00	0.00	0.01	0.00	0.03
Al2O3	20.66	20.31	20.00	20.83	19.25	19.93	19.82	19.01
Cr2O3	0.00	0.01	0.00	0.00	0.00	0.01	0.00	0.00
Fe2O3	0.27	0.33	0.30	0.25	0.38	0.11	0.27	0.84
Mn2O3	0.00	0.01	0.00	0.00	0.00	0.03	0.00	0.00
MgO	0.00	0.00	0.00	0.00	0.36	0.01	0.00	0.03
CaO	0.13	0.15	0.60	0.56	0.44	0.09	0.26	0.24
Na2O	7.29	10.90	10.54	9.38	10.55	10.66	10.53	9.09
K2O	0.03	0.02	0.02	0.01	0.03	0.01	0.02	0.07
BaO	0.02	0.01	0.01	0.00	0.02	0.02	0.01	0.02
Total	102.21	104.11	99.91	103.42	100.81	100.97	100.80	97.02
Si	3.080	3.019	2.984	3.022	3.013	3.014	3.012	3.023
Al	1.016	0.999	1.028	1.025	0.980	1.010	1.007	1.001
Fe3	0.009	0.010	0.010	0.008	0.012	0.004	0.009	0.028
Mn3	0.000	0.000	0.000	0.000	0.000	0.001	0.000	0.000
Cr	0.000	0.000	0.000	0.000	0.000	0.000	0.000	0.000
Ti	0.000	0.000	0.000	0.000	0.000	0.000	0.000	0.001
Ba	0.000	0.000	0.000	0.000	0.000	0.000	0.000	0.000
Ca	0.006	0.006	0.028	0.025	0.021	0.004	0.012	0.011
Na	0.590	0.882	0.891	0.759	0.884	0.889	0.880	0.787
K	0.002	0.001	0.001	0.001	0.001	0.000	0.001	0.004
An	0.011	0.007	0.030	0.032	0.023	0.005	0.014	0.015
Ab	0.987	0.992	0.968	0.967	0.975	0.995	0.985	0.980
Kfs	0.003	0.001	0.001	0.001	0.002	0.001	0.001	0.005

Table 5 EMPA analysis of phengitic white mica from sample 166.

Point	241	242	243	255	260	264	272	273	281	284
SiO2	71.61	69.18	71.83	53.24	55.50	55.19	54.17	54.38	53.63	53.22
TiO2	0.03	0.03	0.03	0.19	0.24	0.25	0.25	0.24	0.32	0.24
Al2O3	19.97	19.14	19.94	28.84	30.07	29.86	30.15	30.02	29.90	29.66
FeO	0.22	0.32	0.24	2.46	2.44	2.31	2.20	2.16	2.19	2.24
MnO	0.01	0.00	0.00	0.00	0.01	0.00	0.00	0.00	0.00	0.01
MgO	0.00	0.00	0.00	3.20	3.20	3.29	3.12	3.10	3.08	3.24
CaO	0.00	0.01	0.01	0.04	0.00	0.02	0.00	0.01	0.00	0.05
Na2O	0.28	0.27	0.23	0.56	0.38	0.75	0.47	0.62	0.61	0.61
K2O	7.48	8.14	6.60	5.05	4.30	4.65	3.58	4.51	4.12	6.85
Total	99.60	97.10	98.89	93.59	96.16	96.30	93.93	95.04	93.86	96.12
Si	4.285	4.276	4.304	3.477	3.499	3.486	3.480	3.475	3.465	3.424
Ti	0.001	0.001	0.001	0.009	0.011	0.012	0.012	0.012	0.016	0.012
Al	1.408	1.394	1.408	2.220	2.234	2.223	2.283	2.261	2.276	2.249
Fe+3	0.000	0.000	0.000	0.000	0.000	0.000	0.000	0.000	0.000	0.000
Fe+2	0.011	0.017	0.012	0.134	0.129	0.122	0.118	0.115	0.118	0.121
Mn	0.001	0.000	0.000	0.000	0.001	0.000	0.000	0.000	0.000	0.001
Mg	0.000	0.000	0.000	0.312	0.301	0.310	0.299	0.295	0.297	0.311
Ca	0.000	0.001	0.001	0.003	0.000	0.001	0.000	0.001	0.000	0.003
Na	0.032	0.032	0.027	0.071	0.046	0.092	0.059	0.077	0.076	0.076
K	0.571	0.642	0.504	0.421	0.346	0.375	0.293	0.368	0.340	0.562
Na/(Na+K)	0.054	0.048	0.050	0.144	0.118	0.197	0.166	0.173	0.184	0.119

Table 6 Paragonite EMPA analysis from sample 166.

Point	244	248	249	256	257	258	259	274	275	276
SiO2	43.10	49.47	49.26	51.91	49.61	50.00	47.15	49.82	49.60	49.47
TiO2	0.08	0.08	0.05	0.06	0.05	0.07	0.06	0.05	0.03	0.05
Al2O3	33.15	40.04	41.19	41.59	40.70	40.33	37.86	40.57	40.51	40.71
FeO	1.84	0.92	0.66	0.56	0.55	0.50	1.21	0.47	0.50	0.52
MnO	0.00	0.01	0.00	0.00	0.01	0.00	0.00	0.01	0.01	0.00
MgO	0.57	0.37	0.06	0.19	0.29	0.20	0.15	0.16	0.24	0.19
CaO	0.19	0.15	0.13	0.21	0.22	0.21	0.31	0.21	0.18	0.18
Na2O	3.87	6.32	6.56	4.68	6.22	4.32	4.07	6.43	6.81	6.55
K2O	0.81	0.88	0.45	0.75	1.04	1.01	0.55	0.82	0.57	0.46
Total	83.62	98.24	98.36	99.95	98.68	96.62	91.37	98.54	98.44	98.13
Si	3.128	3.057	3.030	3.113	3.047	3.104	3.102	3.061	3.051	3.048
Ti	0.004	0.004	0.002	0.003	0.002	0.003	0.003	0.002	0.001	0.002
Al	2.835	2.916	2.986	2.939	2.946	2.951	2.936	2.937	2.937	2.956
Fe+3	0.000	0.000	0.000	0.000	0.000	0.000	0.000	0.000	0.000	0.000
Fe+2	0.112	0.048	0.034	0.028	0.028	0.026	0.067	0.024	0.026	0.027
Mn	0.000	0.001	0.000	0.000	0.001	0.000	0.000	0.001	0.001	0.000
Mg	0.062	0.034	0.006	0.017	0.027	0.019	0.015	0.015	0.022	0.017
Ca	0.010	0.010	0.009	0.013	0.014	0.014	0.022	0.014	0.012	0.012
Na	0.545	0.757	0.782	0.544	0.741	0.520	0.519	0.766	0.812	0.782
K	0.075	0.069	0.035	0.057	0.081	0.080	0.046	0.064	0.045	0.036
Na/(Na+K)	0.879	0.916	0.957	0.905	0.901	0.867	0.918	0.923	0.948	0.956

RESULTS

Description of Raspas blueschists

Blueschists from the Raspas Metamorphic Complex are characterized by rocks with good preservation of the peak assemblage with local evidence of retrogression, at variable degrees. All samples display a matrix dominated by elongated crystals of glaucophane (5 – 30 %) and clinozoisite (5 – 20 %). Depending on the sample, jadeite (15 % in one sample), garnet porphyroblasts (5 - 20 %; 5 samples), omphacite porphyroblasts (~ 5 %; one sample), or white mica (5 – 25 %) are present. Rutile, titanite, and apatite are present in all samples as accessory phases. Chlorite (up to 5 %), Na-Ca amphibole (up to 5 %), tremolite (up to 20 %), albite (up to 10 %), and carbonate (< 5 %) are trace to minor components, and their quantities are related to the retrograde process. They display small variations in their assemblage represented by (1) clinozoisite-glaucophane schists; (2) paragonite(?)-glaucophane-clinozoisite schist; (3) paragonite(?)-garnet-clinozoisite-glaucophane schist.

The samples dominated by the assemblage glaucophane + clinozoisite are fine- to medium-grained rocks with a well-developed foliation S_1 marked by the slender to rounded clinozoisite crystals enveloped by glaucophane. It is common to observe intrafolial folds forming an S_2 foliation (Fig. 2 e-f). The green-bluish cores of Na-Ca amphibole surrounded by lavender-blue glaucophane are widespread. Moreover, the clinozoisite show zoning with ‘cloudy-like’ cores with slight, rounded inclusions of albite and epidote (Fig. 2c-d), sometimes showing weak orientation (S_0). Locally, the main matrix assemblage is partially replaced by randomly distributed aggregates of albite, and albite plus chlorite occurs. These aggregates engulf relict clinozoisite minerals preserving the previous foliation S_1 and displaying epidote rims. This feature is prominent in the

samples highly affected by retrograde reactions and usually coupled with tremolite and scarce relicts of glaucophane.

The assemblage white mica + glaucophane + clinozoisite ± tremolite ± albite ± chlorite ± epidote schists are characterized by fine-to-medium grained rocks with a prominent foliation S_1 that is affected by tight folds forming the S_2. The foliation is defined by slender prismatic amphiboles with bluish-green cores and lavender blue rims and rounded to tabular clinozoisite that exhibits clear zoning with the inclusion of rich cores of epidote and albite and limpid rims (Fig. 2a-b). However, layers with fine-grained and rounded crystals of glaucophane and clinozoisite, or even with high modal amounts of white mica or clinozoisite, also occur. White mica is disseminated and may be found as small grains along the S_2 foliation or more commonly as randomly orientated.

Partial to complete replacement of tremolite after glaucophane is also observed. This transformation is usually coupled by the modal increase of albite and chlorite in the matrix and the formation of epidote rims around clinozoisite (Fig. 2 g-h). At the end of this spectrum, a greenschist assemblage is associated with the folding of the S_2 foliation and the presence of carbonate minerals disseminated through the rock.

In the presence of garnet porphyroblasts, the S_2 foliation may or may not display deflection. However, some samples exhibit both situations simultaneously. When foliation deflection occurs, a symmetrical pressure shadow is generated composed of white mica, quartz, and glaucophane (Fig. 2 a-b). The garnet is predominantly idioblastic, but subidioblastic, xenoblastic, or even rounded crystals also occur. Inclusion trails show a core with small orientated inclusions (S_1) of epidote oblique to the main foliation S_2. These inclusions suggest a correlation with the similar inclusions in the clinozoisite described above. The mantle characterizes by a curved trail of

clinozoisite inclusions with incipient continuity with the foliation originated by the rotation of the S_1 during the formation of the S_2 foliation. Marginal parts of the crystal are inclusion-free, usually associated with the idioblastic and subidioblastic garnets porphyroblasts. Only in the sample with jadeite were found oriented inclusions of this mineral at the rims of garnet. In all samples with garnet, a white mica was present. This mica is idioblastic to subidioblastic and sometimes porphyroblastic. They are mostly aligned according to the foliation, can be oblique, or even as randomly orientated aggregates.

In one sample, diamond-shaped aggregates of chlorite + epidote ± albite occur along the S_2 foliation but can occur obliquely; in the latter case, it deflects the glaucophane + epidote + white mica matrix. Both cases are associated with a pressure shadow of white mica + quartz. Aligned inclusions of clinozoisite (sometimes with epidote rims) parallel to the general foliation are present in this aggregate. Moreover, in rare cases, relics of garnet are found, thus, indicating a pseudomorph after garnet (Fig. 2c-d). The albite inside the pseudomorph could indicate that garnet breakdown was associated with consuming glaucophane or white mica.

Jadeite occurs as coarse-grained, as tabular to rounded grains. They show a distinct oscillatory zoning and have content variations across the sample, forming, at times, monomineralic layers associated with white mica or glaucophane.

Due to only one sample, 166 having omphacite and good preservation of garnet porphyroblasts, it was selected for EMPA analysis. A detailed description of this sample will be presented in the next section.

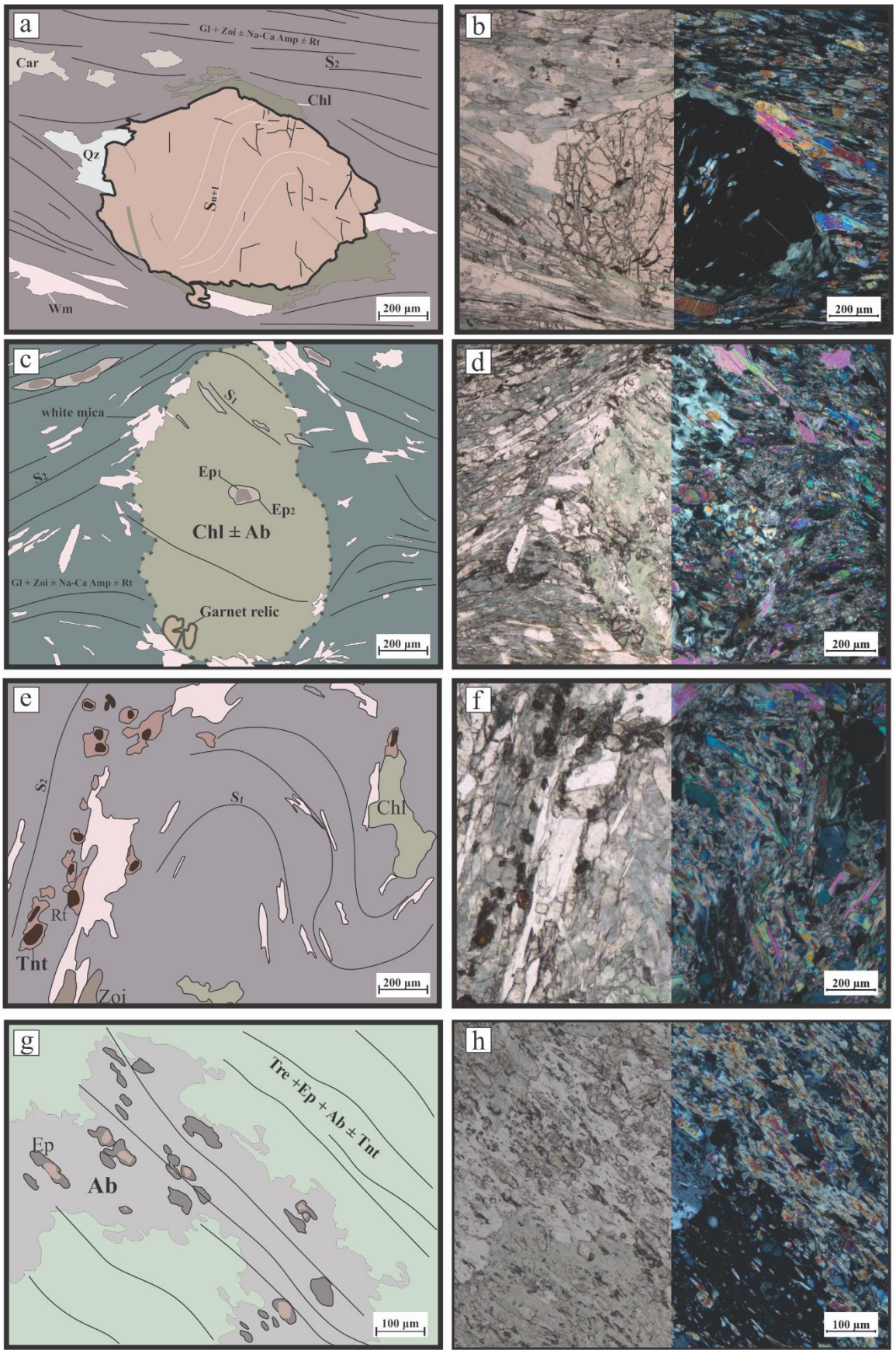
a
Gl + Zoi ± Na-Ca Amp ± Rt
Car
S2
Chl
Qz
Sn+1
Wm
200 µm
b
200 µm
c
white mica
S1
S2
Ep1
Ep2
Chl ± Ab
Gl + Zoi ± Na-Ca Amp ± Rt
Garnet relic
200 µm
d
200 µm
e
S2
S1
Chl
Rt
Tnt
Zoi
200 µm
f
200 µm
g
Tre +Ep + Ab ± Tnt
Ep
Ab
100 µm
h
100 µm

Figure 2 Textural aspects of the blueschists from Raspas Metamorphic Complex (b, d, f, h) with simplified sketches of the textures (a, c, e, g). Garnet blueschists (a, b, e, f) characterized by subidioblastic garnet porphyroblasts exhibiting inclusion trail (S_1) made up of clinozoisite/epidote. The porphyroblasts are wrapped into a foliation S_2 made up of slender clinozoisite and winchite crystals with minor white mica. Locally S_2 foliation exhibit tight folds of a previous S_1 foliation (f). The main blueschist assemblage is partially replaced due retrograde metamorphism registered by the replacement of garnet by chlorite and albite (c, d) and formation of albite, tremolite, epidote, and chlorite after glaucophane and clinozoisite (g, h).

Sample 166

This sample is made up of glaucophane (~ 40 %), garnet (~ 20 %), clinozoisite (~ 15 %), white mica (~ 10 %), and omphacite (~ 5 %). Accessory minerals are epidote, apatite, chlorite, quartz and rutile.

The remarkable feature of this sample is the mineralogical and textural changes along the foliation inherited from the compositional variations of the protolith. It is characterized by an increasing amount of garnet, clinozoisite, and quartz at the expense of glaucophane, omphacite, and white mica.

A well-developed foliation characterized by glaucophane + clinozoisite + white mica grains is observed at the garnet-absent levels of the sample. The foliation is associated with randomly orientated white mica porphyroblasts and prismatic to tabular green omphacite porphyroblasts with evidence of growth after S_2. The white mica porphyroblasts are usually surrounded by albite and minor chlorite, whereas omphacite porphyroblasts are highly fractured and exhibit orientated inclusions of glaucophane and clinozoisite (Fig. 3c-d).

The transition between these portions is marked by an increasing prominence of clinozoisite and a weak orientation of the omphacite and white mica. As a result, garnet appears abruptly as aggregates with isolated porphyroblasts between them. They possess epidote, rutile, and clinozoisite inclusions, but the inclusion pattern changes depending on how garnet is displayed. For example, the aggregated porphyroblasts have inclusions aligned with the foliation and, in rare

cases, are oblique to it. The isolated porphyroblasts are aligned and show curved inclusions that suggest a more pronounced rotation during growth (Fig. 3a-b). Furthermore, the matrix surrounding the garnet porphyroblast is dominated by quartz and clinozoisite, whereas omphacite and glaucophane are less prominent.

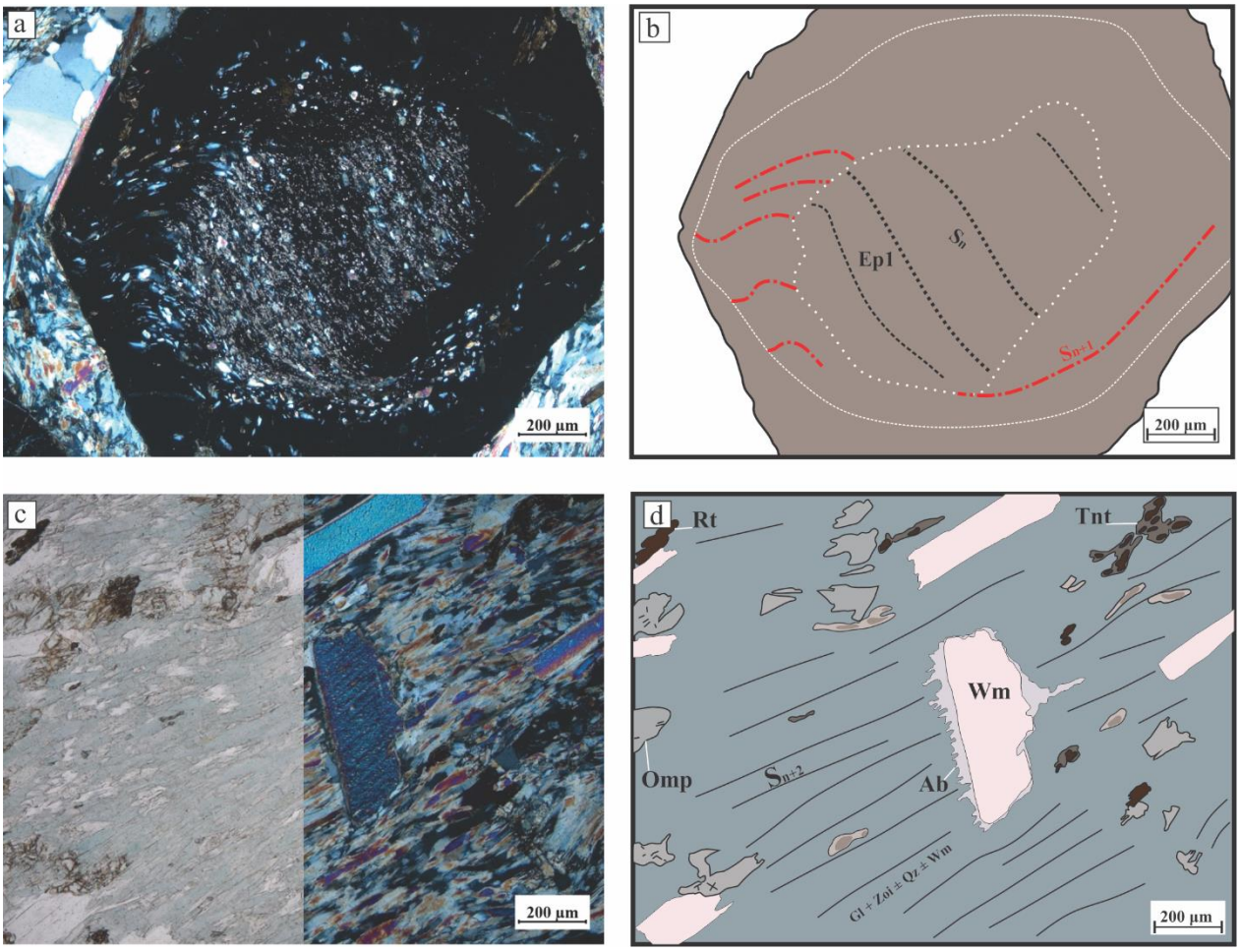

Figure 3 Textural features and sketches of the analyzed sample 166. (a, b) isolated garnet porphyroblast exhibiting a rotated inclusion trail of S_1 foliation and subidioblastic cores defined by inclusion-rich region. (c, d) omphacite and phengite porphyroblasts after S_2 characteristic of the metamorphic peak at an incipient eclogite-facies metamorphism, notice the albite rims around phengite.

Mineral composition

Garnet

This mineral has an incipient zoning better displayed by the almandine and spessartine components (Table 1). Almandine contents are lower in the core ($Alm_{0.49-0.61}$; Fig. 4c), progressively increasing until reaching the highest values at the rims ($Alm_{0.56-0.64}$; Fig. 4c). However, at the outermost rim of some grains, a slight decrease observed ($Alm_{0.56-0.60}$), usually coupled by an increase of FeO contents of amphibole at the contact with garnet crystals. Spessartine possesses a bell-shaped zoning with rich cores ($Sps_{0.17-0.07}$; Fig. 4d) followed by a progressive decrease towards the rims, where the lowest values are found ($Sps_{0.07-0.01}$; Fig. 4d).

Pyrope exhibit almost no variation across the grains. Their contents increase from $Py_{0.05-0.07}$ at the cores to $Py_{0.07-0.12}$ at the rims without a clear limit between core and rim (Fig. 4b). Grossular has their highest contents located at the cores ($Grs_{0.23-0.32}$) decreasing towards the rims ($Grs_{0.24-0.22}$). However, at the proximity of epidote inclusions, their contents reach up to $Grs_{0.35}$ even at the rims, resulting in patchy zoning (Fig. 4a).

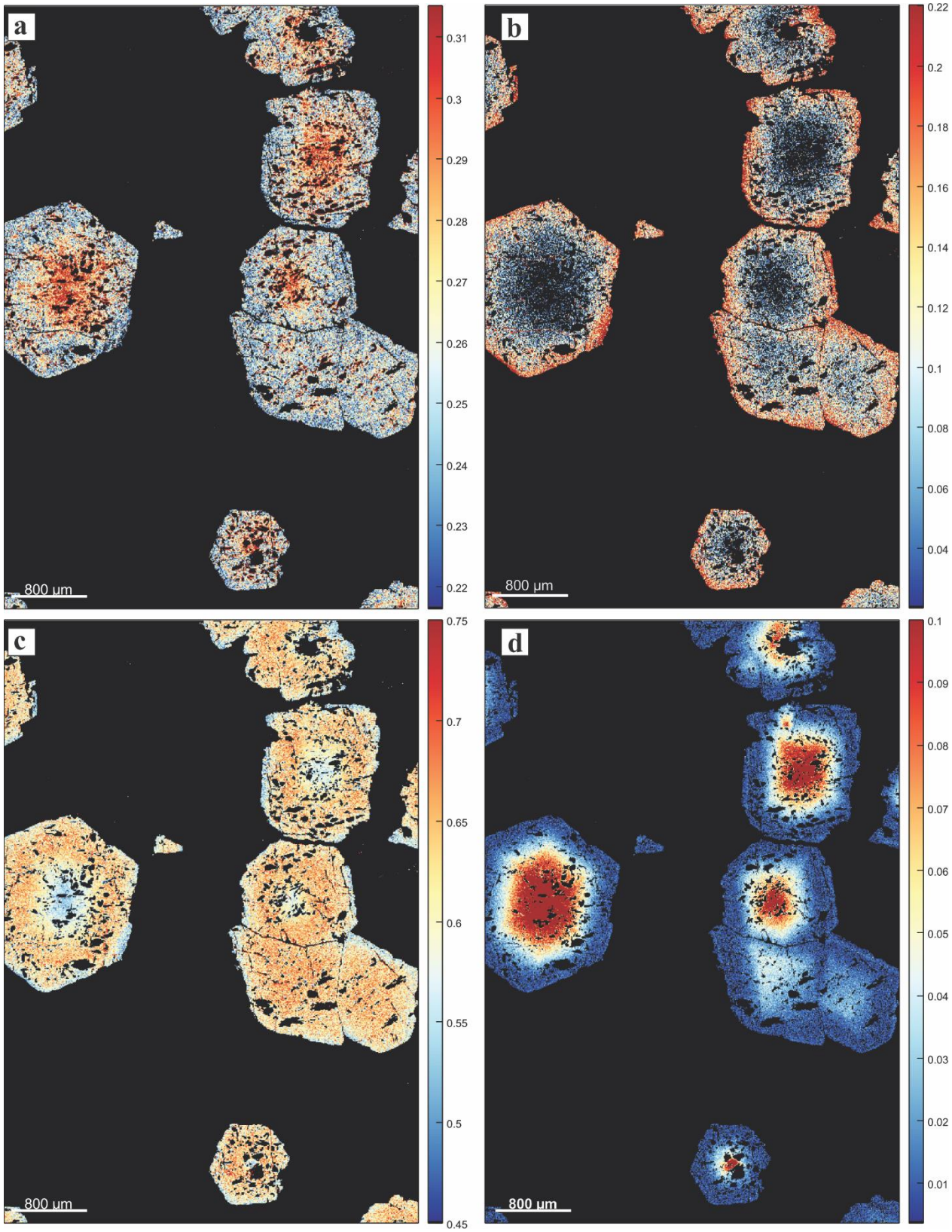

Figure 4 X-ray maps of the main garnet components, grossular (a), pyrope (b), almandine (c), and spessartine (d).

The amphiboles dominate the matrix and are mostly sodic-calcic, represented by winchite (Table 2; Following the nomenclature of Hawthorne et al., 2012) with $^{C}(Al+Fe^{3+}+2Ti)_{apfu}$ around 1.26 to 1.38, but lower values of 1.02 occur, and $^{A}(Na+K+2Ca)_{apfu}$ is between 0.05-0.24. Relicts observed by lower NaO and higher CaO in oxides wt.% maps associated with albite at their cores are also winchite possessing more constrained composition with $^{C}(Al+Fe^{3+}+2\ Ti)_{apfu}$ of 1.23-1.29 and $^{A}(Na+K+2Ca)_{apfu}$ of 0.09-0.136 (Fig. 5a, b). Close to some garnet crystals, the FeO contents increase balanced by the decrease of MgO with $^{C}(Al+Fe^{3+}+2\ Ti)_{apfu}$ of 1.72 and $^{A}(Na+K+2Ca)_{apfu}$ of 0.48, thus being classified as ferro-barroisite.

Calcic amphiboles are found as inclusions in garnet represented by actinolite with $^{C}(Al+Fe^{3+}+2Ti)_{apfu}$ of 0.28 and $^{A}(Na+K+2Ca)_{apfu}$ of 0.05 (Fig. 5b). More commonly, the calcic varieties occur as a retrograde phase featuring with albite rims around paragonite in the case of pargasite ($^{C}[Al+Fe^{3+}+2Ti]_{apfu}$ of 1.4; $^{A}[Na+K+2Ca]_{apfu}$ of 1.64). Or at the winchite rims close to albite represented by Mg-hornblende ($^{C}[Al+Fe^{3+}+2Ti]_{apfu}$ of 0.81; $^{A}[Na+K+2Ca]_{apfu}$ of 0.07).

Epidote, albite, and white mica

The inclusions of epidote in garnet and the cores of epidote at the matrix exhibit higher $Fe^{3+}/(Fe^{3+}+Al)$ around 0.23-0.25, whereas, for the majority of matrix epidote is 0.15-0.19 (Table 3). Albite is relatively homogeneous with $Ab_{0.96-0.99}$ (Table 4; Fig. 5d).

White mica is represented by a phengitic component having Na/(Na+K) between 0.12-0.20 and Si p.f.u. = 3.42-3.50 (Table 5). Muscovite included in garnet has Na/(Na+K) = 0.05 and Si p.f.u. = 4.28-4.30. The white mica associated with albite rims is paragonite displaying lower Si p.f.u. (3.03-3.12) than phengite (Table 6; Fig. 5c). Moreover, Na/(Na+K) ratios of paragonite show weak zoning with values around 0.86 in the cores that go up to 0.95 in the rims.

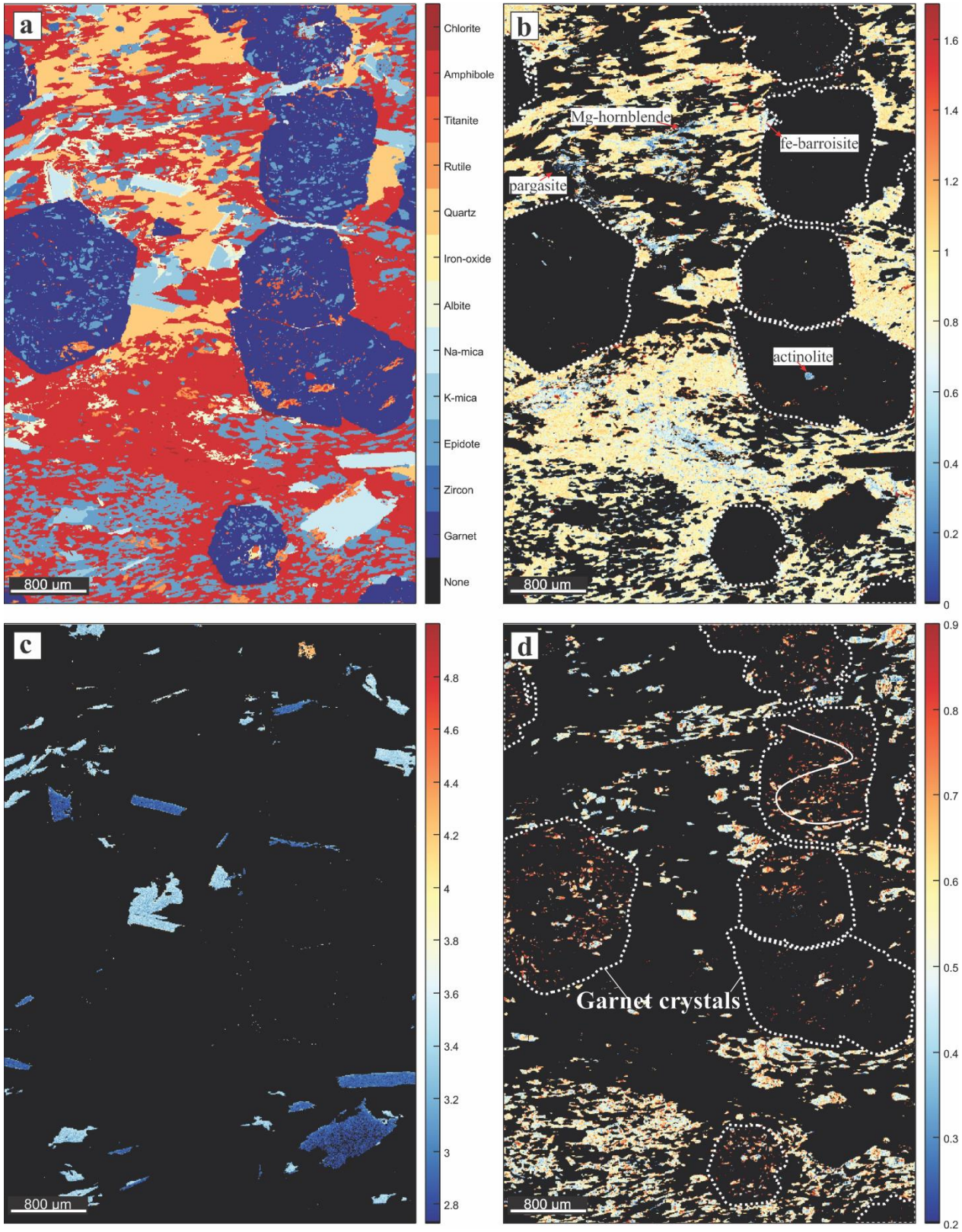
a
800 um
Chlorite
Amphibole
Titanite
Rutile
Quartz
Iron-oxide
Albite
Na-mica
K-mica
Epidote
Zircon
Garnet
None
b
Mg-hornblende
fe-barroisite
pargasite
actinolite
800 um
1.6
1.4
1.2
1
0.8
0.6
0.4
0.2
0
c
800 um
4.8
4.6
4.4
4.2
4
3.8
3.6
3.4
3.2
3
2.8
d
Garnet crystals
800 um
0.9
0.8
0.7
0.6
0.5
0.4
0.3
0.2

Figure 5 (a) mask image showing the mineral proportion on the analyzed region. (b) Map of Na_{apfu} contents on the M_4 site on amphiboles. (c) Si_{apfu} map on white micas. (d) Fe^{3+}_{apfu} on M_3 site of epidote, the outline of garnet crystals is highlighted as dashed white lines, whereas S_1 foliation defined by epidote inclusions is represented by the white line.

Thermodynamic Modeling

NCFMASH

In this system, garnet appears at pressures around 0.5-0.8 GPa, followed by the disappearance of albite coupled by the change of amphibole from a calcic composition towards a sodic-calcic one at higher pressures (Fig. 6). chlorite occurs at lower pressures (< 0.75 GPa) close to the garnet-in tie line consistent with the replacement of chlorite after garnet observed in samples with a certain degree of retrograde reactions (Fig. 6). However, chlorite reappears at pressures above 1.0 GPa and < 550 °C, usually accompanied to sodic-calcic amphiboles, which was not observed in any sample. Epidote is restricted to T < 370 °C and P > 0.74 GPa and is replaced by zoisite as the temperature goes up (Fig. 6). As the K_2O is suppressed in this system, the only micaceous mineral predicted is paragonite, moreover, it is predicted in a small field from 0.74-0.76 GPa at 350 °C to 1.25-1.3 GPa at 500-520 °C (Fig. 6). omphacite is restricted to pressures > 1.3 GPa and temperatures above 550 °C, usually associated with sodic-calcic amphibole and more rarely glaucophane. Lawsonite is not reported in the Raspas Complex; this system is restricted to pressures above 1.75 GPa and temperatures < 530 °C (Fig. 6).

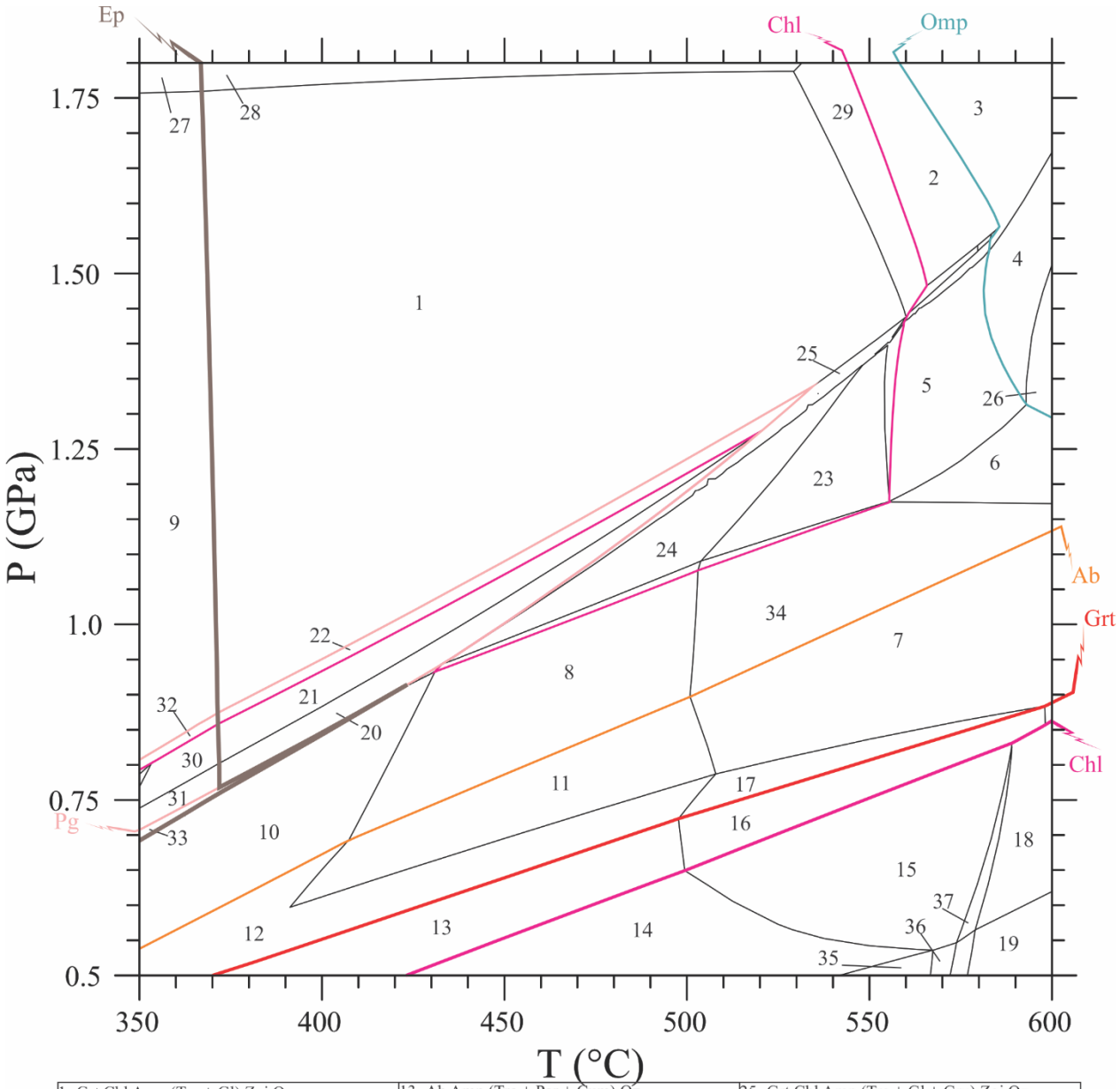

1- Grt Chl Amp (Tre + Gl) Zoi Qz	13- Ab Amp (Tre + Par + Cum) Qz	25- Grt Chl Amp (Tre + Gl + Gru) Zoi Qz
2- Grt Amp (Tre + Gl) Zoi Qz	14- Ab Chl Amp (Tre + par + Cum) Qz	26- Grt Omp Amp (par) Qz
3- Grt Omp Amp (Tre + Gl) Zoi Qz	15- Ab Chl Amp (Gru + Cum) Qz	27- Ep Grt Chl Amp (Tre + Gl) Lws Qz
4- Grt Omp Amp (Gl) Zoi Qz	16- Ab Amp (Par + Cum) Qz	28- Grt Chl Amp (Tre + Gl) Zoi Lws Qz
5- Grt Amp (Gl) Zoi Qz	17- Ab Grt Amp (Par + Cum) Qz	29- Grt Chl Amp (Tre + Gl) Zoi Qz
6- Grt Amp (Par) Qz	18- Ab Amp (gru + Cum) Qz	30- Ep Grt Amp (Tre + Gl) Pg Qz
7- Ab Grt Amp (Par) Qz	19- Ab Amp (gru + Cum)	31- Ep Grt Amp (Tre + Par + Gl) Pg Qz
8- Grt Amp (Tre + Gru) Qz	20- Grt Amp (Tre + Par + Gl) Zoi Pg Qz	32- Ep Grt Chl Amp (Tre + Gl) Pg Qz
9- Ep Grt Chl Amp (Tre + Gl) Qz	21- Grt Amp (Tre + Gl) Zoi Pg Qz	33- Ep Grt Amp (Tre + Par + Gl) Qz
10- Grt Amp (Tre + Par + Gl) Qz	22- Grt Chl Amp (Tre + Gl) Zoi Pg Qz	34- Grt Amp (Gru) Qz
11- Ab Grt Amp (Tre + Par) Qz	23- Grt Chl Amp (Gru) Zoi Qz	35- Ab Chl Amp (Tre + Gru + Cum)
12- Ab Grt Amp (Tre + Par + Cum) Qz	24- Grt Chl Amp (Tre + Gru) Zoi Qz	36- Ab Chl Amp (Gru + Cum)
		37- Ab Chl Amp (Gru + Cum) Qz

Figure 6 Isochemical phase diagram of the analyzed sample on the Na_2O-CaO-FeO-MgO-SiO_2-H_2O (NCFMASH) system. The main mineral tie lines are colored. Mineral abbreviations are Chl – chlorite; Grt – garnet; Ab – albite; Omp – omphacite; Ep – epidote; Pg – paragonite.

NCKFMASH

The addition of K_2O to the system caused some noticeable changes. First, muscovite and potassic feldspar is present, where the former appears at lower P and T at the expense of the latter (Fig. 7). Another critical phase that appears is the clinopyroxene, that is present between the omphacite and albite fields at T < 530 °C and P between 1.1 – 1.3 GPa, rarely coexisting with omphacite or albite (Fig. 7). Then, albite, garnet fields were slightly expanded to higher pressures. In contrast, omphacite first appeared at T ~10 °C lower than in the NCFMASH (Fig. 7). Chlorite and paragonite fields suffered noticeable retractions, whereas epidote and zoisite were unaffected.

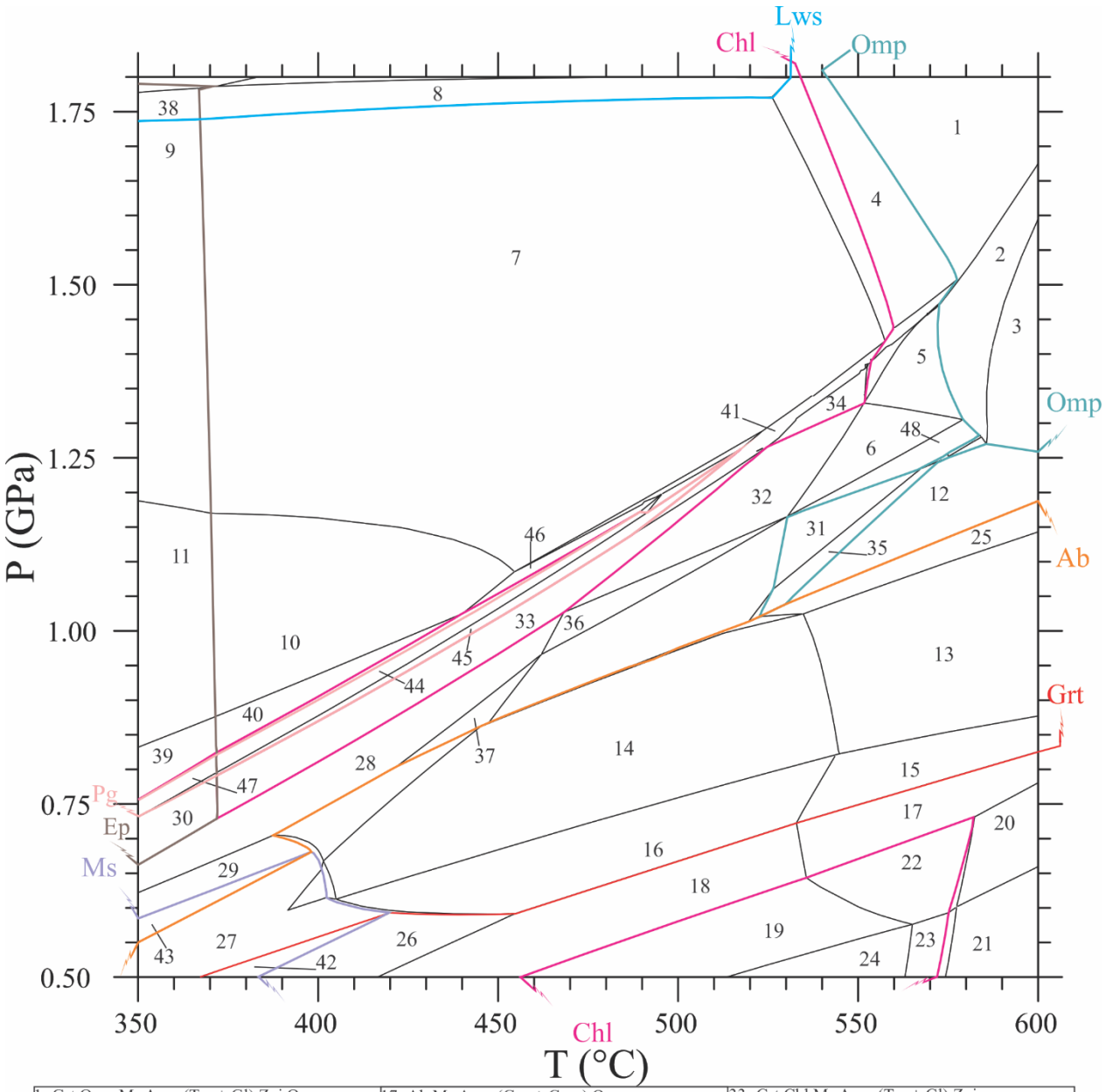

1- Grt Omp Ms Amp (Tre + Gl) Zoi Qz	17- Ab Ms Amp (Gru + Cum) Qz	33- Grt Chl Ms Amp (Tre + Gl) Zoi
2- Grt Omp Ms Amp (Gl) Zoi Qz	18- Ab Ms Amp (Tre + Par Cum) Qz	34- Grt Chl Ms Amp (Tre + Gl) Zoi Qz
3- Grt Omp Ms Amp (Gl) Qz	19- Ab Chl Ms Amp (Tre + Gru +Cum) Qz	35- Grt Cpx Omp Ms Amp (Gru) Qz
4- Grt Ms Amp (Tre + Gl) Zoi Qz	20- Ab Ms Amp (Gru) Qz	36- Grt Ms Amp (Tre + Par) Qz
5- Grt Ms Amp (Gl) Zoi Qz	21- Ab Ms Amp (Gru +Cum)	37- Grt Omp Ms Amp (Tre + Par + Gl) Qz
6- Grt Ms Amp (Gru) Zoi Qz	22- Ab Chl Ms Amp (Gru) Qz	38- Ep Grt Chl Ms Amp (Tre + Gl) Lws Qz
7- Grt Chl Ms Amp (Tre + Gl) Zoi Qz	23- Ab Chl Ms Amp (Gru)	39- Ep Grt Chl Ms Amp (Tre + Par + Gl)
8- Grt Chl Ms Amp (Tre + Gl) Zoi Lws Qz	24- Ab Chl Ms Amp (Tre + Gru + Cum)	40- Grt Chl Ms Amp (Tre + Par + Gl) Zoi
9- Ep Grt Chl Ms Amp (Tre + Gl) Qz	25- Ab Grt Cpx Ms Amp (Gru) Qz	41- Grt Chl Ms Amp (Tre + Gl + Gru) Zoi Qz
10- Grt Chl Ms Amp (Tre + Gl) Zoi	26- Ab Ms Amp (Tre + Par + Cum) Kf Qz	42- Ab Amp (Tre + Par + Cum) Kf Qz
11- Ep Grt Chl Ms Amp (Tre + Gl)	27- Ab Grt Amp (Par +Gl) Kf Qz	43- Grt Amp (Tre + Par + Gl) Kf Qz
12- Grt Cpx Ms Amp (Par) Qz	28- Grt Ms Amp (Tre + Par + Gl) Qz	44- Grt Ms Amp (Tre + Par + Gl) Zoi Pg
13- Ab Grt Ms Amp (gru) Qz	29- Grt Ms Amp (Tre + Par + Gl) Kf Qz	45- Grt Ms Amp (Tre + Par + Gl) Zoi Pg Qz
14- Ab Grt Ms Amp (Tre + Par) Qz	30- Ep Grt Ms Amp (Tre + Par + Gl) Qz	46- Grt Chl Ms Amp (Tre + Gl) Zoi Qz
15- Ab Grt Ms Amp (gru + Cum) Qz	31- Grt Omp Ms Amp (Gru) Qz	47- Ep Grt Ms Amp (Tre + Par + Gl) Pg
16- Ab Grt Ms Amp (Tre + Par + Cum) Qz	32- Grt Ms Amp (Tre + Gru) Zoi Qz	48- Ab Grt Ms Amp (Gru + Cum) Qz

Figure 7 Isochemical phase diagram on the chemical system Na_2O-CaO-K_2O-FeO-MgO-SiO_2-H_2O (NCKFMASH). Mineral abbreviations are as on Figure 6, except Lws – lawsonite.

Accessing the Fe^{3+}

Due to most of the geochemical analysis only analyzing the total iron either as FeO or as Fe_2O_3, it is easier to estimate the amount of ferric iron by directly analyzing the iron valences from each mineral. That usually causes the underestimating of the stability field of Fe^{3+}-bearing phases. In our case, this is better represented by the limited field of epidote, contrasting with its widespread presence during various stages of the metamorphic and textural history. A way to avoid this problem is by adding a small quantity of extra oxygen in the system that forces the model to accommodate those extra oxygens in the phases bearing ferric iron.

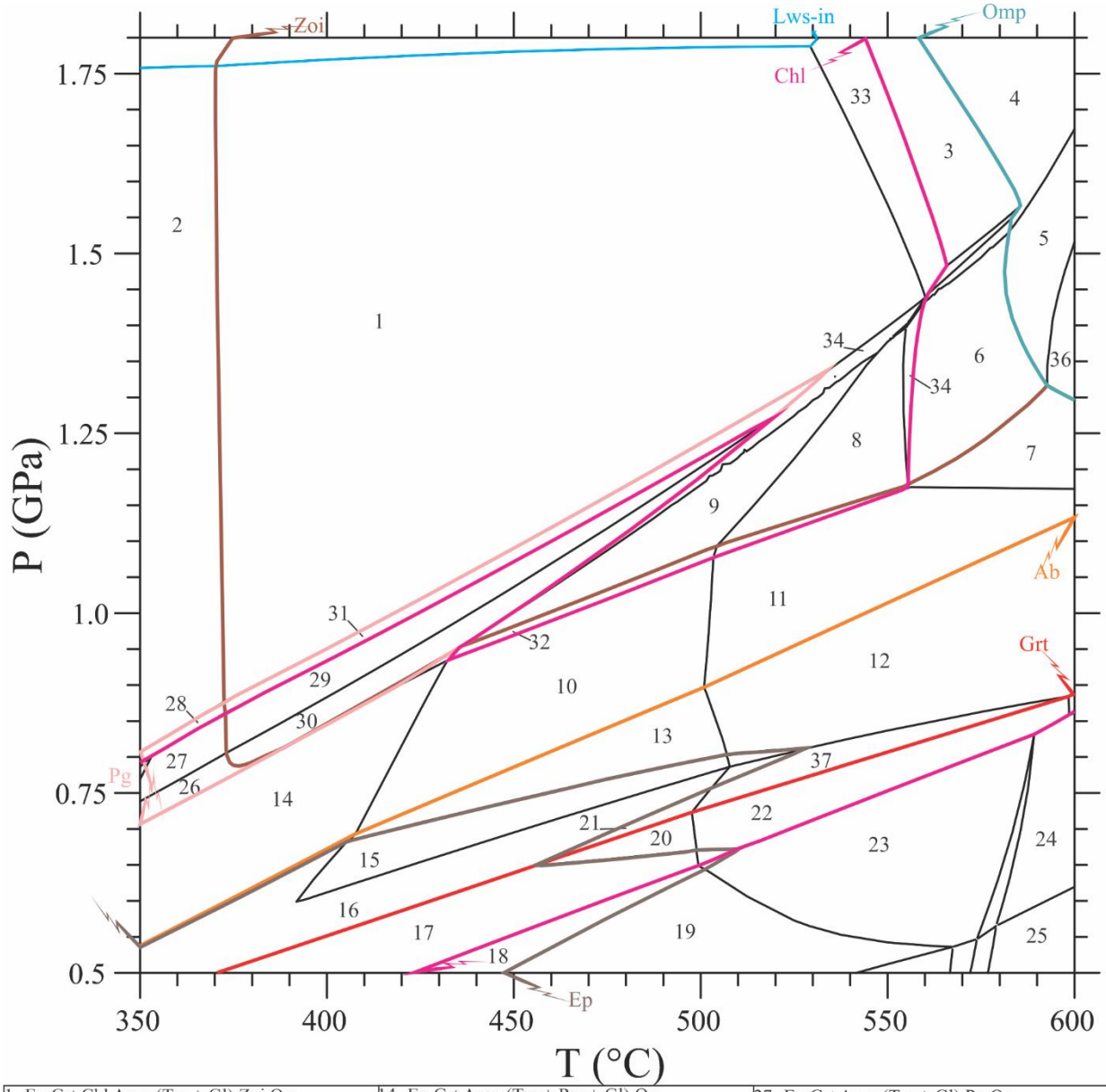

1- Ep Grt Chl Amp (Tre + Gl) Zoi Qz	14- Ep Grt Amp (Tre + Par + Gl) Qz	27- Ep Grt Amp (Tre + Gl) Pg Qz
2- Ep Grt Chl Amp (Tre + Gl) Qz	15- Ab Grt Amp (Tre + Par + Rie) Qz	28- Ep Grt Chl Amp (Tre + Gl) Pg Qz
3- Ep Grt Amp (Tre + Gl) Zoi Qz	16- Ab Grt Amp (Tre + Par + Cum + Rie) Qz	29- Ep Grt Amp (Tre + Gl) Zoi Pg Qz
4- Ep Grt Omp Amp (Tre + Gl) Zoi Qz	17- Ab Amp (Tre + Par + Cum + Rie) Qz	30- Ep Grt Amp (Tre + Gl + Par) Zoi Pg Qz
5- Ep Grt Omp Amp (Gl) Zoi Qz	18- Ab Chl Amp (Tre + Par + Cum + Rie) Qz	31- Ep Grt Chl Amp (Tre + Gl) Zoi Pg Qz
6- Ep Grt Amp (Gl) Zoi Qz	19- Ab Ep Chl Amp (Tre + Par + Cum) Qz	32- Ep Grt Chl Amp (Tre + Par) Qz
7- Ep Grt Amp (Par) Qz	20- Ab Ep Amp (Tre + Par + Cum) Qz	33- Ep Grt Chl Amp (Tre + Gl) Zoi Qz
8- Ep Grt Chl Amp (Gru) Zoi Qz	21- Ab Ep Grt Amp (Tre + Par + Cum) Qz	34- Ep Grt Chl Amp (Tre + Gl + Gru) Zoi Qz
9- Ep Grt Chl Amp (Tre + Gru) Zoi Qz	22- Ab Ep Amp (Par + Cum) Qz	35- Ep Grt Chl Amp (Gl) Zoi Qz
10- Ep Grt Amp (Tre Par) Qz	23- Ab Ep Chl Amp (Par + Cum) Qz	36- Ep Grt Omp Amp (Par) Qz
11- Ep Grt Amp (Gru) Qz	24- Ab Ep Amp (Par + Cum) Qz	37- Ab Ep Grt Amp (Par +Cum) Qz
12- Ab Ep Grt Amp (Par) Qz	25- Ab Ep Amp (Gru + Cum)	
13- Ab Ep Grt Amp (Tre + Par) Qz	26- Ep Grt Amp (Tre + Par + Gl) Pg Qz	

Figure 8 Isochemical phase diagram on the NCFMASH with oxygen in excess. Mineral abbreviations are as on Figure 7.

As expected, this enables the expansion of the epidote field to pressures above 0.55 GPa and temperatures above 450 °C in the NCFMASH (Fig. 8), and even more so in the NCKFMASH, where it appears at T > 390 °C and P > 0.55 GPa (Fig. 9). As an additional effect, zoisite is predicted at T above 370 °C and P > 0.75 GPa both in the NCFMASH and NCKFMASH. Only in the NCKFMASH slight changes in the omphacite and chlorite fields are noticed.

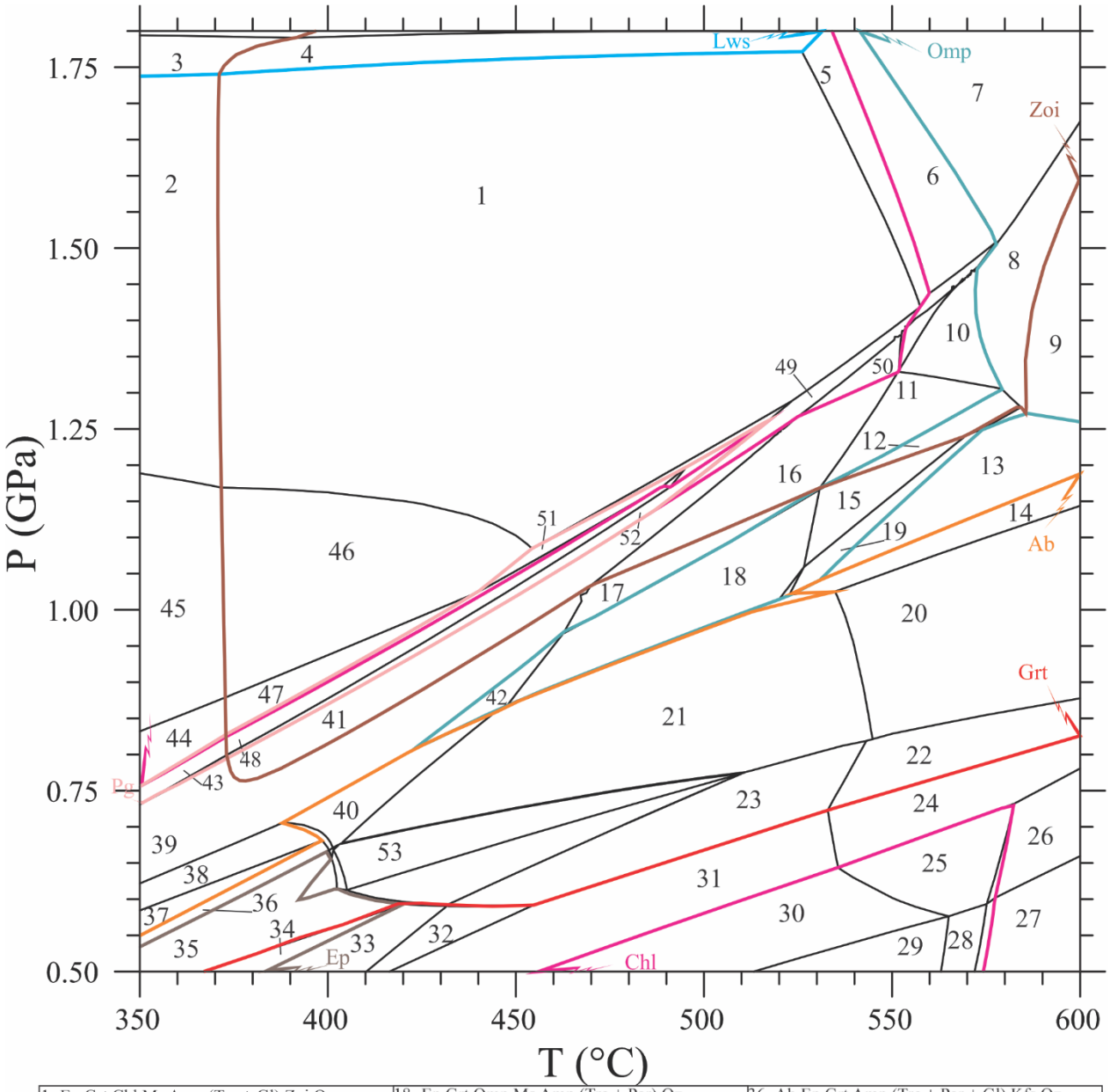

1- Ep Grt Chl Ms Amp (Tre + Gl) Zoi Qz	18- Ep Grt Omp Ms Amp (Tre + Par) Qz	36- Ab Ep Grt Amp (Tre + Par + Gl) Kfs Qz
2- Ep Grt Chl Ms Amp (Tre + Gl) Qz	19- Ep Grt Cpx Omp Ms Amp (Gru) Qz	37- Ep Grt Amp (Tre + Par + Gl) Kfs Qz
3- Ep Grt Chl Ms Amp (Tre + Gl) Lws Qz	20- Ab Ep Grt Ms Amp (Gru) Qz	38- Ep Grt Ms Amp (Tre + Par + Gl) Kfs Qz
4- Ep Grt Chl Ms Amp (Tre + Gl) Zoi Lws Qz	21- Ab Ep Grt Ms Amp (Tre + Par) Qz	39- Ep Grt Ms Amp (Tre + Par + Gl) Qz
5- Ep Grt Chl Ms Amp (Tre + Gl) Zoi Qz	22- Ab Ep Grt Ms Amp (Gru + Cum) Qz	40- Ab Ep Grt Ms Amp (Tre + Par + Gl) Qz
6- Ep Grt Ms Amp (Tre + Gl) Zoi Qz	23- Ab Ep Grt MS Amp (Tre + Gru + Cum) Qz	41- Ep Grt Ms Amp (Tre + Par Gl) Zoi Qz
7- Ep Grt Omp Ms Amp (Tre + Gl) Zoi Qz	24- Ab Ep Ms Amp (Gru + Cum) Qz	42- Ep Grt Omp Ms Amp (Tre +Par + Gl) Qz
8- Ep Grt Omp Ms Amp (Gl) Zoi Qz	25- Ab Ep Chl Ms Amp (Gru + Cum) Qz	43- Ep Grt Ms Amp (Tre +Par Gl) Pg
9- Ep Grt Omp Ms Amp (Gru) Qz	26- Ab Ep Ms Amp (Gru + Cum) Qz	44- Ep Grt Chl Ms Amp (Tre + Par + Gl)
10- Ep Grt Ms Amp (Gl) Zoi Qz	27- Ab Ep Ms Amp (Gru + Cum)	45- Ep Grt Chl Ms Amp (Tre + Gl)
11- Ep Grt Ms Amp (Gru) Zoi Qz	28- Ab Ep Chl Ms Amp (Gru + Cum)	46- Ep Grt Chl Ms Amp (Tre + Gl) Zoi
12- Ep Grt Omp Ms Amp (Gru) Zoi Qz	29- Ab Ep Chl Ms Amp (Tre + Gru + Cum)	47- Ep Grt Chl Ms Amp (Tre + Par + Gl) Zoi
13- Ep Grt Cpx Ms Amp (Gru) Qz	30- Ab Ep Chl Ms Amp (Tre + Gru + Cum) Qz	48- Ep Grt Ms Amp (Tre + Par + Gl) Zoi Pg
14- Ab Ep Grt Cpx Ms Amp (Gru) Qz	31- Ab Ep Ms Amp (Tre + Gru + Cum)Qz	49- Ep Grt Chl Ms Amp (Tre + Gl + Gru) Zoi Qz
15- Ep Grt Omp Ms Amp (Gru) Qz	32- Ab Ep Ms Amp (Tre +Par + Cum) Kfs Qz	50- Ep Grt Chl Ms Amp (Tre + Gl) Zoi Qz
16- Ep Grt Ms Amp (Tre + Gru) Zoi Qz	33- Ab Ms Amp (Tre +Par + Cum + Rie) Kfs Qz	51- Ep Grt Chl Ms Amp (Tre + Gl) Zoi Pg
17- Ep Grt Ms Amp (Tre + Par) Qz	34- Ab Amp (Tre +Par +Cum + Rie) Kfs Qz	52- Ep Grt Ms Amp (Tre + Par + Gl) Zoi Pg Qz
	35- Ab Grt Amp(Tre + Par + Gl + Rie) Kfs Qz	53- Ab Grt Ms Amp (Tre + Par Rie) Qz

Figure 9 Isochemical phase diagram on the NCKFMASH with excess of oxygen. Mineral abbreviations are as on Figure 7 except Zoi – zoisite.

GrtMod modelling

To access the P-T conditions attained during the garnet growth stages and help solve the metamorphic evolution, we performed the modeling in the GrtMod version 2.0 (Lanari et al., 2017). The same thermodynamic database from the modeling above was used. Moreover, we run the modeling in the NCFMASH and NCKFMASH, considering with and without O in excess.

The models consider only two stages of garnet growth (i.e., core and rim) without considering significant resorption.

Core. In all modeled systems, the onset of garnet growth conditions was constrained at similar P-T conditions at ~ 523 °C and 1.68 GPa for a residue value (C_0) of 0.02. They only differ in the amount of garnet formed, where, in the NCFMASH was ~ 19 %, whereas, for the NCKFMASH, it was ~ 11 % (Fig. 10). The addition of O in both models caused the amount of garnet predicted to decrease to ~ 11 % and ~ 10 %, respectively.

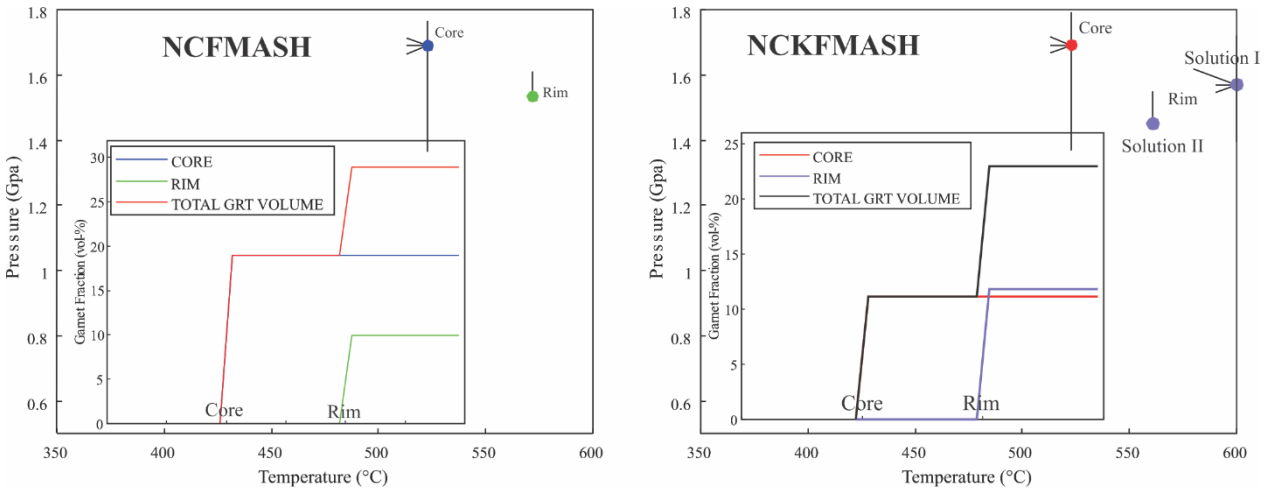

Figure 10 P-T diagram showing a summary of the modelling of garnet growth stages using the GrtMod program on NCFMASH and MCKFMASH. Moreover, a diagram of the resulting garnet volumes on each chemical system are shown.

Rim. The NCFMASH resulted in one solution constrained at 572 °C and 1.53 GPa for a C_0 of 0.004 and an amount of garnet of 9.9 %, resulting in a total volume of ~28 %. In contrast, two results were obtained in the NCKFMASH. The first resulted in conditions of 599 °C and 1.57 GPa with C_0 of 0.03 for a garnet volume of 18 %. The program selected the second solution constrained at 561 °C and 1.45 GPa for the same C_0 but with a noticeably lower garnet volume of 11 % (Fig. 10). The modeling did not find solutions during the addition of O in both systems.

DISCUSSION

Textural evolution

The main metamorphic assemblage observed through the samples is characteristic of blueschist facies dominated by winchite + clinozoisite + white mica (paragonite) + garnet (core) with an incipient eclogite-facies paragenesis during the formation of omphacite + garnet (rim) + white mica (phengite + paragonite). Moreover, the presence of tremolite + albite replacing the peak

metamorphic assemblage at variable degrees suggests an apparent retrogression toward greenschist facies minerals.

Associated with the blueschist facies assemblage, evidence from a possible early metamorphic event represented by epidote + albite inclusions in clinozoisite, inclusions of epidote at the cores of garnet, and the winchite cores. Thus, the first metamorphic event can be constrained due to the formation of the assemblage epidote + albite + winchite cores along an S_1 foliation, which could indicate the transition from a greenschist facies assemblage to a blueschist facies assemblage during the prograde path.

Only epidote and locally epidote with albite inclusions in garnet and clinozoisite, respectively, suggest that garnet and clinozoisite nucleated together. Because the inclusions that garnet and clinozoisite possess at their cores preserve S_1, they probably growth after S_1 and before S_2. Contemporaneous to S_1 the albite disappears coupled with the formation of glaucophane and white mica (depending on the composition) in equilibrium with garnet cores and clinozoisite. During S_2, the folding followed by rotation was coupled with the growth of garnet mantles and the further development of the blueschist facies assemblage. After S_2, an incipient eclogite-facies assemblage during the formation of omphacite + white mica porphyroblasts and minor jadeite is in equilibrium with the garnet rims.

The retrograde metamorphism is marked mainly by the formation of carbonate or albite or even albite + chlorite patches coupled with the formation of tremolite and minor Mg-hornblende replacing glaucophane coupled with epidote rims around clinozoisite. Chlorite or Chlorite + epidote ± albite after garnet was also observed.

Metamorphic Evolution

NCFMASH

The early stages dominated by Ep + Ab inclusions in Zoi and Na-Ca Amp during S_1 development were not observed in this model. However, the presence of Ep inclusions in Grt and Zoi limits the minimum T attained by the blueschists rocks to above 370 °C; as the garnet was formed together with Zoi before S_2, it constrains the minimum pressure at above 0.75 GPa (Fig. 11a).

The assemblage paragonite + winchite that dominates the S_1 matrix is restricted to the narrow field of paragonite comprising T between 370 °C from 0.75-0.85 GPa to 530 °C at 1.33 GPa further constrained by the isopleths of Na-M_4 of amphibole between 0.4-0.8 consistent with the composition of the winchite relicts of the matrix highlighted in the Figure 11a between 485-500 °C at 1.15 GPa. At these conditions, the paragonite and Na-Ca amphibole are predicted to occur with garnet, zoisite, chlorite, and quartz. However, constraints for the garnet growth given by the GrtMod modeling indicate higher P-T conditions at 523 °C and 1.68 GPa suggesting a considerable amount of overstepping (Fig. 10). These conditions at this model fall at the garnet + chlorite + Na-Ca amphibole + zoisite + quartz field. That, together with the Na-M_4 site isopleths of the matrix winchite (0.9), suggests that, at least in the NCFMASH, the S_1 matrix was formed during a near isothermal compression between 1.25-1.7 GPa (Fig. 11a). Moreover, the lack of chlorite vestiges predicted to be stable at the conditions indicated by the GrtMod indicate consumption of this mineral around 550°C before the formation of garnet rims.

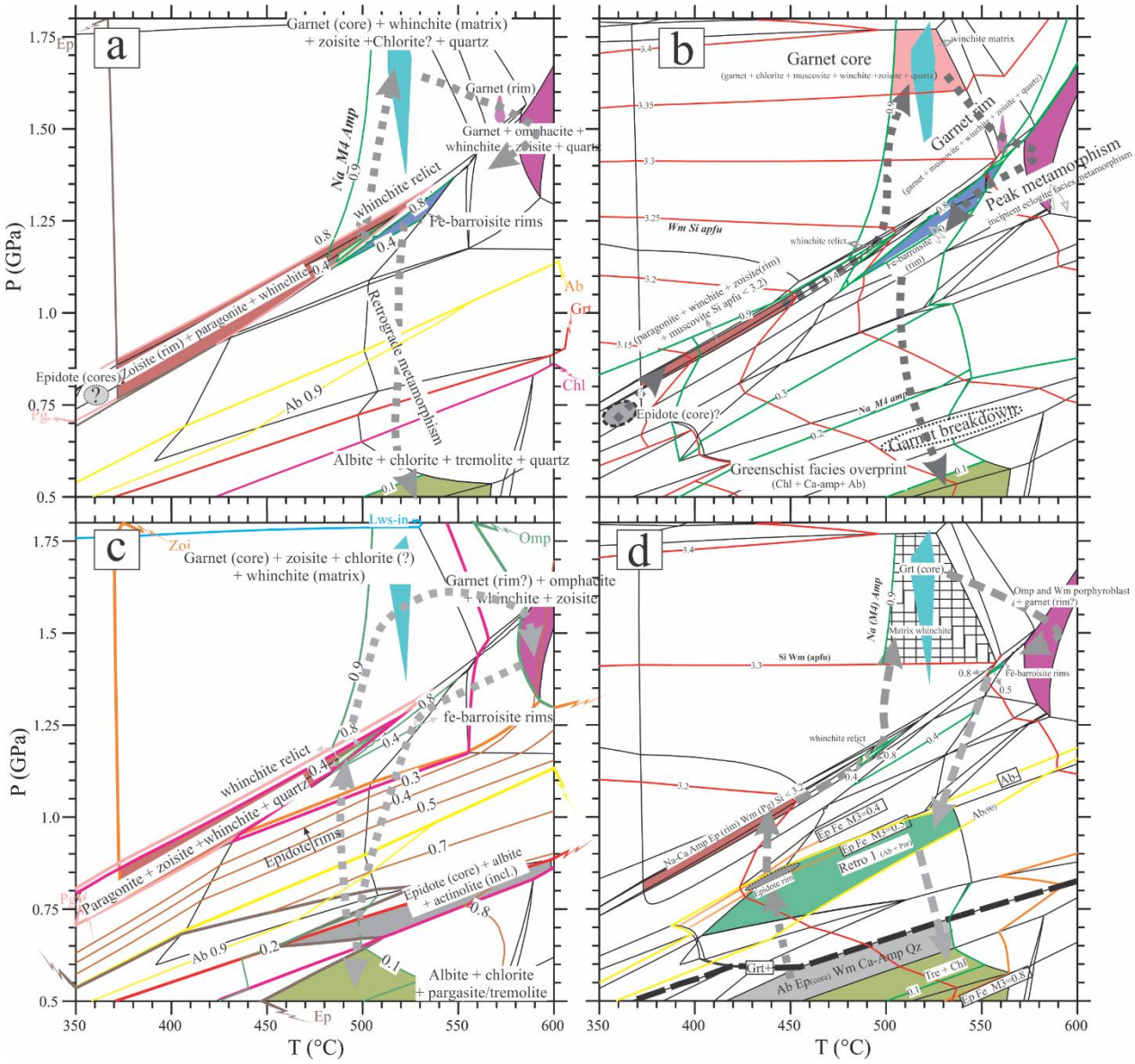

Figure 11 Simplified isochemical phase diagram of Figures 6-9 superimposed with a summary of the P-T evolution on NCFMASH (a), NCKFMASH (b), and considering oxygen in excess (c, d); see text for further discussion. Mineral abbreviations on tie lines are as on Figure 7. Isopleths of Si_{apfu} on white mica (Wm Si apfu), Na_{apfu} on M_4 of amphiboles (Na_M_4 amp), and $Fe^{3+}{}_{apfu}$ on M_3 site of epidote (Ep Fe_M_3) are also plotted.

The garnet rims constrained at 572 °C and 1.53 GPa, coincides with the field of Na-Ca amphibole + zoisite + quartz points toward an early decompression tendency, or at least an attempt, of the blueschists during the formation of S_2 and prior metamorphic peak (Fig. 11a). The appearance of omphacite in the sample 166 limit the peak metamorphic conditions at ~ 580-600

°C and 1.3-1.65 GPa. However, white mica is not predicted under these conditions in this system. Moreover, the pressure may be slightly lower due to the decompression tendency shown by the conditions on the garnet rims.

The presence of Fe-barroisite in contact with the garnet rims constrains the early stages of the exhumation at 485-550°C and 1.1-1.35 GPa by the Na in the M_4 isopleths between 0.4-0.8. The breakdown of winchite is marked by the appearance of albite ~0.9 GPa, followed by the consumption of garnet at 0.7 GPa to the formation of chlorite at 0.6 GPa (Fig. 11a). Although epidote does not occur at lower pressures in this model, the final retrograde assemblage dominated by albite + chlorite + tremolite is present soon after the Chl tie-line is crossed. They are further constrained by matrix pargasite and Mg-hornblende with Na-M_4 < 0.1 at pressures < 0.6 GPa and temperatures between 500-560 °C.

NCKFMASH

Although the epidote field can suggest lower conditions, the onset of the metamorphic evolution is constrained by the field of paragonite coexisting with Na-Ca amphibole, zoisite, and garnet during the formation of S_1. However, in this model, it is accompanied by the presence of muscovite. The assemblage evolved along this field as the Si contents on white mica increased from~ 370 °C between ~ 0.79-0.83 GPa to 485-505 °C and 1.15-1.20 GPa where the winchite relicts with Na in the M_4 between 0.4-0.8 is constrained (Fig. 11b).

As in the NCFMASH, although garnet appears at lower conditions in the isochemical phase diagram, the favorable conditions that enable their growth was only attained after a nearly isothermal compression at 523 °C and 1.68 GPa. This time garnet cores are predicted to have occurred with the assemblage chlorite + muscovite (Si apfu > 3.3) + winchite (Na in the M_4 ~0.9)

+ zoisite + quartz (Fig. 10; 11b). The garnet rims equilibrated at 561 °C and 1.45 GPa coexisting with muscovite + Na-Ca amphibole + zoisite + quartz (Fig 11b).

Peak metamorphic conditions during the formation of omphacite and white mica (phengite) porphyroblasts associated with winchite are constrained at lower conditions than in the NCFMASH. This assemblage covers a P-T field from 570-590 °C at 1.30-1.45 to 600 °C at 1.60-1.68 GPa (Fig. 11b).

The retrograde path is constrained by the formation of albite at pressures < 1.20 GPa associated with the swift from glaucophane to calcic amphibole. Garnet replacement begins at pressures < 0.80 GPa, followed by the formation of chlorite coupled by albite and calcic amphibole at 460-570 °C at pressures < 0.70 GPa (Fig. 11b).

Models with excess of oxygen

The main difference here is that it allows the albite, epidote, and tremolite to coexist at lower P-T, constraining the early assemblages founded in the blueschists. In the NCFMASH, it occurs at 460-600 °C 0.65-0.90 GPa close to the garnet and chlorite tie lines by the field of albite + epidote (with Fe^{3+} in the M3 site = 0.7-0.8) + Ca-amphibole + quartz (Fig. 11c). The same assemblage occurs coexisting with white mica at lower conditions in the NCKFMASH at 420-530 °C and < 0.70 GPa (Fig. 11d). They also differ by the absence of solutions for the garnet rims and a slight decrease of the paragonite field. Moreover, it also allows the presence of epidote and white mica to coexist with albite, chlorite, and calcic amphibole during the retrograde path (Fig. 11c, d).

Implications for the evolution of the Raspas Metamorphic Complex; insights on the subduction of oceanic plateaus

The Raspas Unit is marked by blueschist assemblages close to eclogite and the local presence of garnet amphibolite and greenschist. Previous works consider the blueschists part of the early stages of the retrograde path experienced by the eclogites. This assumption got more traction after the Lu-Hf ages presented by John et al. (2010), showing a slightly younger age for the blueschists of 126.4 ± 4.0 Ma compared with the 133.4 ± 2.1 Ma for the eclogites. Thus, leading to the assumption that the blueschists were part of the retrograde path. However, textural and thermodynamic constraints presented in this work evidence that the blueschists preserved the early stages of the subduction of the Raspas Plateau.

Although rare, the coexistence of blueschist and eclogite can be found in several localities; Tianshan Belt (China; Tian and Wei, 2014), Urals (Russia; Goméz-Pugnaire et al., 1997), or Cyclades orogens (Greece; Foster and Lister, 1999) are some examples. A common feature in those localities is the similar metamorphic path and peak temperature for both blueschist and eclogite.

A possible explanation for this feature is that compositional differences favored the formation of one assemblage instead of the other. In this case, the element responsible for this varies; some argue that it is NaO and CaO (Gosso et al., 2010), for others are FeO and MnO or even C/CNK ratios (Oh et al., 1991; Tian and Wei, 2014). Another common explanation is the variation of water budget present in the rock favoring the preservation of hydrated blueschist assemblages, either inherited from the protolith (Rebay et al., 2010; Vitale Brovarone et al., 2011) or fluid migration during metamorphism (Gao and Klemd, 2001).

Firstly, comparing the major elements of blueschists and eclogites from the Raspas Metamorphic Complex, we observe that the eclogites have more FeO, MnO, Na_2O, TiO_2, and K_2O. In contrast, the blueschists have more MgO, CaO, and Al_2O_3. At first glance, with only this information, it could be concluded that the high contents of MnO, Na_2O, and TiO_2 favored the

formation of garnet, omphacite, and rutile. In contrast, the high MgO and CaO contents favored the formation of amphibole and epidote. However, this oversimplification disregards the complexity of the chemical relationship in metamorphic systems. They are reflected by the presence of minerals with solid solutions, such as amphiboles, in both rock types and the net reactions involved during the transitions between them.

Previous works proposed that instead of isolated elements, $Na_2O/(Na_2O+CaO)$, $CaO/(CaO+FeO)$, and A/CNK ratios are more reliable parameters that influence the formation of blueschists or eclogites (Gómez-Pugnaire et al., 1997; Vitale Brovarone et al., 2011; Tian and Wei, 2014). Furthermore, Tian and Wei (2014) noticed that when A/CNK when is compared with $Na_2O/(Na_2O+CaO)$ and $CaO/(CaO+FeO)$, the blueschists and eclogites they are grouped separately, where the blueschists are favored by higher A/CNK and $Na_2O/(Na_2O+CaO)$, whereas eclogites by higher $CaO/(CaO+FeO)$.

Unfortunately, these parameters are unsuited to explain why the Raspas blueschists and eclogites coexist. Firstly, because they differ from the other localities where these rocks reached the same P-T conditions, the eclogites and blueschists from Raspas possess different peak metamorphic conditions. Secondly, because their composition is very similar when plotted in the A/CNK vs. $Na_2O/(Na_2O+CaO)$ and $CaO/(CaO+FeO)$ overlap each other (Figure 12a, b).

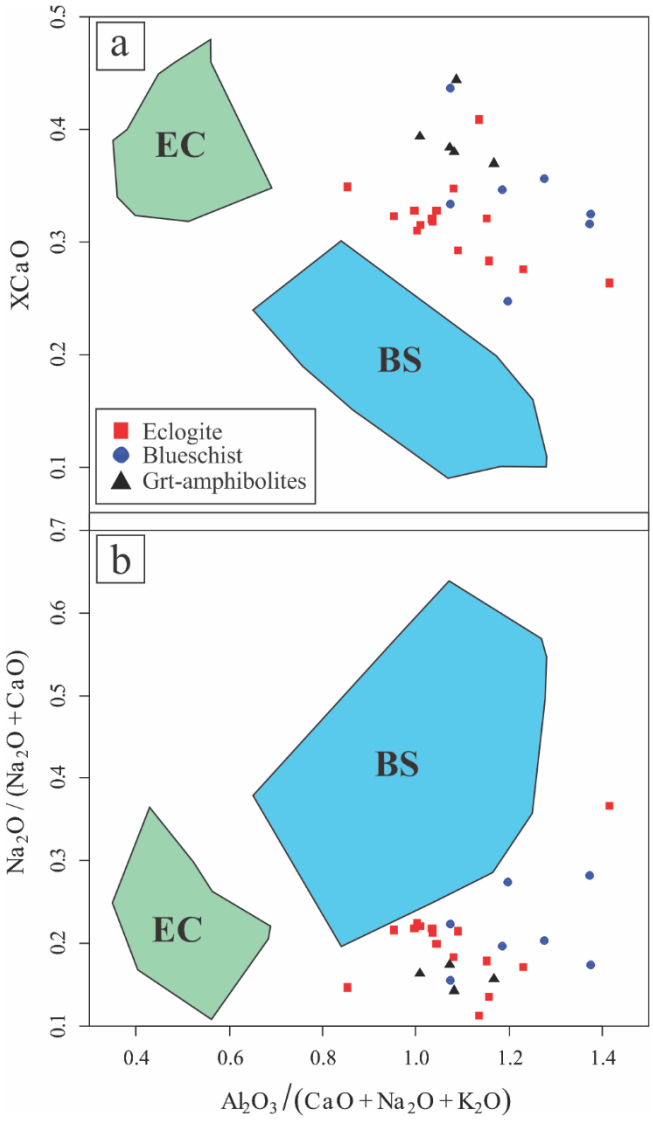

Figure 12 A/CNK vs. $Na_2O/(Na_2O+CaO)$ (a) and $CaO/(CaO+FeO)$ (b) diagrams after Tian and Wei (2014) showing the compositional factors influencing the formation of eclogites (EC field) and blueschists (BS field). For comparison, geochemical analysis of blueschists (blue circles), eclogites (red square) and garnet amphibolites (black triangle) of the Raspas Metamorphic Complex. Notice that all analysis is grouped together and outside the compositional fields for these rock types. Geochemical analysis of Raspas Metamorphic Complex is from Arculus et al. (1999), Bosh et al. (2002), John et al. (2010), and da Silva et al. (2022).

Comparing previous P-T estimates with our results, it becomes clear that the blueschist assemblages registered the prograde path and were overprinted by an eclogite facies metamorphism. Furthermore, along the P-T path, the eclogites exhibit temperatures consistently ~100 °C warmer than the conditions presented in this work for their blueschist equivalent.

A possible explanation lies in the resorption features present in the atoll garnets from eclogite samples described by Silva et al. (submitted). Their work observed channel-like structures visible in the compositional maps indicating fluid infiltration during the HP event. Therefore, the compositional changes during rock-fluid interaction could have altered the Lu-Hf ages (Kelly et al., 2011) reported by John et al. (2010). However, the currently available data is insufficient to support this hypothesis.

We prefer the possibility of thermal zoning inside the subducted oceanic plateau controlling the resulting HP assemblages. Thermal zoning is relatively common in subduction zones (Peacock et al., 2005). Moreover, due to the width of the plateau, the time needed for the thermal energy from the surrounding mantle heat of the downgoing slab would be more significant than for a 'normal' oceanic slab. The latter is reflected by the difference of > 100 °C between the peak conditions of eclogites and blueschists. They assume that the blueschists Lu/Hf ages represent the age of garnet formation. In contrast, the eclogites represent the formation of atoll garnets formed (see da Silva et al., 2022). It took 0.9-1.3 Ma (considering the error margin) for the heat to travel through the plateau until it reached the blueschists.

During the early stages of the blueschists evolution, the formation of the assemblage white mica (paragonite + phengite) + epidote/zoisite + winchite + quartz (490 °C/1.15 GPa) is followed by an isothermal compression during the formation of garnet cores (523 °C/1.68 GPa) resulting in a thermal gradient of ~311°C/GPa (Fig. 13). The overpressure of ~0.5 GPa during the formation of garnet, although may not seem significant, but is comparable to collisional belts (e.g., Massonne and Li, 2022; Fig. 13) thus, indicating that the blueschists record when the Raspas Plateau collided with the Andean margin. Moreover, the 0.9-1.3 Ma period to the temperature increase at deeper portions of the plateau constrains the minimum duration of the collisional event.

Furthermore, the isobaric heating experienced by the eclogites that accounted for an increase of ca. 50 °C (da Silva et al., submitted) is very similar to the temperature difference between the appearance of garnet and the metamorphic peak on the blueschists (ca. 80 °C; Fig. 13). Da Silva et al. (2022) interpreted this as the effect of a thinning of the plateau before a slab breakoff, which accounted for the small decompression observed in the blueschists during the formation of garnet rims (572 °C/ 1.53 GPa) and before the growth of omphacite + phengite porphyroblasts at the metamorphic peak (Fig. 13).

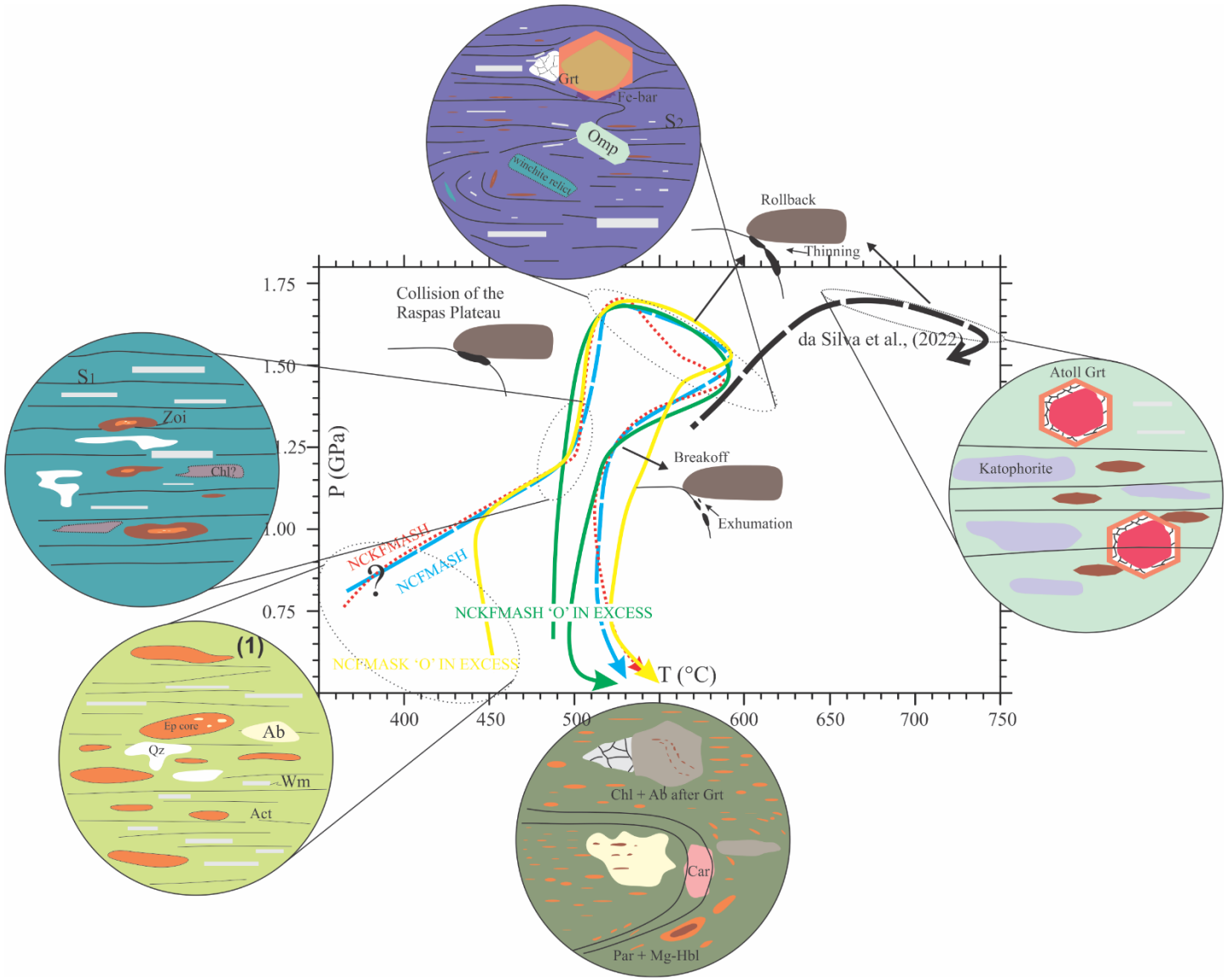

Figure 13 Resume of the metamorphic, textural, and tectonic evolution from Raspas Metamorphic Complex, see text for further discussion. P-T path from eclogites from da Silva et al., (2022) is plotted as black dashed line for comparison. Act – actinolite, Par – pargasite, Mg-Hbl – Mg-hornblende, Zoi – zoisite, Chl – chlorite, Qz – quartz, Fe-bar – Fe-barroisite, Ab – albite, Ep – epidote, Wm – white mica.

The exhumation had the onset marked by the formation of Fe-barroisite coupled with the decrease of pressure and temperature (550 °C/1.25 GPa; Fig. 13). Following; an isothermal decompression took place during the breakdown of the main HP minerals to the formation of greenschist to amphibolite facies assemblage (450-550 °C/>0.6 GPa). This PT path during the exhumation is consistent with the hypothesis of a slab breakoff presented by da Silva et al. (2022) to explain the fast exhumation rates indicated by the 129-123 Ma Ar-Ar ages (Fig. 13; Gabriele, 2002; da Silva et al., 2022).

CONCLUSION

This contribution presented mineral analysis and thermodynamic constraints to unravel the early stages of the metamorphic evolution during the subduction of an oceanic plateau. The blueschists exhibit a metamorphic P-T path consistently ~100 °C cooler than their eclogitic equivalent throughout their evolution. The early stages registered by the blueschists reveal the formation of the assemblage winchite + paragonite/phengite + epidote/zoisite + quartz ± chlorite at 490 °C and 1.15 GPa. An isothermal compression followed this event during the collision of the Raspas Plateau with the Andean margin resulting in the assemblage winchite + $garnet_{(core)}$ + phengite + zoisite + quartz ± chlorite at 523 °C and 1.68 GPa. The apparent diachronic HP event registered by the eclogites (~133 Ma) and blueschists (~126 Ma) was due to the thickness of the plateau that hindered the heat flow through the slab. The time difference of 0.9-1.3 Ma between the HP events enables us to estimate the minimum constraints of the duration of the collisional event. Before the onset of exhumation, the plateau experienced a thinning during a rollback which was responsible for a small decompression during the formation of garnet rims and prior to the metamorphic peak. The thinning enables the increase of temperature resulting in the formation of omphacite and phengite porphyroblasts around 570-590 °C and 1.4-1.7 GPa. The exhumation had the onset marked by the appearance of Fe-barroisite in contact with the garnet rims at 550 °C and 1.25 GPa before the slab breakoff. During break-off, the blueschists experienced an isothermal decompression to the formation of the assemblage pargasite/Mg-hornblende + albite + chlorite + quartz at 450-550 °C and < 0.6 GPa.

ACKNOWLEDGMENTS

This study was supported by the brazilian agencies National Council for Scientific and Technological (CNPq) grant 458735/2014-0 and Fundação de Amparo à Pesquisa do Estado de

São Paulo (FAPESP) grant 2004/10203-7. S. P. da Silva thanks the Coordenação de Aperfeiçoamento de Pessoal de Nível Superior – Brasil (CAPES) - Finance Code 001 by the partial financial support.

REFERENCES

Agard, P., Yamato, P., Jolivet, L., Burov, E., 2009. Exhumation of oceanic blueschists and eclogites in subduction zones: Timing and mechanisms. Earth-Science Reviews 92(1-2), 53-79 https://doi.org/10.1016/j.earscirev.2008.11.002.

Arculus, R.J., Lapierre, H., Jaillard, E., 1999. Geochemical window into subduction and accretion processes: Raspas metamorphic complex, Ecuador. Geology 27, 547-550.

Aspden, J. A., Bonilla, W., Duque, P., 1995. The El Oro metamorphic complex, Ecuador: geology and economic mineral deposits. Nottingham, British Geological Survey, Overseas Geology and Mineral Resources 67, p. 63.

Avellaneda-Jimenez, D. S., Cardona, A., Valencia, V., León, S., Blanco-Quintero, i. F., 2021. Metamorphic gradient modification in the Early Cretaceous Northern Andes subduction zone: A record from thermally overprinted high-pressure rocks. Geoscience Frontiers https://doi.org/10.1016/j.gsf.2020.09.019

Bosch, D., Gabriele, P., Lapierre, H., Malfere, J., Jaillard, E., 2002. Geodynamic significance of the Raspas Metamorphic Complex (SW Ecuador): geochemical and isotopic constraints. Tectonophysics 345, 83-102.

Brun, J. -P., Faccenna, C., 2008. Exhumation of high-pressure rocks driven by slab rollback. Earth and Planetary Science Letters 272, 1-7 https://doi.org/10.1016/j.epsl.2008.02.038.

Bustamante, A., 2008. Geotermobarometria, geoquímica, geocronologia e evolução tectônica das rochas da fácies xisto azul nas áreas de Jambaló (Cauca) e Barragán (Valle del Cauca), Colômbia. Thesis -Instituto de Geosciências, Universidade de São Paulo, São Paulo, 179p.

Bustamante, A., Bustamante, A., Cardona, A., Juliani, C., da Silva, S., 2021. Jambaló blueschist and greenschist protoliths in the Central Cordillera of the Colombian Andes and their tectonic implications for Late Cretaceous Caribbean-South American interactions. Journal of South American Earth Sciences 107, 102977.

Bustamante, A., Juliani, C., Essene, E. J., Hall, C. M., Hyppolito, T., 2012. Geochemical constraints on blueschist- and amphibolite-facies rocks of the Central Cordillera of Colombia: the Andean Barragán region. International Geological Review 54, 1013-1030.

Bustamante, C., Archanjo, C. J., Cardona, A., Vervoort, J. D., 2016. Late Jurassic to Early Cretaceous plutonism in the Colombian Andes: A record of long-term arc maturity. Geological Society of America Bulletin 128, 1762-1779.

Bustamante, C., Bustamante, A., 2019. Two Cretaceous subduction events in the Central Cordillera: Insights from the high P–low T metamorphism. In: Gómez, J. & Pinilla–Pachon, A.O. (editors), The Geology of Colombia, Volume 2 Mesozoic. Servicio Geológico Colombiano, Publicaciones Geológicas Especiales 36, p. 485–498. Bogotá. https://doi.org/10.32685/pub.esp.36.2019.14

da Silva, S. P., Bustamante, A., Bustamante, C., Cardona, A., Juliani, C., 2022. Early Cretaceous subduction of an oceanic plateau at the Northern Andes; geochemical, metamorphic, and cooling age constraints of the Raspas Metamorphic Complex. Submitted to Lithos on September 2022.

de Capitani, C., Brown, T. H., 1987. The computation of chemical equilibrium in complex systems containing non-ideal solutions. Geochimica et Cosmochimica Acta 51, 2639-2652.

de Capitani, C., Petrakakis, K., 2010. The computation of equilibrium assemblage diagrams with Theriak/Domino software. American Mineralogist 95, 1006-1016.

Diener, J. F. A., Powell, R., 2011. Revised activity–composition models for clinopyroxene and amphibole. Journal of Metamorphic Geology 30(2), 131-142. https://doi.org/10.1111/j.1525-1314.2011.00959.x

Gabriele, P., 2002. HP terranes exhumation in an active margin setting: geology and geochemistry of the Raspas Complex in SW Ecuador. Unpublished Ph.D. thesis, University of Laussane, Switzerland.

Gao, J., Klemd, R., 2001. Primary fluids entrapped at blueschist to eclogite transition: evidence from the Tianshan meta-subduction complex in northwestern China. Contributions to Mineralogy and Petrology 142, 1-14.

García-Ramírez, C.A., Ríos-Reyes, C.A., Castellanos-Alarcón, O.M., Mantilla-Figueroa, L.C., 2017. Petrology, geochemistry and geochronology of the Arquía Complex's metabasites at the Pijao-Génova sector, Central Cordillera, Colombian Andes. Boletín de Geología 39 (1), 105–126.

Gosso, G., Messiga, B., Rebay, G., Spalla, M., 2010. Interplay between deformation and metamorphism during eclogitization of amphibolites in the Sezia-Lanzo Zone of the Western Alps. International Geology Review 52, 1193-1219.

Green, E. C. R., Holland, T., Powell, R., 2007. An order-disorder model for omphacitic pyroxenes in the system jadeite-diopsidehedenbergite- acmite, with applications to eclogitic rocks. American Mineralogist 92(7), 1181-1189.

Hawthorne, F. C., Oberti, R., Harlow, G. E., Maresch, W. V., Martin, R. F., Schumacher, J. C., Welch, M. D., 2012. Nomenclature of the amphibole supergroup. American Mineralogist 97, 2031-2048. http://dx.doi.org/10.2138/am.2012.4276

Holland T., Judy, B., Powell, R., 1998. Mixing properties and activity-composition relationships of chlorites in the system MgO-FeO-Al2O3-SiO2-H2O. European Journal of Mineralogy 10(3), 395-406.

Holland, T. J. B., Powell, R., 1998. An internally consistent thermodynamic data set for phases of petrological interest. Journal of Metamorphic Geology 16, 309-343.

Holland T., Powell, R., 2003. Activity–composition relations for phases in petrological calculations: an asymmetric multicomponent formulation. Contributions to Mineralogy and Petrology 145, 492-501. https://doi.org/10.1007/s00410-003-0464-z

John, T., Scherer, E. E., Schenk, V., Herms, P., Halama, R., Garbe-Schonberg, D., 2010. Subducted seamounts in an eclogite-facies ophiolite sequence: the Andean Raspas Complex, SW Ecuador. Contributions to Mineralogy and Petrology 159, 265-284. DOI 10.1007/s00410-009-0427-0

Kelly, E. D., Carlson, W. D., Connelly, J. N., 2011. Implications of garnet resorption for the Lu-Hf garnet geochronometer: an example from the contact aureole of the Makhavinekh Lake Pluton, Labrador. Journal of Metamorphic Geology 29(8), 901-916.

Kerr, A. C., Marriner, G. F., Tarney, J., Nivia, A., Saunders, A. D., Thirlwall, M. F., Sinton, C. W., 1997. Cretaceous Basaltic Terranes in Western Colombia: Elemental, Chronological and Sr–Nd Isotopic Constraints on Petrogenesis. Journal of Petrology 38 (6), 677-702.

Kerrick, D. M., Connolly, J. A. D., 2001. Metamorphic devolatilization of subducted oceanic metabasalts: implications for seismicity, arc magmatism and volatile recycling. Earth and Planetary Science Letters 189(1-2), 19-29. https://doi.org/10.1016/S0012-821X(01)00347-8

Kydonakis, K., Moulas, E., Chatzitheodoridis, E., Brun, J. -P., Kostopoulos, D., 2015. First-report on Mesozoic eclogite-facies metamorphism preceding Barrovian overprint from the western Rhodope (Chalkidiki, northern Greece). Lithos 220-223, 147-163 https://doi.org/10.1016/j.lithos.2015.02.007.

Lanari, P., 2020. An introduction to XMapTools. User guide, version 2020-6-10.

Lanari, P., Vidal, O., De Andrade, V., Dubacq, B., Lewin, E., Grosch, E., & Schwartz, S., 2014. XMapTools: a MATLAB©-based program for electron microprobe X-ray image processing and geothermobarometry. Computers and Geosciences, 62, 227-240.

Lanari, P., Giuntoli, F., Loury, C., Burn, M., Engi, M., 2017. An inverse modeling approach to obtain P–T conditions of metamorphic stages involving garnet growth and resorption. European Journal of Mineralogy 29, 181-199. DOI: 10.1127/ejm/2017/0029-2597

Liu, Z., Dai, L., Li, S., Wang, L., Xing, H., Liu, Y., Ma, F., Dong, H., Li, F., 2021. When plateau meets subduction zone: A review of numerical models. Earth-Science Reviews 215, 103556. https://doi.org/10.1016/j.earscirev.2021.103556

Mamberti, M., Lapierre, H., Bosch, D., Jaillard, E., Ethien, R., Hernandez, J., Polvé, M., 2003. Accreted fragments of the Late Cretaceous Caribbean-Colombian Plateau in Ecuador. Lithos 66, 173-199.

Maruyama, S., Liou, J. G., Terabayashi, M., 1996. Blueschists and Eclogites of the World and Their Exhumation. International Geology Review 38(6), 485-594. https://doi.org/10.1080/00206819709465347

Massonne, H. -J., Li, B., 2022. Eclogite with unusual atoll garnet from the southern Armorican Massif, France: Pressure-temperature path and geodynamic implications. Tectonophysics 823, 229183. https://doi.org/10.1016/j.tecto.2021.229183

McCourt, W.J., Aspden, J.A., Brook, M., 1984.New geological and geochemical data from the Colombian Andes: continental growth by multiple accretion. Journal of the Geological Society 831–845.

Oh, C. H., Liou, J. G., Maruyama, S., 1991. Low-Temperature Eclogites and Eclogitic Schists in Mn-rich Metabasites in Ward Creek, California; Mn and Fe Effect s on the Transition between Blueschist and Eclogite. Journal of Petrology 32(2), 275-301.

Ota, T., Utsunomiya, A., Uchio, Y., Isozaki, Y., Buslov, M., M., Ishikawa, A., Maruyama, S., Kitajima, K., Kaneko, Y., Yamamoto, H., Katayama, I., 2007. Geology of the Gorny Altai subduction–accretion complex, southern Siberia: Tectonic evolution of an Ediacaran–Cambrian intra-oceanic arc-trench system. Journal of Asian Earth Sciences 30, 666-695. https://doi.org/10.1016/j.jseaes.2007.03.001

Ota, T., Kaneko, Y., 2010. Blueschists, eclogites, and subduction zone tectonics: Insights from a review of Late Miocene blueschists and eclogites, and related young high-pressure metamorphic rocks. Gondwana Research 18, 167-188. https://doi.org/10.1016/j.gr.2010.02.013

Peacock, S. M., 1993. The importance of blueschist-eclogite dehydration reactions in subducting oceanic crust. Geological Society of America Bulletin 105, 684-694.

Peacock, S. M., van Keken, P. E., Holloway, S. D., Hacker, B. R., Abers, G. A., Fergason, R. L. 2005. Thermal structure of the Costa Rica – Nicaragua subduction zone. Physics of the Earth and Planetary Interiors 149 (1-2), 187-200.

Rebay, G., Powell, R., Diener, F. A., 2010. Calculated phase equilibria for a MORB composition in a P-T range, 450-650 °C and 18-28 kbar: the stability of eclogite. Journal of Metamorphic Geology 28, 635-645.

Ridley, J., 1984. Evidence of a Temperature-dependent 'Blueschist' to 'Eclogite' Transformation in High-pressure Metamorphism of Metabasic Rocks. Journal of Petrology 25(4), 852-870.

Spikings, R. A., Cochrane, R. S., Villagomez, D., Van der Lelij, D., Vallejo, C., Winkler, W., Beate, B., 2015. The geological history of northwestern South America: from pangaea to the early collision of the Caribbean large igneous province (290-75 Ma). Gondwana Research 27, 95–139.

Tian, Z. L., Wei, C. J., 2014. Coexistence of garnet blueschist and eclogite in South Tianshan, NW China: dependence of P–T evolution and bulk-rock composition. Journal of Metamorphic Geology 32, 743-764.

Toussaint, J.F., Restrepo, J.J., 1994.The Colombian Andes during Cretaceous times. In: Salfity, J.A. (Ed.), Cretaceous Tectonics of the Andes. Earth Evolution Series. Vieweg and Teubner Verlag, pp. 61–100.

Vallejo, C., Winkler, W., Sipikings, R. A., Luzieux, L., Heller, F., Bussy, F., 2009. Mode and timing of terrane accretion in the forearc of the Andes in Ecuador. The Geological Society of America Memoir 204, p.

Villagómez, D., Spikings, R., Magna, T., Kammer, A., Winkler, W., Beltrán, A., 2011. Geochronology, geochemistry and tectonic evolution of the Western and Central cordilleras of Colombia. Lithos 125, 875-896.

Vitale Brovarone, A., Groppo, C., Hetényi, G., Compagnoni, R., Malavieille, J., 2014. Coexistence of lawsonite-bearing eclogite and blueschist: phase equilibria modelling of Alpine Corsica metabasalts and petrological evolution of subducting slabs. Journal of Metamorphic Geology 29, 583-600.

Whitney, D. L., Davis, P. B., 2006. Why is lawsonite eclogite so rare? Metamorphism and preservation of lawsonite eclogite, Sivrihisar, Turkey. Geology 34(6), 473-476 https://doi.org/10.1130/G22259.1.

Zapata-Villada, J. P., Restrepo, J. J., Cardona, A, Martens, U., 2017. Geoquímica y geocronología de las rocas volcánicas básicas y el Gabro de Altamira, Cordillera Occidental (Colombia): Registro de ambientes de Plateau y arco oceánico superpuestos durante el cretácico. Boletín de Geología, 39(2), 13-30.

Zhang, X, -Z., Wang, Q., Dong, Y. -S., Zhang, C., Li, Q. -Y., Xia, X. -P., 2017. High-Pressure Granulite Facies Overprinting During the Exhumation of Eclogites in the Bangong-Nujiang Suture Zone, Central Tibet: Link to Flat-Slab Subduction. Tectonics 36(12), 2918-2935. https://doi.org/10.1002/2017TC004774

6 CONCLUSÕES

Dados inéditos de química mineral, geoquímica e idades Ar/Ar em fengita demonstram a possibilidade de subducção e exumação de platôs oceânicos. Modelagem termodinâmica de xisto azul e eclogito do Complexo Metamórfico Raspas desvendaram o reflexo metamórfico da subducção de um platô oceânico.

Os metabasaltos exibem em diagramas normalizados padrão plano dos elementos terras raras pesados enquanto os leves exibem padrão variado similares a N- e E-MORB. Razões entre elementos traço demonstram uma origem a partir de uma fonte heterogênea (Zr/Nb – 7.69-112.66) com variável grau de fusão parcial (La/Yb 0.76-6.86) e profundidade (Sm/Yb 0.94-1.95). Adicionalmente as rochas seguem o trend de rochas tipo ‘Icelandito” no diagrama Zr/Y vs. Nb/Y.

Durante toda o metamorfismo de alta pressão há consistentemente uma diferença de ~100°C entre xisto azul e eclogito. Devido a elevada espessura o fluxo térmico no platô não foi coerente resultando em um zoneamento térmico em seu interior. Os estágios iniciais são marcados pela sua colisão com a margem Andina caracterizados por uma geometria plana com baixo ângulo de subducção que imprimiu uma compressão isotermal entre 490 °C/1.15 GPa e 523 °C/1.68 GPa exibida pelo xisto azul, enquanto no eclogito é 598-661 °C/1.43-1.63 GPa. Após parte do platô ser transformado em eclogito o aumento resultante de densidade favoreceu o aumento do ângulo de subducção. Essa fase é marcada pelo fluxo astenosférico e diminuição da espessura do platô antes do breackoff. Esse estágio é responsável pelo pico metamórfico exibido por ambos, xisto azul (570-590 °C/1.4-1.7 GPa) e eclogito (709 °C/1.61 GPa), contudo no eclogito destaca-se pelo aquecimento isobárico. A exumação teve início durante o breackoff em 129 Ma evidenciado pela rápida ascensão (1.25-0.5 cm/ano) e pela descompressão isotermal exibida pelo xisto azul (450-550 °C /< 0.6 GPa).

REFERÊNCIAS

ARCULUS, R. J.; LAPIERRE, H.; JAILLARD, R. **Geochemical window into subduction and accretion processes:** Raspas metamorphic complex, Ecuador. Geology, 27, 547-550, 1999.

BLANCO-QUINTERO, I. F.; GARCÍA-CASCO, A.; TORO, L. M.; MORENO, M.; RUIZ, E. C.; VINASCO, C. J.; CARDONA, A.; LÁZARO, C.; MORATA, D. **Late Jurassic terrane collision in the northwestern margin of Gondwana (Cajamarca Complex, eastern flank of the Central Cordillera, Colombia).** International Geology Review 56, 1852-1872, 2014.

BOSH, D.; GABRIELE, P.; LAPIERRE, H.; MALFERE, J.; JAILLARD, E. **Geodynamic significance of the Raspas Metamorphic Complex (SW Ecuador):** geochemical and isotopic constraints. Tectonophysics 345, 83-102, 2002.

BUSTAMANTE, C.; ARCHANJO, C. J.; CARDONA, A.; VERVOORT, J. D. **Late Jurassic to Early Cretaceous plutonism in the Colombian Andes:** A record of long-term arc maturity. Geological Society of America Bulletin 128, 1762-1779, 2016.

CAMPBELL, I. H. **Testing the plume theory.** Chemical Geology 241 (3-4), 153-176, 2007.

CARDONA, A.; LEÓN, S.; JARAMILLO, J. S.; VALENCIA, V.; ZAPATA, S.; PARDO-TRUJILLO, A.; SCHMITT, A. K., MEJÍA, D.; ARENAS, J. C. **Cretaceous Record from a Mariana– to an Andean–Type Margin in the Central Cordillera of the Colombian Andes.** In: The Central Cordillera of the Colombian Andes. In: Gómez, J. & Pinilla-Pachon, A.O. (editors), The Geology of Colombia, Volume 2 Mesozoic. Servicio Geológico Colombiano, Publicaciones Geológicas Especiales 36, 39 p. Bogotá. https://doi.org/10.32685/pub.esp.36.2019.10.

CARLSON, W. D.; PATTISON, D. R. M.; CADDICK, M. J. **Beyond the equilibrium paradigm:** How consideration of kinetics enhances metamorphic interpretation. American Mineralogist 100, 1659-1667, 2015.

DE CAPITANI, C.; BROWN, T. H. **The computation of chemical equilibrium in complex systems containing non-ideal solutions.** Geochimica et Cosmochimica Acta 51, 2639-2652, 1987.

DE CAPITANI, C.; PETRAKAKIS, K. **The computation of equilibrium assemblage diagrams with Theriak/Domino software.** American Mineralogist 95 (7), 1006–1016, 2010.

DUESTERHOELFT, E.; LANARI, P. **Iterative thermodynamic modelling—Part 1:** A theoretical scoring technique and a computer program (Bingo-Antidote). Journal of Metamorphic Geology 38, 1-25, 2020.

ESKOLA, P. **On the relations between the chemical and mineralogical composition in the metamorphic rooks of the Orijärvi region.** Comm. Geol. Finlande Bull.44, 1–107 [in Finnish], 109–145 [in English] (1915).

FITTON, J. G., SAUNDERS, A. D., NORRY, M. J., HARDARSON, B. S., TAYLOR, R. N. **Thermal and chemical structure of the Iceland plume.** Earth and Planetary Science Letters 153, 197-208, 1997.

GABRIELE, P. **HP terranes exhumation in an active margin setting:** geology and geochemistry of the Raspas Complex in SW Ecuador. Unpublished Ph.D. thesis, University of Laussane, Switzerland, 2002.

GERYA, T. V.; STOCKHERT, B. **Exhumation rates of high pressure metamorphic rocks in subduction channels:** The effect of Rheology. Geophysical Research Letters 29 (8), 102-1-102-4, 2002.

GIRAULT, J. B.; BELLAHSEN, N.; BERNET, M.; LOGET, N.; LASSEUR, E.; ROSENBERG, C. L.; BALVAY, M.; SONNET, M. **Exhumation of the Western Alpine collisional wedge: New thermochronological data**. Tectonophysics 822, 22915, January 2022.

JOHN, T.; SCHERER, E. E.; SCHENK, V.; HERMS, P.; HALAMA, R.; GARBE-SCHONBERG, D. **Subducted seamounts in an eclogite-facies ophiolite sequence:** the Andean Raspas Complex, SW Ecuador. Contributions to Mineralogy and Petrology 159, 265-284, 2010.

KERR, A. C. **4.18 – Oceanic Plateaus, In:** Treatise on Geochemistry (second edition) (Holland, H. D and Turekian, K. K, eds). Oxford, Elsevier 4, 631-667, 2014.

KERR, A. C., WHITE, R. V., SAUNDERS, A. D. **LIP reading:** Recognizing oceanic plateaux in the geological record. Journal of Petrology 41 (7), 1041-1056, 2000.

KERR, A. C.; TARNEY, J.; KEMPTOM, P. D.; SPADEA, P.; NIVIA, A.; MARRINER, G. F.; DUNCAN, R. A. **Pervasive mantle plume head heterogeneity:** Evidence from the late Cretaceous Caribbean-Colombian oceanic plateau. Journal of Geophysical Research 107, ECV 2-1-ECV 2-13, 2002.

KLEMD, R.; GAO, J.; LI, J-. L.; MEYER, M. **Metamorphic evolution of (ultra)-high-pressure subduction-related transient crust in the South Tianshan Orogen (Central Asian Orogenic Belt):** Geodynamic implications. Gondwana Research 28 (1), 1-25, 2015.

LANARI, P.; ENGI, M. **Local bulk composition effects on metamorphic mineral assemblages.** Reviews in Mineralogy and Geochemistry 83 (1), 55-102, 2017.

LANARI, P.; GIUNTOLI, F.; LOURY, C.; BURN, M.; ENGI, M. **An inverse modeling approach to obtain P-T conditions of metamorphic stages involving garnet growth and resorption.** European Journal of Mineralogy 29, 181-199, 2017.

LIU, Z.; DAI, L.; LI, S.; WANG, L.; XING, H.; LIU, Y.; MA, F.; DONG, H.; LI, F. **When plateau meets subduction zone:** A review of numerical models. Earth-Science Reviews 215, 103556, 2021.

MAHONEY, J. J., SINTON, J. M., MACDOUGALL, J. D., SPENCER, K. J., LUGMAIR, G. W. **Isotope and trace element characteristics of a super-fast spreading ridge:** East-Pacific rise, 13-23°S. Earth and Planetary Science Letters 121, 173-193, 1994.

MALONEY, K. T.; CLARKE, G. L.; KLEPEIS, K. A.; QUEVEDO, L. **The Late Jurassic to present evolution of the Andean margin:** Drivers and the geological record. Tectonics 32 (5), 1049-1065, 2013.

MARRINER, G. F., MILLWARD, D. **The petrology and geochemistry of Cretaceous to Recent volcanism in Colombia:** The magmatic history of an accretionary plate margin. Journal of the Geological Society, London 141, 473-486, 1984.

OTA, T.; BUSLOW, M. M.; WATANABE, T. **Metamorphic evolution of Late Precambrian eclogites and associated metabasites, Gorby Altai, Southern Russia.** International Geological Review 44, 837-858, 2002.

OTA, T.; UTSUNOMIYA, A.; UCHIO, Y.; ISOZAKI, Y.; BUSLOV, M. M.; ISHIKAWA, A.; MARUYAMA, S.; KITAJIMA, K.; KANEKO, Y.; YAMAMOTO, H.; KATAYAMA, I. **Geology of the Gorny Altai subduction-accretion complex, southern Siberia:** Tectonic evolution of an Ediacaran-Cambrian intra-oceanic arc-trench system. Journal of Asian Earth Sciences 30, 666-695, 2006.

RESTREPO, M.; BUSTAMANTE, C.; CARDONA, A.; BELTRÁN-TRIVIÑO, A.; BUSTAMANTE, A.; CHAVARRÍA, L.; VALENCIA, V. A. **Tectonic implications of the Jurassic magmatism and the metamorphic record at the southern Colombian Andes.** Journal of South American Earth Sciences 111, 103439, 2021, https://doi.org/10.1016/j.jsames.2021.103439.

RUBIE, D. C. **Disequilibrium during metamorphism:** the role of nucleation kinetics. Geological Society, London, Special Publications 138, 199-214, 1998.

SPEAR, F.; WOLFE, O. M. **Evaluation of the effective bulk composition (EBC) during growth of garnet.** Chemical Geology 491, 39-47, 2018.

SPIKINGS, R. A.; COCHRANE, R. S.; VILLAGOMEZ, D.; VAN DER LELIJ, D.; VALLEJO, C.; WINKLER, W.; BEATE, B. **The geological history of northwestern South America:** from pangaea to the early collision of the Caribbean large igneous province (290-75 Ma). Gondwana Research 27, 95–139, 2015.

STERN, R. J. **Subduction zones.** Reviews of Geophysics 40 (4), 3-1 – 3-38, 2002.

SUN, S. S., MCDONOUGH, W. F. **Chemical and isotopic systematics of oceanic basalts:** Implications for mantle composition and processes. In: Saunders, A. D., Norry, M.J. (eds.) Magmatism in the Ocean Basins, Geological Society Special Publication 42, pp. 313–345. London: Geological Society of London, 1989.

SUN, B. B., KLAUS, B. J. P., YANG, J., LU, G., WANG, X., WANG, K., ZHAO, L. **Subduction polarity reversal triggered by oceanic plateau accretion:** Implications for induced subduction initiation. Geophysical Research Letters 48 (24), e2021GL095299, 2021.

THRILWALL, M. F., GRAHAM, A. M., ARCULUS, R. J., HARMON, R. S., MACPHERSON, C. G. **Resolution of the effects of crustal assimilation, sediment subduction and fluid transport in island arc magmas:** Pb-Sr-Nd-O isotope geochemistry of Grenada, Lesser Antilles. Geochimica et Cosmochimica Acta 60, 4785-4810, 1996.

VALLEJO, C.; SPIKINGS, R. A.; LUZIEUX, L.; WINKLER, W.; CHEW, D.; PAGE, L. **The early interaction between the Caribbean Plateau and the NW South American Plate.** Terra Nova 18, 264-269, 2006.

VILLAGÓMEZ, D.; SPIKINGS, R.; MAGNA, T.; KAMMER, A.; WINKLER, W.; BELTRÁN, A. **Geochronology, geochemistry and tectonic evolution of the Western and Central cordilleras of Colombia.** Lithos 125, 875-896, 2011.

WALTER, J. V.; WOOD, B. J. **Rate and mechanism in prograde metamorphism.** Contributions to Mineralogy and Petrology 88, 246-259, 1984.

ZHENG, Y, -F. **Subduction zone geochemistry.** Geoscience Frontiers 10, 1223-1254, 2019.